2017

# Resonant Interactions in Strong Field Laser Physics

Seth Jacob Camp
*Louisiana State University and Agricultural and Mechanical College*

# RESONANT INTERACTIONS IN STRONG FIELD LASER PHYSICS

A Dissertation

Submitted to the Graduate Faculty of the
Louisiana State University and
Agricultural and Mechanical College
in partial fulfillment of the
requirements for the degree of
Doctor of Philosophy

in

The Department of Physics and Astronomy

by
Seth Camp
BS, Berry College, 2011
August 2017

# Acknowledgements

Let me begin by thanking my friends, family, collaborators, and committee members. This thesis is only possible because of significant help, support, and guidance from all of you. I would like to also thank all of my professors and classmates that I encountered along the way to writing this thesis. I would also like to thank several specific people, who greatly contributed to my success along the way.

To my advisors, Dr. Mette Gaarde and Dr. Kenneth Schafer, I would like to thank you for your guidance, patience, and caring in my research and studies. This thesis would absolutely not exist without your efforts, advice, teaching, and help. I admit that six years ago, I had no idea what I was getting myself into by joining your research group. All I knew was that I liked quantum mechanics, I enjoyed programming, and that your research group would allow me to use both of these skills. Now, looking back, I see that as the biggest strike of luck that one could imagine. I had absolutely no idea that I was gaining such passionate, enthusiastic, and helpful mentors. You guided me through my graduate studies teaching me many things that I needed to know, and allowing me to discover the things that can't be taught. For this, I will be forever grateful.

To my group mates, Mengxi Wu, Paul Abanador, Francois Mauger, and Renate Pazourek, I would like to thank you for fruitful discussions, guidance, encouragement, and help along the way. I would also like to thoroughly thank all of you for allowing me to ask questions when I didn't understand a concept, and for patiently explaining the answer to me, even when I periodically interrupted with attempts at understanding and bad analogies. Without these discussions, I suspect that my understanding of high harmonic generation, classical mechanics, strong field phenomena, and transient absorption would be greatly diminished.

To Dr. Todd Timberlake, I would like to thank you for giving me my first introduction to quantum mechanics at Berry College, so many years ago. The homework was tough and the problems were many, but it was sufficient for giving a brilliant physical intuition to the strangeness of the quantum world, which I have applied nearly every day in my research in this field. I would also like to thank you for giving me my first introduction to computational and theoretical research in quantum mechanics. You introduced the problem, gave background on it, and got me started. Then you disappeared to a vacation for the summer, leaving me to my own devices. In many way, this helped prepare me for the independent motivation and imagination required of true scientific research. Further, the paper that we published from that work helped me earn a fellowship that funded the bulk of my graduate education. Needless to say, in your role as a mentor and a friend, I cannot thank you enough.

To Dr. Charles Lane, I would like to thank you for teaching me to think for myself and directly developing so many of my problem solving skills. On the first day of class, within a few minutes you would send us away with homework, a book, and nothing else. By the next class, we would be expected to start presenting solutions

to the homework on the board, all while you asked extremely pointed questions to test if we really understood what we were writing. Occasionally, you would even ask misleading questions to test our confidence and to help build physical intuition. It is in this fire that many of my problem solving skills were forged. The application of the problem solving skills that I acquired in your courses are what made much of the work in this thesis possible. I would also like to thank you for teaching me that sometimes the best solution for solving a tricky problem is to step away from it and relax a little. Over the last six years, this approach has been applied countless times, resulting in countless new ideas.

To Dr. Ron Taylor, I could spell out exactly all the ways that you have impacted my life and my education, however, there would not be enough room in a simple acknowledgment section of a thesis. To list a few: you convinced me to add a second major in Mathematics. You taught me logic in Proof Structures. You gave me advice and always believed in the best part of me. You were a listening ear when I needed to talk, and your couch and office still bring back many memories of comfort and happiness. You let me write essay's on the craziest of topics and thoroughly enjoyed them as much as I did. You helped me be the best Pape I could be. You were the best mentor, when I needed a mentor. You were the best teacher, when I needed a teacher. You were the best friend, when I needed a friend. You put more effort into these things than I (or any of your students) could ever pay back. As a result, you impacted my entire undergraduate education, graduate education, and influenced all of my research. For all of these reasons, Ron, and for an uncountably infinite number of others, I would like to thank you.

Finally, to my father, Ray Camp, I would like to thank you for your support, belief, and effort throughout these 28 years. You have always been there for me, knowing when to let me handle my own problems and when to give advice. In many ways, you put in just as much time into my education as I did, working too many hours to fund it, driving me places, nagging me to fill our paperwork, researching how to go about applying to undergraduate programs and graduate programs, researching what a physicist does. You always believed that I was good enough to do anything that I wanted, even if it seemed like a distant dream. When I came to you in the 9th grade and told you that I wanted to be a physicist, you were entirely on board and you have now helped me reach my dream. This thesis would not be possible without you. There's no way that I can ever pay back the effort that you put in, trying to help me be a better person and accomplish more in life than I should have ever reasonably been expected to accomplish. However, I dedicate this thesis to you, in order to begin trying.

# Preface

The work that I present in this thesis was performed in the Department of Physics and Astronomy at Louisiana State University, under the supervision of Dr. Mette Gaarde and Dr. Kenneth Schafer. The work can be divided into two separate, but related topics: the resonant interaction of light with gas-phase atoms in high harmonic generation (HHG) at the single atom level, and the resonant interaction of light with a macroscopic number of gas-phase atoms in transient absorption. As such, I have divided this thesis into two parts.

In Part I, we study the resonant interaction of light with gas-phase atoms in HHG. HHG is a physical phenomenon that occurs when an intense infrared (IR) laser beam passes through a gas of atoms, and leads to the generation of ultrafast, coherent extreme ultraviolet (XUV) light. On the single atom level, one can understand HHG in a simple three-step, semi-classical model. In this model, an atomic electron first tunnel ionizes out of the atomic core due to the strong field, is then accelerated away from the atomic core as a free particle in the laser field, and is then driven back to the core to recombine with the atom and give off a high-energy-photon from the excess energy picked up by ionizing and accelerating. This allows for the conversion of easy-to-make, low-energy photons into difficult-to-make, high-energy-photons. HHG is often used as an XUV light source in experiments studying atomic and molecular resonant interactions. Rapidly, however, interest is growing in using HHG, not just as a light source, but directly as a source of information about the resonant interactions that occur when the electron is ionized, accelerated, and recombined. This is what we explore in Part I of this thesis. In Chapter 1, we give a brief introduction to HHG and discuss how it can be used to study resonant interactions in atoms. In Chapter 2, we give an overview of the numerical techniques that we use throughout the thesis, in order to calculate the response of an atom to a laser pulse. In Chapter 3, we discuss enhancement of HHG through Stark-shifted resonances and the interplay of the resonant interaction with the typical quantum trajectories in HHG. In Chapter 4, we close by presenting a new approach for studying resonant enhancement that we have developed. Portions of the research in Chapter 4 were done in collaboration with Yann Mairesse's experimental group at the University of Bordeaux.

In Part II, we study the resonant interaction of light with a macroscopic medium in transient absorption. Transient absorption is an all-optical technique that makes use of an ultrafast XUV pulse and a moderately strong IR pulse to study electron dynamics. In this thesis, we examine the influence that a resonant macroscopic medium can play in transient absorption. We look at two influences: (i) We examine how a macroscopic medium can change the absorption line shape of a resonance. This absorption line shape is typically assumed to be independent of the medium, and controlled only by the gas species and the IR pulse. Demonstrating that this assumption can break down, and when, is an important part of this research. (ii) We also look at how a macroscopic medium can be used to steer resonant emission

in a different direction. In Chapter 5, we introduce transient absorption and the numerical techniques needed to extend single atom calculations to a macroscopic medium. Then in Chapter 6, we look at resonant pulse propagation changes to the absorption line shape in transient absorption. Finally, in Chapter 7, we examine a new technique that we have developed for controlling the direction of XUV light with a dressing IR pulse. The research presented in this portion of the thesis was done closely in collaboration Arvinder Sandu's experimental group at the University of Arizona (Chapter 6) and Johan Mauritsson's experimental group at Lund University (Chapter 7).

Many of the ideas and results presented in this thesis have appeared previously in the following publications:

- **S. Camp**, K. J. Schafer, and M. B. Gaarde. *Interplay between resonant enhancement and quantum path dynamics in harmonic generation in helium*, *Phys. Rev. A* **92**, 013404 (2015). Parts of Chapter 3 are based on this publication.

- S. Beaulieu, **S. Camp**, D. Descamps, A. Comby, V. Wanie, S. Petit, F. Legare, K. J. Schafer, M. B. Gaarde, F. Catoire, and Y. Mairesse. *Role of Excited States in High-order Harmonic Generation*, *Phys. Rev. Lett.* **117**, 203001 (2016). Parts of Chapter 4 are based on this publication.

- C.-T. Liao, A. Sandhu, **S. Camp**, K. J. Schafer, and M. B. Gaarde. *Beyond the single atom response in absorption lineshapes: Probing a dense, laser-dressed helium gas with attosecond pulse trains*, *Phys. Rev. Lett.* **114**, 143002 (2015). Parts of Chapter 5 and 6 are based on this publication.

- C.-T. Liao, A. Sandhu, **S. Camp**, K. J. Schafer, and M. B. Gaarde. *Attosecond transient absorption in dense gases: Exploring the interplay between resonant pulse propagation and laser-induced line-shape control*, *Phys. Rev. A* **93**, 033405 (2016). Parts of Chapter 5 and 6 are based on this publication.

- M. Wu, S. Chen, **S. Camp**, K. J. Schafer, and M. B. Gaarde. *Theory of strong-field attosecond transient absorption*, *J. Phys. B* **49**, 062003 (2016). Parts of Chapter 5 and 6 are based on this publication.

- S. Bengtsson, E. W. Larson, D. Kroon, **S. Camp**, M. Miranda, C. L. Arnold, A. L'Huillier, K. J. Schafer, M. B. Gaarde, L. Rippe, and J. Mauritsson. *Space-time Control of Free Induction Decay in the Extreme Ultraviolet*, *Nature Photonics* **11**(4), 252-258 (2017). Parts of Chapter 7 are based on this publication.

# Table of Contents

# List of Figures

# Abstract

We present a theoretical study of the influence of resonant enhancement on high harmonic generation for harmonics near the ionization threshold of helium and argon atoms. This is done by solving the time-dependent Schrödinger equation (TDSE) for the interaction between an atom and a driving laser pulse. By varying parameters of the driving laser pulse, we are able to identify the enhancement of harmonics resulting from multiphoton resonances between the ground state and Stark-shifted excited states of the atom. In this way, spectral and temporal signatures of resonant enhancement are identified and highlighted. We also study trajectory dynamics in HHG. For resonances occurring at the peak intensity of the driving laser pulse, we use time-frequency analysis on the emission to show that both long and short quantum path contributions to the harmonic yield can be enhanced. In this case, we also show that the phase of the long quantum path can be perturbed by the resonant interaction. For resonances occurring at intensities below the peak intensity, we demonstrate a new approach to studying resonant enhancement in both the time and spectral domain. This approach allows us to separate the long and short quantum path spectrally, allowing for unique insight into quantum path dynamics during the interaction with the strong laser field. We compare our results to those of recent experiments and find good agreement.

We also present a theoretical study of the interaction of extreme ultraviolet (XUV) pulses with a resonant macroscopic medium in transient absorption. In order to do this, the coupled TDSE and Maxwell's wave equation (MWE) are solved for an electric field propagating through a gas of atoms. We first show that a resonant medium can act to greatly alter the absorption line shape of an XUV pulse, when the medium is optically thick and the resonance is long-lived. This is demonstrated to be an effect of resonant pulse propagation, a temporal reshaping of light pulses interacting with long-lived resonances (relative to the duration of the pulse). The evolution of this spectral and temporal reshaping with increased propagation distance and gas pressure is investigated, both theoretically and experimentally. We next demonstrate a new optical tool that we have developed for controlling the spatial properties of XUV light. This optical tool uses an infrared pulse to tailor the emission direction of free-induction decay in a gas after a resonant XUV pulse excites the atoms. This technique is explored in both theory and experimental work, demonstrating the spatial control in two different geometries. It is also shown that this technique can be used to spectrally study the atomic response of atoms independently from the excitation pulse. This is a unique scenario, as typically the atomic response is measured as absorption in the spectrum of the excitation pulse.

# Part I

# Resonant interactions in high harmonic generation at the single atom level

# Chapter 1
# High harmonic generation

In this chapter, we give a brief introduction to high harmonic generation (HHG) in gases, a process in which intense, long-wavelength laser light interacting a gas of atoms (nobel gases, typically) generates light with much shorter wavelengths. First, we provide some general background and history on the discovery of HHG. Then we explore concepts necessary for understanding the physics driving HHG, and that will permeate this entire thesis. Finally we discuss the two different ways in which this thesis uses HHG as a tool to study resonant interactions. Note that in this thesis, we generally consider linearly polarized laser pulses interacting with gas-phase atoms, with laser intensities such that we need only to consider the electric field interaction with the atom. That is, magnetic field interactions only become important at laser intensities several orders of magnitude stronger than we consider in this work [1].

## 1.1 Introduction to HHG

A harmonic of an electric field is simply another electric field with a frequency that is an integer multiple of the original frequency. Hence electric fields with frequencies $2f$, $3f$, and $4f$ are referred to as the second, third, and fourth harmonic of an electric field with frequency $f$ (the fundamental), or H2, H3, and H4, in shorthand. In this thesis, we consider only odd order harmonics, since the even orders are forbidden in gas-phase systems with inversion symmetry. As is well known, in free space the relationship between light's frequency, wavelength, and photon energy is given by

$$f = \frac{c}{\lambda} = \frac{E}{h}, \tag{1.1}$$

where $f$ is the frequency of the light, $c$ is the speed of light, $\lambda$ is the wavelength of the light, $E$ is the photon energy of the light, and $h$ is Planck's constant. This implies that the $q$th harmonic of a field with photon energy $E$ and wavelength $\lambda$ will have photon energy $qE$ and wavelength $\frac{\lambda}{q}$. This means that high-order harmonics of low-photon-energy, long wavelength light will be high-photon-energy, short wavelength light. Coherent short wavelength light in the extreme ultraviolet (XUV, from 124 nm to 10 nm) and x-ray regime (10 nm to .01 nm) is desirable for a multitude of uses in spectroscopy and imaging applications [2–6]. Short wavelength light is generally required for the study of atomic excitation and resonances. For example, to promote an electron in helium from its ground state to the $2p$ excited state, one needs a photon energy close to 21.1 eV, or 60 nm light. It is, however, much harder to produce and control short wavelength light than its visible (400 nm to 750 nm) or near infrared (IR, 750 nm to 1400 nm) counterpart, and often requires nonlinear generation processes.

In 1967, it was observed that shining an IR laser through a gas of atoms could be used to produce odd harmonics of the input laser [7]. By todays standard, the intensity of the light was relatively low and only low-order harmonics were observed. In the weak-field (low intensity) limit, the harmonic generation process can be understood in the perturbative regime, as the atom absorbing $q$ photons of the driving field and then emitting a single photon with $q$ times the original photon energy. The probability for this to occur becomes exponentially smaller as $q$ increases. This leads to a rapid decline in harmonic yield as the harmonic order is increased, significantly limiting the number of harmonics that can be generated in this way. Generally, weak-field harmonic generation is only useful for directly generating harmonics up H5, however, atomic resonances (which increases the probability of multiphoton processes) can be used to push this limitation all the way to H11 [8].

Laser design improved, and by the late 1980's scientists were able to push laser intensities into the strong field regime, where the laser-interaction potential is comparable to the atomic potential interaction. In the strong field regime, the number of odd harmonics generated by passing an IR laser through a gas of atoms is greatly increased, allowing for the generation of higher order harmonics, with initial observations showing harmonics all the way up to H33 of a 1064 nm laser [9, 10]. In this strong-field limit, the low-order harmonics still rapidly decrease in intensity with

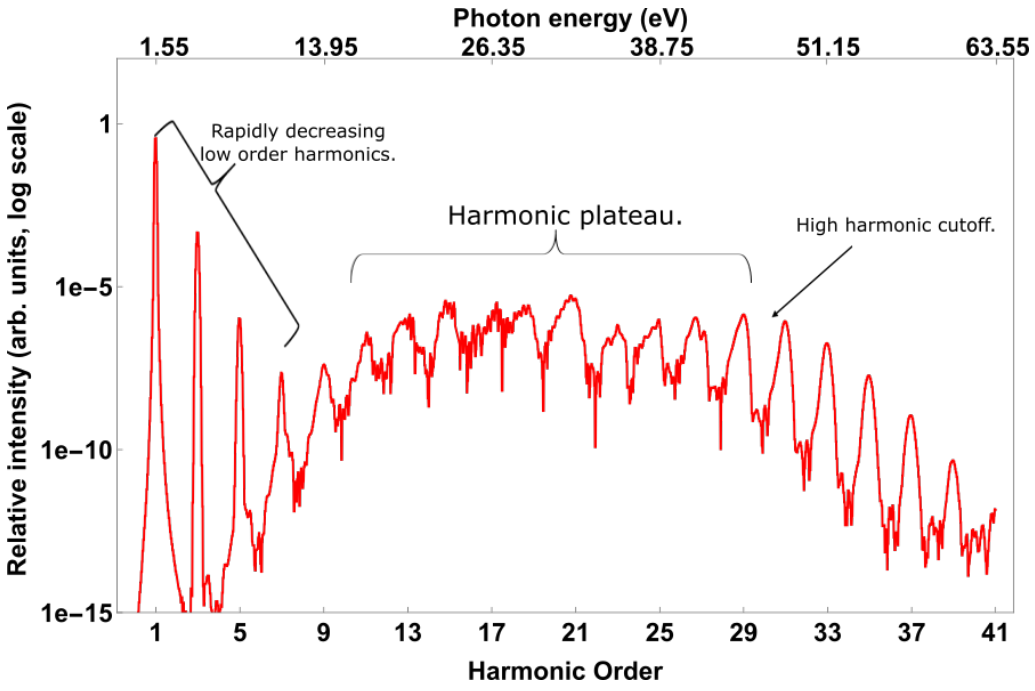


Figure 1.1: Theoretically calculated high harmonic spectrum, calculated for a helium atom interacting with a 20 optical cycle full-width at half-maximum 800 nm pulse with a peak intensity of $10^{14}$ W/cm$^2$. It illustrates the rapidly decreasing low order harmonics (H1-H7), the harmonic plateau (H9-H29), and the high harmonic cutoff at H29. Note that here, HHG allows us to use 1.55 eV light to generate light up to 50 eV.

increased order, but the high-order harmonics behave very differently, forming a plateau of constant intensity up to a high harmonic cutoff, which we discuss more in the next section. This highly nonlinear process is referred to as HHG in gases. We present an example of a typical high harmonic spectrum in Fig. 1.1, showing the rapid decrease in intensity for low-order harmonics, a harmonic plateau of near-constant intensity for high-order harmonics, and the high harmonic cutoff, where the intensity of the harmonics begins to drop. The high harmonic cutoff is given by $E_{cutoff} = I_p + 3.17U_p$, where $I_p$ is the ionization potential of the atom and $U_p$ is the ponderomotive energy of the atom (average oscillation energy picked up by a free electron in a laser field), which is proportional to the intensity of the laser times the square of the laser wavelength ($\propto I\lambda^2$) [11]. We explore the details of this cutoff energy in more detail in the next section.

Since its discovery, HHG has grown in leaps and bounds. Currently, most HHG experiments are performed in rare/nobel gases with laser pulses around 800 to 1000 nm, peak intensities in the range of $10^{13} - 10^{15}$ W/cm$^2$, and pulse durations on the order of 10's of femtoseconds (fs), though they can be as short as 1 optical cycle of the laser, or 2.5 fs at 800 nm [12–16]. IR light sources can be used to reach harmonics with photon energies up to around a few hundred eV [17, 18]. However, there is also a growing push into using intense, few-cycle, mid-IR light sources between 1000 and 4000 nm [5, 15, 19–21]. These longer wavelength light sources can greatly extend the harmonic cutoff [19], and have been used to generate harmonics with photon energies up to 1.5 keV [22]. While the conversion efficiency of HHG is notoriously low, generating harmonics at intensities $5 - 10$ orders of magnitude weaker than the input laser [23], HHG has effectively been applied as a source of coherent XUV light in spectroscopy [24–26], interferometry [27–30], imaging [31–35], studying magnetic properties [36–38] and the development of unique light sources [39–43], amongst many other applications. Further, the harmonic spectrum represents a huge bandwidth of coherent radiation that has been used to create extremely short attosecond (as) ($10^{-18}$ seconds) pulses [44, 45] allowing for the study of electron dynamics [6, 46–48]. In the next section, we discuss HHG in more depth, exploring the physics that allows for the conversion of low-photon-energy IR light into high-photon-energy extreme ultraviolet light (XUV) light.

## 1.2 The rescattering model and quantum trajectories

We can understand the physics driving the HHG process by a semi-classical rescattering model (often referred to as the three-step model throughout this thesis). In this model, the HHG process is broken into three steps [11, 50], which we illustrate in Fig. 1.2. Here we assume the field interacts with a single bound electron at a time and that the field is linearly polarized. The first step consists of the laser field bending the atomic potential, allowing the electron to tunnel ionize outside of the atomic core. In the second step, the newly freed electron is accelerated away from the atomic core by the electric field, before the sign of the field flips and drives the

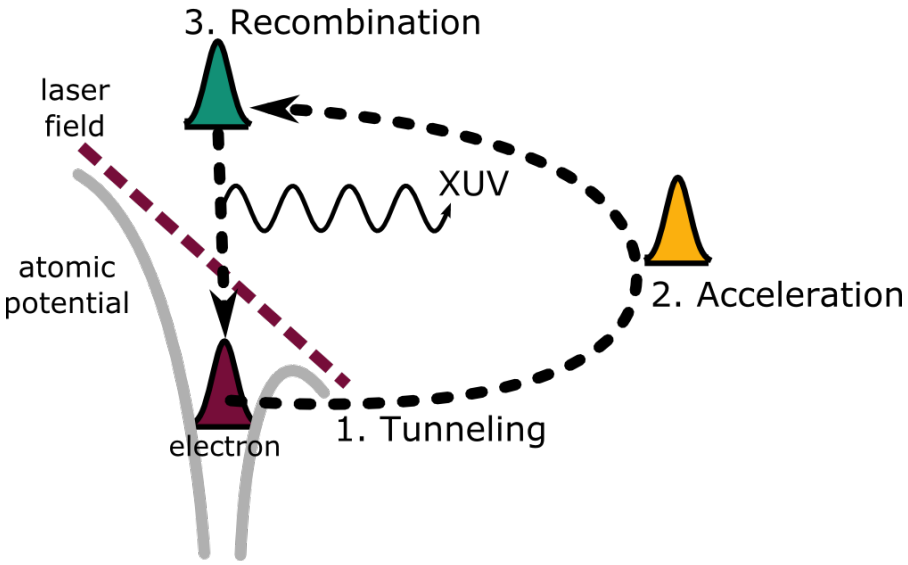


Figure 1.2: The rescattering model for understanding HHG in a gas. The electron is first tunnel ionized from the atomic potential, the free electron is next accelerated by the laser field, gaining energy, and finally the electron recombines with the ionic core, emitting a high-energy-photon. Reprinted from [49], which is released under the Creative Commons Attribution-Share-Alike License 3.0.

electron back to the atomic core. The third and final step consists of the electron recombining to the ground state of the atom. Upon recombination, the excess energy gained by the electron is emitted in the form of a high-energy-photon. The maximum excess energy that can achieved by the electron, and thus the highest energy harmonic that can be generated, is $E_{cutoff} = I_p + 3.17U_p$ [11]. Intuitively, we can break this excess electron energy into two different contributions: a contribution from the energy gained to ionize out of the atomic core ($I_p$) and a contribution from the quiver energy, $U_p$, picked up by the free electron oscillating in the field. While the factor of 3.17 is a little mysterious (we explore it below), it is clear that if the three-step model applies to HHG, then the harmonic cutoff energy must be expressible in this form. And in fact, the three-step model very accurately predicts the experimentally observed high harmonic cutoff energy. Note that the three-step model can also be used to explain why only odd harmonics are observed in HHG in a gas, as this three-step behavior will occur periodically every half cycle of the laser and the Fourier transform of this sort of periodic behavior gives rise to a frequency comb with a spacing of twice that of the cycle frequency. Since our generated spectrum must include a linear response to the original frequency (H1), this gives rise to only odd harmonics [51].

The factor of 3.17 in the high harmonic cutoff law can be obtained from semi-classical calculations based around the idea of the rescattering model [11]. In such calculations, one assumes that the electron initially tunnel ionizes close to the atomic core and has no initial velocity upon escape. Then one calculates classical trajectories for a free electron accelerated by the electric field and considers only trajectories

that return to the core (to recombine). By measuring the kinetic energy of the returning electrons, it is found that the highest possible return energy is $3.17U_p$. For each harmonic with energy less than $3.17U_p$, there are two distinct trajectories giving rise to that particular return energy, a long trajectory and a short trajectory. Long trajectories are born near the peak of the field, travel far away from the core, and return after a long excursion time, whereas short trajectories are born near the zero of the field, stay close to the atomic core, and return very quickly after ionization. Both of these types of trajectories can be seen in Fig. 1.3, where we plot semi-classical calculated trajectories in HHG as a function of return energy (by color). As the return energy approaches the $3.17U_p$ limit, the birth and return times of these two separate trajectories grow closer together until they become a single trajectory at the high harmonic cutoff, which we can also see in Fig. 1.3. At each return energy, each of these quantum trajectories lead to a burst of light every half cycle and, as we increase the return energy, the two bursts of light grow closer together temporally. That is, with increased return energy, the burst of light related to the short trajectory shifts later in the half cycle, while the long trajectory burst shifts earlier. We discuss and observe this emission behavior more in Chapter 2, but it has been previously observed in both HHG experiments [52–56] and HHG

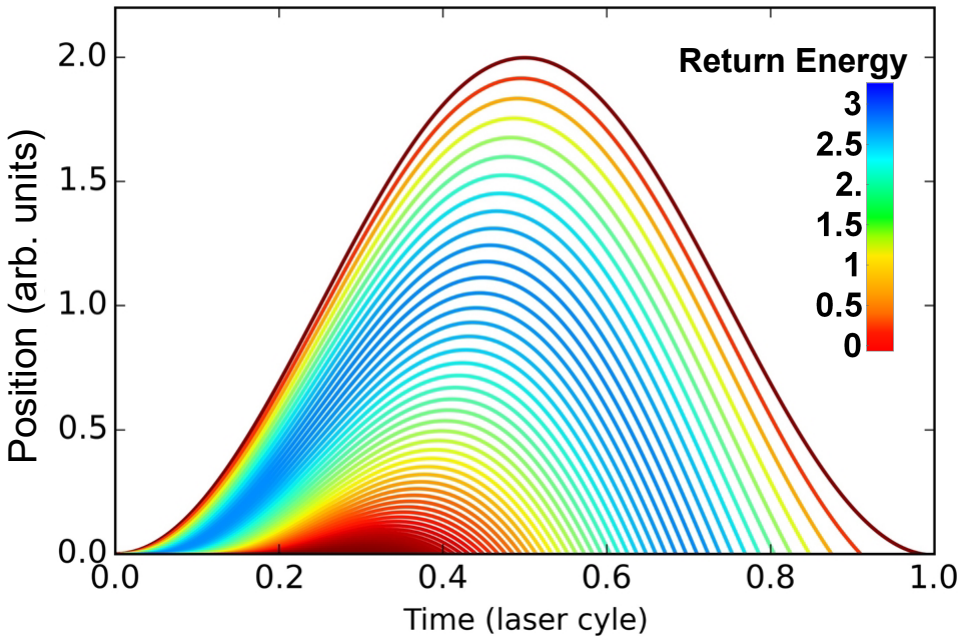


Figure 1.3: Semiclassical quantum trajectories in HHG for a cosine carrier pulse. (a) Recombining classical trajectories that are ionized at different times, from the peak of the field at $t = 0$ to $t = 0.25$ of the laser cycle. Each trajectory is colored by its return energy. This return energy can be related to the slope of the trajectory when it returns to the core. For each return energy, up to the cutoff, there is a trajectory that takes a large amount of time to return (long trajectory) and a trajectory that returns very quickly (short trajectory).

calculations [57–61], serving as evidence for how well the rescattering model works. Isolating the bursts of light related to these quantum trajectories (corresponding to isolating a broadband of frequency in the harmonic spectrum) give us access to attosecond pulses [44, 45], which have been made as short as 67 attoseconds [62], and whose application we discuss in more detail in Chapter 5.

We can calculate the phase accumulated by an electron wave packet traveling along one of these classical trajectories, in order to calculate the phase of the light emitted upon recombination (the phase of the related time-dependent dipole moment) [13]. To do this, we calculate the classical action integral along the trajectory. For a trajectory released into the continuum at $t'$ and returning to the core at $t$, this phase takes the form

$$\phi(t', t) = -\int_{t'}^{t} \mathrm{S}(t'')dt'', \tag{1.2}$$

where $\mathrm{S}(t'') = E_{\mathrm{kin}}(t'') - E_{\mathrm{pot}}(t'')$ is the classical action (kinetic energy minus the potential energy) [13,63]. For a given harmonic, the different birth and return times of the two associated trajectories will lead to different phases. In most cases that we consider in HHG (several cycle driving pulses), this phase can be approximated as being proportional to the driving intensity of the laser [13, 64, 65]. So then for harmonic $q$, we can write the dipole phase of the corresponding long ($l$) and short ($s$) trajectory contributions as

$$\phi_q^{l,s} = \alpha_q^{l,s} I, \tag{1.3}$$

where $I$ is the driving intensity of the pulse, and $\alpha_q^{l,s}$ is a proportionality constant [13, 20, 63]. We illustrate the calculated intensity-dependent phase coefficient for the long (red) and short (black) trajectories in Fig. 1.4. Generally, $\alpha_q^{l,s}$ increases monotonically with time spent in the continuum and varies slowly with return energy

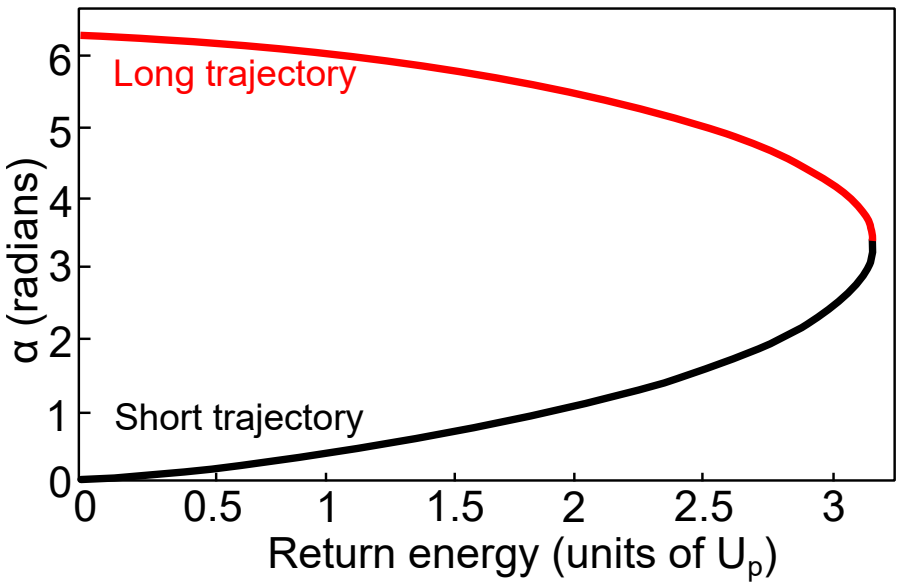


Figure 1.4: Intensity-dependent phase coefficient, $\alpha$, calculated for the long (red) and short (black) trajectories as a function of return energy.

(and thus harmonic order). For plateau harmonics (particularly harmonics with low return energies), the corresponding long and short trajectories have intensity-dependent phases such that $\alpha_q^l \gg \alpha_q^s$, joining together only at the cutoff (where the long and short trajectory merge together) [13, 64–67].

This difference in the intensity-dependent phase for the long and short trajectory contribution to a harmonic leads to different spectral behaviors. The large phase variation on the long trajectory contribution during the driving pulse leads to a large spectral bandwidth, while the small phase variation on the short trajectory contributions leads to a much smaller bandwidth [63, 67–69]. However, these two contributions spectrally overlap and the difference in phase leads to interference in the harmonic spectrum, giving rise to complex structures. This can be observed in the complicated form of the plateau harmonics in Fig. 1.1, whereas the harmonics around the cutoff are spectrally narrow and well-defined, due to the phase of the long and short trajectories growing together (as the two paths merge). This complicated interference structure in the spectrum of the plateau harmonics can make it difficult to study the two trajectories independently. We know that the two trajectories are temporally separated, but the short time scale of the trajectories (a few 100's of attoseconds) can make it complicated to work with them in the time domain. Plus, often HHG experiments are entirely done in the frequency domain with spectrometers, which measures the total amount of incoming light at each frequency, at the cost of integrating out the time information. This would suggest that studying differences in the long and short trajectory contributions to a generated harmonic would be very complicated. Luckily, however, the difference in the

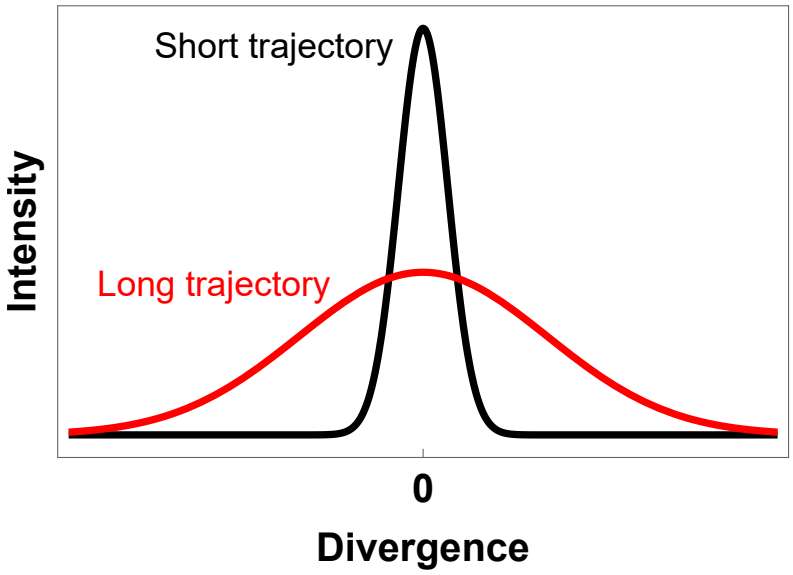


Figure 1.5: Quantitative demonstration of the far-field divergence behavior of the short (black) and long (red) trajectory contributions to a harmonic. The short trajectory is very intense, but spatially narrow, while the long trajectory is weaker, but spatially broader. This difference in divergence can be used to study the two trajectories separately in experimental setups.

intensity-dependent phase of the long and short trajectory contributions leads to the corresponding phase fronts having different curvature in space. This leads to different behavior in the far-field, namely, that the long trajectory emission is much more divergent than that of the short trajectory. We demonstrate these different far-field behaviors in Fig. 1.5. Here the short trajectory corresponds to the very intense, but spatially narrow curve (black) and the long trajectory corresponds to the weaker, but spatially broader curve (red). This separation in the far-field is often used as a simple technique for studying the two trajectories separately [64, 66, 70–73]. While we will not see this spatial separation of the long and short trajectory again in this work, we explore this concept of exploiting the asymmetry in the magnitudes of $\alpha_q^l$ and $\alpha_q^l$ to spectrally separate the respective trajectory contributions to a harmonic in Chapter 4.

### 1.3 HHG as a tool to study resonant interactions

We now turn our attention to the idea of using HHG as a tool for learning about resonant interactions, which is the over-arching theme of this thesis. In this section we touch on two different approaches that have developed around using HHG to get access to information about the electron.

The first approach is the idea of using HHG as simply a source of coherent XUV light. This approach treats HHG as a tool to generate coherent XUV light to be used in other experiments that probe resonant interactions and electron dynamics. This approach has been very fruitful and HHG is now often used as an easy tabletop source of coherent XUV light that can be used to excite and probe atomic resonances in experiments [26, 28, 74–76]. Not only is it useful as a tabletop source of coherent XUV light, but it can also be used to create laser pulses with just a few hundred attosecond durations [44,45]. This is a time scale on par with the motion of electrons in an atom. This is important because any time that a dynamic process is being studied, one needs to be able to observe the process on the time scale that it occurs. These ultrashort duration pulses of light can give us access to the time scale of the electron, allowing for the study of electron dynamics in atoms [44, 45, 77–83]. In this thesis, we make use of this approach in Part II, where we study the resonant interaction of XUV light (generated by HHG) passing through a macroscopic media. We discuss how this is done in more depth and the application of attosecond pulses, in Chapter 5.

In the past decade, a new approach has developed. It has been demonstrated that the light from HHG is much more than just a tool to generate ultrafast, coherent XUV radiation, but also has a wealth of information encoded in it via the generation process itself. During HHG, the XUV photon emitted upon the recombination of the electron to the atom depends sensitively on the dynamics of the electron and the core structure as it ionizes, accelerates, and recombines. This encodes the XUV light with important information about the atomic energy structure, the ionization method of the electron, the dynamics experienced by the electron while it was ionized, and how

it recombined to the parent ion [29,66,67,71,84–88]. This approach goes beyond the simple three steps of the rescattering model, which ignores the atomic interaction with the potential, but often tries to resolve new effects through explaining how the influence of the potential alters the usual three-step process. This is the particular approach that we will use in the rest of Part I to study resonant interactions in HHG.

Techniques to study the high harmonic spectrum and decode dynamic information from it are still being refined and are at the heart of the growing field of high harmonic spectroscopy (HHS) [29, 74, 85, 89–91]. HHS aims to use HHG as a form of spectroscopy to study atomic/molecular structure and electron dynamics. Often this consists of measuring how the harmonic spectrum varies with the parameters of the driving pulse (intensity, wavelength, pulse duration, etc.) or atomic sample (alignment, species, etc.). By relating changes in the harmonic spectrum directly to changes in these parameters, information about dynamics, resonant interactions, and structural information can be gained. HHS can also be extended to studying how the temporal structure of generated harmonics vary, instead of the spectra, which can allow for unique information to be garnered. We will see the application of both these HHS methods in Chapters 3 and 4, where we study near-threshold harmonics to gain insight into the resonant interaction of an electron (in HHG) with Stark-shifted excited states of the atom [67,84]. In order to study the resonant interaction of these near-threshold harmonics, we go beyond the rescattering model and fully incorporate the atomic potential. We do this by calculating the high harmonic spectra through solving the full time-dependent Schrödinger equation (TDSE) for the interaction of an electron, bound in an atomic potential, with a time-dependent strong laser field, which we discuss in more detail in the next chapter.

# Chapter 2
# Numerical methods used in the study of the single atom HHG response

This chapter describes the numerical methods that we use in the study of HHG and strong field interactions throughout this thesis. We begin by carefully outlining the physical problem that we wish to study in HHG, noting that we are working in the single active electron (SAE) approximation; this means that we only ever consider the interaction of a single electron with the strong laser field [92].

The response of an atom to a strong laser field can be characterized by its time-dependent dipole moment, $d(t)$ [93]. The single atom radiation spectrum is then proportional to $\widetilde{\mathcal{D}}(\omega)$, the Fourier transform of $d(t)$, as $\widetilde{\mathcal{D}}(\omega)$ serves as the source term for new electric fields in Maxwell's wave equation. This means we can study the light generated or absorbed by an atom interacting with a strong laser field by calculating $d(t)$. For a laser field polarized along the $z$ direction, the time-dependent dipole moment is given by

$$d(t) = \langle z \rangle = \langle \psi(\boldsymbol{r}, t) | \, z \, | \psi(\boldsymbol{r}, t) \rangle \,, \tag{2.1}$$

where $|\psi(\boldsymbol{r}, t)\rangle$ is the time-dependent wave function for the electron, which is found by solving the TDSE. It turns out that $d(t)$ is numerically complicated to calculate because the $z$ term puts a lot of emphasis on the wave function at large distances from the core, where numerical representations of the wave function can be inaccurate [12]. Instead, we calculate the time-dependent acceleration,

$$a(t) = \frac{\mathrm{d}^2}{\mathrm{dt}^2}\langle z \rangle = -\langle [H, [H, z]] \rangle, \tag{2.2}$$

where the last equality follows from Ehrenfest's theorem and $H$ is the full Hamiltonian including both the interaction with the ion core and the laser field [13, 57, 58]. This is a much easier calculation, numerically, because $a(t)$ contains the same information as $d(t)$, but is weighted more heavily near the core, where we expect our numerical representation of the wave function to be much more accurate [12].

Having $a(t)$, we can calculate the acceleration spectrum, $\widetilde{\mathcal{A}}(\omega)$, using a Fourier transform given by

$$\widetilde{\mathcal{A}}(\omega) = \int a(t) W(t) e^{i\omega t} dt. \tag{2.3}$$

Here $W(t)$ is a window function that smoothly brings the time-dependent acceleration to zero at the end of the calculation. The purpose and applications of this window function will be discussed in more depth in section 2. With $\widetilde{\mathcal{A}}(\omega)$, we can

calculate the dipole spectrum using the relationship [13, 57],

$$\widetilde{\mathcal{D}}(\omega) = \frac{-\widetilde{\mathcal{A}}(\omega)}{\omega^2}. \tag{2.4}$$

We should note that whenever we discuss showing the harmonic spectrum from a single atom in this work, we are showing $|\widetilde{\mathcal{A}}(\omega)|^2$.

This chapter focuses on discussing the numerical techniques that we use in the study of the above outlined problem. In section 1, we discuss the numerical techniques used to calculate the time-dependent wave function, $|\psi(\boldsymbol{r}, t)\rangle$, describing the electron as it interacts with the strong laser field and how we use this wave function to calculate $a(t)$. In section 2, we discuss the different temporal window functions we apply to $a(t)$ when calculating the spectrum in Eq. (2.3). Finally, in section 3, we discuss the spectral window functions we apply when using the inverse Fourier transform, in order to study temporal dynamics of the electron during its interaction with the field.

## 2.1 Calculation of the single atom response to a laser pulse

In the length gauge, using atomic units such that $e = \hbar = m_e = 1$ and assuming that the driving laser field has a wavelength much larger than the atomic length scale, we can apply the dipole approximation and write the TDSE using the classical electron-field interaction as

$$i\frac{\partial}{\partial t}|\psi(\boldsymbol{r}, t)\rangle = \left[-\frac{1}{2}\nabla^2 + V(\boldsymbol{r}) + (\boldsymbol{\mathcal{E}}(t)\cdot\boldsymbol{r})\right]|\psi(\boldsymbol{r}, t)\rangle\,, \tag{2.5}$$

where $V(\boldsymbol{r})$ is the atomic binding potential, and $\boldsymbol{\mathcal{E}}(t)$ is the time-dependent electric field vector [13, 57, 93]. Though this is the TDSE for a single electron interacting with a laser, it can be used broadly to simulate one-electron effects in multielectron atoms by carefully choosing the atomic binding potential so that it leads to the correct singly excited states of that electronic system [12]. This relies on the SAE approximation; that the laser field only strongly interacts with one of the atom's valence electrons at a time [92]. The SAE approximation, intuitively, applies well to atomic systems where a single valence electron sits outside of a closed shell, such as alkali metal atoms. However, it also applies well to any case where it is not very likely that multiple electrons will be excited at once, which is generally true in the strong-field limit in which harmonics are generated. In the noble gases, the SAE approximation has been shown to be valid for most cases where the driving laser photon energy is below the ionization potential of the singly excited electron [12, 92, 94, 95].

In solving the TDSE, we make use of the fact that if we know the wave function at an initial time $\tau$, then the time propagation of $|\psi(\boldsymbol{r}, \tau)\rangle$ for a small time step $\delta t$

is given by

$$|\psi(\boldsymbol{r}, \tau + \delta t)\rangle = e^{-i(H_0+H_I)\delta t} |\psi(\boldsymbol{r}, \tau)\rangle \,, \tag{2.6}$$

where the full Hamiltonian $H$ has been split into two terms, the field-free, time-independent Hamiltonian $H_0$ and the time-dependent electron-laser interaction Hamiltonian $H_I$, which is evaluated at the midpoint of the time step [93, 96]. In our calculations we always start with a well defined initial state, the ground state of the atomic system that we are interested in, so our algorithms for finding the time-dependent wave function are built around Eq. (2.6), which can be rewritten in an approximate form that maintains the unitary property and is accurate to $\mathcal{O}(\delta t)^3$ as

$$|\psi(\boldsymbol{r}, \tau + \delta t)\rangle \approx e^{-iH_I\delta t/2} e^{-iH_0\delta t} e^{-iH_I\delta t/2} |\psi(\boldsymbol{r}, \tau)\rangle \,. \tag{2.7}$$

Now we can use the Crank-Nicolson technique [97] to approximate the exponential operators into a more malleable form for us to use, while maintaining the same order of accuracy numerically, by approximating the field-free Hamiltonian exponential operator as

$$e^{-iH_0\delta t} \approx [1 + iH_0\delta t/2]^{-1}[1 - iH_0\delta t/2] \tag{2.8}$$

and the interaction Hamiltonian operator as

$$e^{-iH_I\delta t/2} \approx [1 + iH_I\delta t/4]^{-1}[1 - iH_I\delta t/4]. \tag{2.9}$$

Assuming that we expand our wave function in a basis set, we have now reduced the problem of time propagation to one of solving a system of equations of the form

$$\vec{z} = \boldsymbol{A}\vec{y}, \tag{2.10}$$

$$\boldsymbol{B}\vec{x} = \vec{z}, \tag{2.11}$$

where $\boldsymbol{A}$ and $\boldsymbol{B}$ are matrix operators, $\vec{y}$ is a known vector, and $\vec{x}$ is some unknown vector. Time propagation consists of solving systems like this multiple times per propagation step for the different operators, but this is a well-researched problem and there are many algorithms that one can apply to the problem. The only question left is the form of the operators $H_0$ and $H_I$, which depend on the basis that we expand our wave function into. Because of the form of the $\boldsymbol{\mathcal{E}}(t) \cdot \boldsymbol{r}$ term in the TDSE, we handle this expansion differently for linearly and elliptically polarized fields, which we illustrate below.

### 2.1.1 Linearly polarized driving fields

For the case of linearly polarized fields, we use the approach described in detail in [12]. Here we assume that

$$\boldsymbol{\mathcal{E}}(t) = F(t)\mathcal{E}_0 \cos(\omega t)\hat{z}, \tag{2.12}$$

where $\omega$ is the frequency of the driving laser field, $\mathcal{E}_0$ is the peak field strength, and $F(t)$ is an envelope function that starts the field at zero, smoothly brings it up to the peak field strength of $\mathcal{E}_0$ for some duration of the pulse and then back to zero. We discuss the envelope function we typically use in more detail in Chapter 3. This assumption allows us to simplify the TDSE to the form

$$i\frac{\partial}{\partial t}\psi(\boldsymbol{r},t) = \left[H_0 + z\mathcal{E}(t)\right]\psi(\boldsymbol{r},t). \tag{2.13}$$

We now discretize the TDSE and time-dependent wave function. To do this, we first expand $\Psi(\boldsymbol{r},t)$ in spherical coordinates using the spherical harmonics multiplied by radial functions as a basis for our expansion. This gives

$$\psi(\boldsymbol{r},t) = \sum_{\ell,m}\psi_\ell(r,t)Y_\ell^m(\theta,\phi). \tag{2.14}$$

In the case of linear polarization, this basis has the benefit that the $m$ quantum number of the initial wave function is conserved. Going forward, we assume that the initial orbital of the interacting electron is aligned with the field, such that $m = 0$. This means we get a full three-dimensional treatment for the computational cost of only solving two dimensions. Discretizing the wave function in $r$ on a radial grid $r_j = (j - 1/2)\Delta r$ for $j = 1...n_r$ and in $Y_\ell^0(\theta,\phi)$ for $|\ell\rangle = |0\rangle \ldots |\ell_{max}\rangle$, we get

$$|\psi(r_j,\theta,t)\rangle = \sum_{\ell=0}^{\ell_{max}}\psi_\ell(r_j,t)\,|\ell\rangle. \tag{2.15}$$

Note that during time propagation we use an absorbing mask near the edges of our grid to prevent unphysical reflections of the wave function off these boundaries.

Using this form for the wave function, making the transformation $\phi_l^j = r_j\psi_l^j$, and using a variational technique with the discretized wave function inserted into a Lagrange-type functional, one can derive the discrete form of the operators $H_0$ and $H_I$ acting on the wave function in $r$ and $\ell$ as [12],

$$[H_0\phi]_\ell^j = \frac{-1}{2(\Delta r)^2}\left[\alpha_j\phi_\ell^{j+1} - 2\beta_j\phi_\ell^j + \alpha_{j-1}\phi_\ell^{j-1}\right] + V_\ell^j\phi_\ell^j, \tag{2.16}$$

$$[H_I\phi]_\ell^j = \mathcal{E}(t)r_j\left[c_\ell\phi_{\ell+1}^j + c_{\ell-1}\phi_{\ell-1}^j\right], \tag{2.17}$$

where the dimensionless terms $\alpha_j$, $\beta_j$ and $c_\ell$, are

$$\alpha_j = \frac{j^2}{j^2 - 1/4}; \beta_j = \frac{j^2 - j + 1/2}{j^2 - j + 1/4}; c_\ell = \sqrt{\frac{(l+1)^2}{(2l+1)(2l+3)}}, \tag{2.18}$$

and $V_\ell^j$ is our pseudopotential, discretized on our $\ell$ and $r_j$ grid, that recreates the field-free energy levels of the atomic system that we are interested in studying. For the noble gases that we consider in this work (in the linear polarization case), $V_\ell^j$ is constructed by the methods outlined in [12]. We calculate the $\ell$ dependent potential

for the three lowest $\ell$ (0, 1, and 2) and then use the $\ell = 2$ potential for $\ell > 2$. We can now calculate the acceleration using Eq. (2.2), by using that in this coordinate system the $z$ operator takes the form

$$z = c_\ell \left|\ell + 1\right\rangle \left\langle \ell\right| + c_{\ell-1} \left|\ell - 1\right\rangle \left\langle \ell\right|, \tag{2.19}$$

where we implicity assume the summation over all $\ell$.

### 2.1.2 Elliptically polarized driving fields

In order to calculate HHG by elliptically polarized driving fields, we have implemented a new numerical approach to the problem with the hope of extending the work demonstrated in this thesis to elliptical driving fields. To do this we use a method similar to one proposed by Marangos *et al.* [98], but that makes use of techniques developed by Schafer for the linear polarization problem [12]. In this case our electric field takes the form

$$\boldsymbol{\mathcal{E}}(t) = E_x(t)\hat{x} + E_y(t)\hat{y} = F(t)\frac{\mathcal{E}_0}{\sqrt{1+\epsilon^2}}\left[\cos(\omega t)\hat{x} + \epsilon\sin(\omega t)\hat{y}\right], \tag{2.20}$$

where $F(t)$ is an envelope function, and $\epsilon$ is our ellipticity parameter. $\epsilon$ varies from $\epsilon = -1$ for left circularly polarized light to $\epsilon = 1$ for right circularly polarized light with $\epsilon = 0$ being the linearly polarized case. Note that we have chosen the normalization of the field such that the cycle averaged intensity of the field is independent of $\epsilon$. In the length gauge, the TDSE now simplifies to the form,

$$i\frac{\partial}{\partial t}\psi(\boldsymbol{r}, t) = \left[H_0 + xE_x(t) + yE_y(t)\right]\psi(\boldsymbol{r}, t). \tag{2.21}$$

Because we now have an $x$ and $y$ term in the TDSE, the solution of Eq. (2.21) is more easily done in cylindrical coordinates rather than the spherical coordinates that we used for the linearly polarized case. Making the transformation

$$\mathcal{E}_\pm = E_x(t) \mp iE_y(t), \tag{2.22}$$

we can rewrite the TDSE in cylindrical coordinates $(\rho, \phi)$

$$i\frac{\partial}{\partial t}\psi(\boldsymbol{r}, t) = \left[H_0 + \frac{\rho}{2}\{\mathcal{E}_+ e^{i\phi} + \mathcal{E}_- e^{-i\phi}\}\right]\psi(\boldsymbol{r}, t). \tag{2.23}$$

In these two dimensions we can discretize the wave function and the TDSE, however, there are no conserved quantities in these coordinates that will give us a free dimension this time. This means that in order to stay in two-dimensions, we choose to ignore the $z$-coordinate in this problem.

With these assumptions, we can expand our wave function in this basis as

$$\psi(r_j, \phi, t) = \sum_m \psi_m(\rho, t) \frac{e^{im\phi}}{\sqrt{2\pi}}, \tag{2.24}$$

and now the path to discretization is clear. We expand our wave function on a grid in the $\rho$ coordinate $\rho_j = (j - 1/2)\Delta\rho$ for $j = 1...n_\rho$ and in $\frac{e^{im\phi}}{\sqrt{2\pi}}$ for $|m\rangle = |-m_{max}\rangle ... |m_{max}\rangle$ and get

$$\psi(\boldsymbol{r}, t) = \sum_{m=-m_{max}}^{m_{max}} \psi_m(\rho_j, t) |m\rangle. \tag{2.25}$$

As in the linear polarization case, during time propagation we use an absorbing mask at the edge of the grids to prevent unphysical reflections of the wave function. Now using the variational method described in [12] and making the transformation $f_m^j = \sqrt{\rho}\psi_m^j$, we can write the discrete form of the Hamiltonian operators as

$$[H_0 f]_m^j = \frac{-1}{2(\Delta\rho)^2} \left[\gamma_j f_m^{j+1} - 2f_m^j + \gamma_{j-1} f_m^{j-1}\right] + \frac{m^2}{2\rho_j^2} f_m^j + V_j f_m^j, \tag{2.26}$$

$$[H_I f]_m^j = \frac{\rho_j}{2}\{\mathcal{E}_+ f_{m+1}^j + \mathcal{E}_- f_{m-1}^j\}, \tag{2.27}$$

where the dimensionless term $\gamma_j$ is

$$\gamma_j = \frac{j}{\sqrt{j^2 - 1/4}}, \tag{2.28}$$

and $V_j$ is our pseudopotential, discretized over our $\rho$ grid, that well recreates the field-free energy levels of the atomic system [98].

Having finished the discretization of the Hamiltonian operators, we discuss the method for calculating the dipole acceleration. For this system we actually want to calculate the dipole spectra for both the $x$ and $y$ coordinate, separately. Because of the discretization that we chose and the intermingling of $E_x$ and $E_y$, this is not as simple as in the linear polarization case, but can be done straightforwardly using Eq. (2.2) if we note that the operator $e^{\pm i\phi}$ can be expressed as

$$e^{\pm i\phi} = \sum_{m=-\infty}^{\infty} |m \pm 1\rangle \langle m| \approx \sum_{m=-m_{max}}^{m_{max}} |m \pm 1\rangle \langle m|, \tag{2.29}$$

where the equality arises from using the entire $m$ basis, which ranges from $-\infty$ to $\infty$, and the approximation arises from our numerical need for a finite $m$ range to consider. Combining this expression for the operator with the relationships in this coordinate system gives us

$$x = \rho\cos(\phi) = \rho\{e^{i\phi} + e^{-i\phi}\}/2, \tag{2.30}$$

$$y = \rho\cos(\phi) = \rho\{e^{i\phi} - e^{-i\phi}\}/(2i). \tag{2.31}$$

With this relationship and the discretization of the Hamiltonian operators, calculating the expectation value of $e^{\pm i\phi}$ can be used to construct $\langle x\rangle$ and $\langle y\rangle$. Note that elliptically polarized fields will not be discussed again in this thesis, as this method has not yet lead to published results.

## 2.2 Transforming the dipole acceleration to the frequency domain with different temporal window functions.

The previous section was dedicated to the numerical techniques used for calculating the time-dependent wave function, which we needed in order to calculate the time-dependent acceleration, $a(t)$. In this section we are going to discuss different temporal window functions that we apply to $a(t)$ before transforming it to the frequency domain. These allow us to control the temporal contributions from $a(t)$ to $\widetilde{\mathcal{A}}(\omega)$. Numerically, we do the Fourier transform from $a(t)$ to $\widetilde{\mathcal{A}}(\omega)$ in Eq. (2.3) by using stadard numerical tools for the discrete fast Fourier transform (DFFT) [99,100]. The resulting acceleration spectrum depends sensitively on the choice of temporal window function. This allows us to use various $W(t)$ in order to serve different purposes. These purposes range from numerical to tailoring the information in our generated spectrum to a specific problem, allowing for additional insight into the dynamics of the laser-electron interaction.

A DFFT takes a discrete time signal and Fourier transforms it into a discrete frequency representation by assuming that the original discrete time signal is periodic. This means the beginning of the time signal should be continuous with the end. When this is not true, it can introduce numerical issues that result in large amounts of noise and unphysical effects in the resulting spectrum [99,101]. For our problem it is the case that $a(t)$ starts at zero at the beginning of our calculation, but does not return to zero at the end of the calculation, breaking this periodicity assumption. Numerically we get around this problem by using a window function that smoothly goes to zero at the beginning and end of our signal, making the signal periodic [99,101]. An appropriate window function can also have the added benefit of allowing for much cleaner high harmonic spectra by emphasizing the signal near the maximum of the laser pulse, where the HHG that we are interested in occurs, while de-emphasizing any signal near the beginning and end of the laser pulses, which could introduce noise to the spectrum. We demonstrate some of these numerical effects of our window function in Fig. 2.1.

In Fig. 2.1(a), we show three different window functions (dashed lines) and their respective product with $a(t)$ (solid lines) calculated for a helium atom interacting with a strong laser pulse. In red we show a constant window

$$W(t) = 1, \tag{2.32}$$

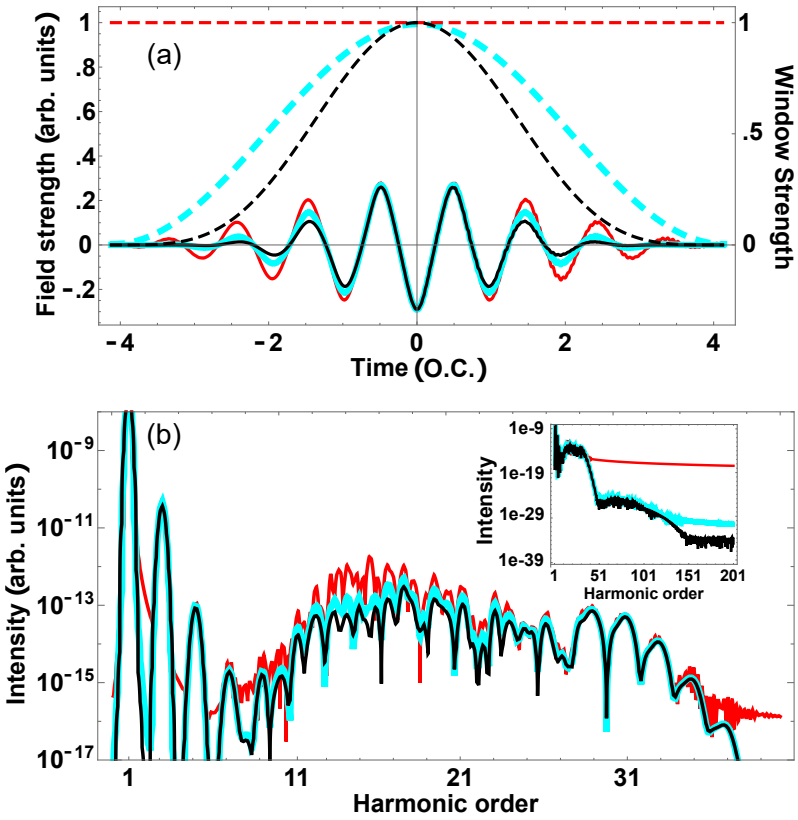


Figure 2.1: (a) 3 different window functions (dashed) and their corresponding product with $a(t)$ calculated for a helium atom interacting with an 8 optical cycle (O.C.) total duration, cosine squared pulse with a peak intensity of $10^{14}$ W/cm$^2$. Red corresponds to a constant window function, blue corresponds to a Hanning window function that smoothly goes to zero at the beginning and end of the calculation, and black corresponds to the square of the Hanning window function. (b) The corresponding (by color) harmonic spectra plotted up to just beyond the high harmonic cutoff. The inset shows a zoomed out plot to a much higher frequency, demonstrating the noise floor of the respective calculations.

and in blue we show a Hanning window,

$$W_H(t) = .5(1 + \cos(\frac{\pi t}{\tau_H})), \tag{2.33}$$

where $\tau_H$ is chosen to bring the window to zero at the beginning and end of our calculation. In black we show $W_H(t)^2$. The constant window function calculation allows us to compare the spectral result of not windowing $a(t)$ to the spectral result of windowing it. In Fig. 2.1(b), we show the corresponding (by color) harmonic spectrum. Here we see that the unwindowed $a(t)$ leads to a spectrum that is much more noisy and disagrees significantly with the spectra resulting from the other window functions. In fact, the spectrum from the unwindowed $a(t)$ does not seem to be able to resolve high frequency, low strength signals, as the spectrum can be seen

at the end of the harmonic plateau reaching a noise floor on the signal resolution. As shown in the inset of Fig. 2.1(b), the noise floor of the spectra from the Hanning and squared Hanning window functions is much lower, with the Hanning windowed noise floor being only slightly higher than squared Hanning window noise floor. For the problems considered in this thesis, we will often use a Hanning window. However, there are problems in HHG that require a much lower signal noise floor which make use of squared Hanning windows, such as HHG in solids, which exhibit weak second and third, high frequency plateaus that a Hanning window can fail to resolve [102].

The reason that $a(t)$ does not go to zero at the end of our laser pulse is primarily, ignoring any other numerical effects, because the strong laser field populates dipole-coupled excited states in our atom [12, 13, 64, 84]. In real life, this excited state population would induce spontaneous emission that decayed with the lifetime of the excited state, allowing the atom to relax to its ground state [96]. In our calculations, this excited state population has no mechanism for decay and will live forever, inducing a tail in $a(t)$ that gives rise to narrow contributions in the harmonic spectrum at the energies of these populated excited states. Even if we did include spontaneous decay of these excited states, the time scale of the decay would be much longer than the time scale that we consider in our calculations, as these lifetimes typically occur on the nanosecond scale and we consider tens of femtoseconds [103]. A temporal window function allow us to effectively put a lifetime on these excited states and end their coherence with the ground state. The shorter lifetime that we

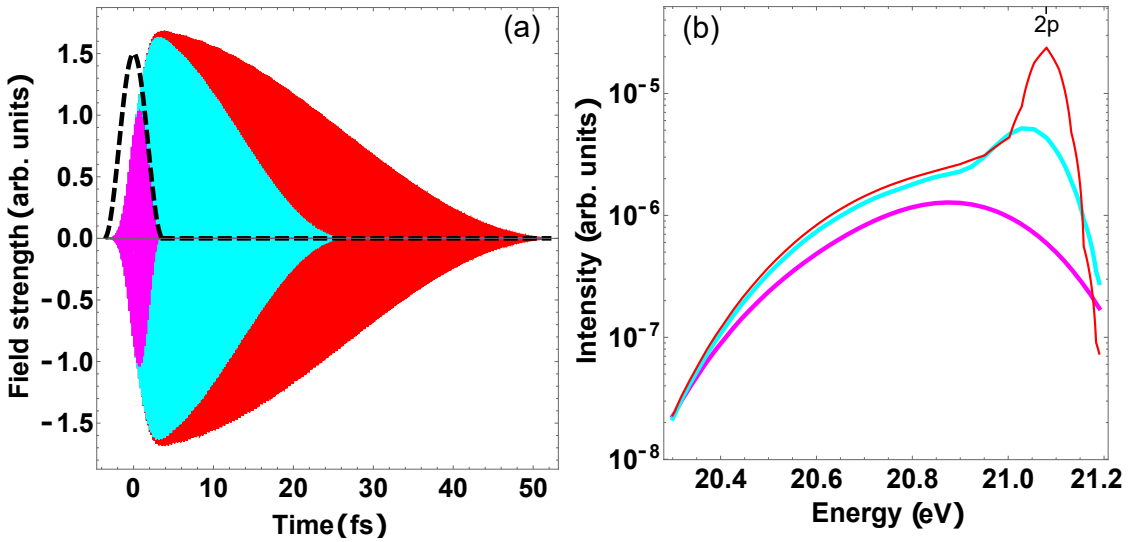


Figure 2.2: (a) $a(t)$ calculated in helium after an interaction with a $10^9$ W/cm$^2$, 2 O.C. XUV pulse with a central frequency overlapping the $2p$ energy level of helium. We show the XUV intensity profile with the black dashed line and $a(t)$ multipled by three different Hanning windows to impose different lifetimes on the resonance. The Hanning windows begin at $-5$ fs, increasing to 1 at $t = 0$, and then either end at 5 fs, 25 fs, or 50 fs and the product with a(t) is shown in purple, blue, and red, respectively. (b) shows the corresponding (by color) harmonic spectrum around the resonant energy. The $2p$ energy is labeled along the top axis.

impose is an acceptable approximation, as we are interested in dynamics induced by the IR and not dynamics happening over the natural lifetime of the excited state.

Beyond ending this coherence, however, the window function gives us some control over the resulting harmonic spectrum. By varying the effective lifetime on the state, we can choose how much of a contribution from these excited states that we include in the harmonic spectrum. In Fig. 2.2(a) we show $a(t)$ for a helium atom interacting with an XUV pulse whose central frequency occurs at 20.86 eV, and spectrally overlaps the $2p$ energy level of helium (intensity profile given by the dashed black line) and windowed by three different Hanning windows. The Hanning windows is chosen to be asymmetric, and begin at $-5$ fs, increase to 1 at $t = 0$ and then end at either 5 fs, 25 fs, or 50 fs, and their products with $a(t)$ are shown in purple, blue, and red, respectively. Note the oscillation at the resonant frequency is too fine to be resolved on the time scale that we consider here, and we discuss this more in depth in the next section. We show the corresponding harmonic spectra (by color) in Fig. 2.2(b). Here we see that as we increase the effective lifetime of the excited state with the window function, we add in a narrow resonant harmonic contribution to the spectrum from the excited state. It is clear that if we were not (were) interested in this contribution, then we could use a short (long) lifetime window to remove (include) it. This gives us a lot of control over the resonant contribution to the harmonic spectrum.

This sort of control knob on the harmonic spectrum can allow us great insight into the dynamics of the electron during the strong field interaction and will be a running theme in later chapters of this thesis. For example, if we know that a physical process only occurs during the first or last half of a laser pulse, then we can use a temporal window that extends to only that duration, in order to learn about the frequency components of the process. We can use these temporal windows to effectively turn on or off the signal from atomic resonances. This can be an invaluable amount of control when trying to use the harmonic spectrum to learn about ultrafast electron dynamics during HHG [84]

## 2.3 Returning the dipole acceleration spectrum to the time domain with different spectral window functions.

In the previous section, we looked at how we could use $a(t)$ to calculate the harmonic spectrum, and discussed how we could use different temporal window functions to study the spectral contributions of different parts of $a(t)$. In this section we discuss how we can use spectral window functions to study the temporal contributions of different parts of $\widetilde{\mathcal{A}}(\omega)$. This is important because electron dynamics explicitly occur in the time domain, and thus the frequency domain can often be confusing for studying these effects. By choosing which frequencies that we are interested in, and looking at the dynamics responsible for their creation, we can bring some clarity.

To return $\widetilde{\mathcal{A}}(\omega)$ to the time domain, our inverse Fourier transform takes the form

$$A(t) = \frac{1}{2\pi}\int \widetilde{\mathcal{A}}(\omega)W(\omega)e^{-i\omega t}d\omega, \tag{2.34}$$

where $W(\omega)$ is now a spectral window function. If we let $W(\omega) = 1$, then $A(t)$ is simply the temporally windowed time-dependent acceleration used in the calculation of $\widetilde{\mathcal{A}}(\omega)$. This section is designed to illustrate some of the temporal information that can be gained when using non-constant $W(\omega)$. We will see that just as temporal windowing gave us control over the generated spectral signal, this spectral window can give us control over the generated temporal signal.

Let us begin our discussion of spectral windowing by looking at a very useful application. In Fig. 2.2(a), we plotted $a(t)$ over a long time scale and saw that the oscillations were much too rapid to be finely resolved. However, we were not interested in the rapid oscillations, but rather how the strength, or envelope, of the oscillations varied over the long time scale. Using spectral windowing, we can generate $A(t)$ in such a way that $|A(t)|$ shows only the slowly varying envelope of our signal, effectively removing the fast oscillations and leaving only the much slower varying amplitude envelope of the signal.

In order to do this, we use a Hilbert spectral window function in the form

$$W_H(\omega) = \begin{cases} 0, & \omega < 0 \\ 1, & \omega = 0 \\ 2, & \omega > 0. \end{cases} \tag{2.35}$$

This window may seem unintuitive in the frequency domain, but in the time domain it has the equivalence of taking an oscillatory time signal like $R(t)\cos(\omega t)$ and using Hilbert transforms to generate a signal in the form of $R(t)e^{i\omega t}$ [104]. The amplitude of this new complex signal would then only varies as $R(t)$, with the fast oscillations of $cos(\omega t)$ removed. We demonstrate this in Fig. 2.3, where we plot the intensity of a temporal signal (red), and the resulting intensity envelope (black dashed line) after Hilbert windowing the original signal. For the rest of this section, and often throughout this work, we will focus only on the envelope of time signals, removing the rapid oscillations in this way.

We now look at a different application of using these spectral windows, one related to learning about actual time dynamics of the electron during the strong field interaction. For this section, we consider only quadratic windows in the form [13, 19, 57, 84]

$$W_q(\omega, \omega_L, \omega_H) = \begin{cases} 0, & \omega < \omega_L \\ \frac{-8(\omega-\omega_L)(\omega-\omega_H)}{(\omega_H-\omega_L)^2}, & \omega_L \leq \omega \leq \omega_H \\ 0, & \omega > \omega_H. \end{cases} \tag{2.36}$$

Here $\omega_L$ and $\omega_H$ are the lower and upper frequency bounds on our spectral windows, respectively, and the center of our window occurs at their midpoint, $\frac{\omega_L+\omega_H}{2}$. This

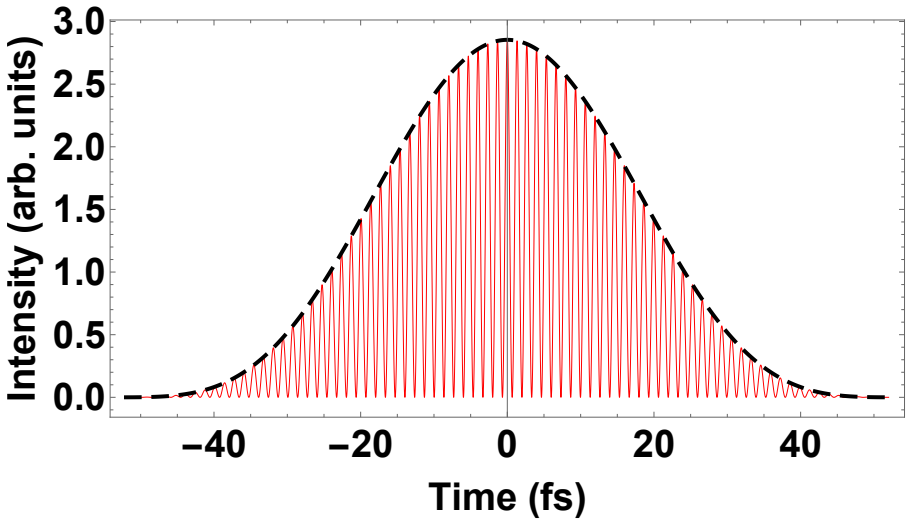


Figure 2.3: The intensity of a time signal with a fast oscillation (red) and the intensity envelope (black dashed line) after the original time signal is Fourier transformed to the frequency domain, has a Hilbert window applied to it, and is then inverse Fourier transformed back to the time domain.

spectral windows rises smoothly from zero at the edges of the window to a maximum of 2 at the center. This form is chosen to smoothly cut out the portion of the spectrum that we are interested in, while introducing minimal numerical noise into our inverse Fourier transform. This spectral window also has the added benefit of applying the Hilbert spectral window to our data for free, since it zeroes out the negative frequencies and we have normalized it to a maximum value of 2.

In Fig. 2.4(a), we show a harmonic spectrum calculated for an argon atom interacting with an intense, few cycle 800 nm IR pulse. With the black dotted box, we illustrate the spectral width of 5 harmonics, H19 to H27. Note that the box ranges from $\omega = 18$ to $\omega = 28$ in order to capture the entire bandwidth of the edge harmonics. In order to look at the time domain contribution from this portion of the spectrum, we apply $W_q(\omega, 18, 28)$ to $\widetilde{\mathcal{A}}(\omega)$ and inverse Fourier transform back to the time domain. We show the resulting $|A(t)|^2$ in Fig. 2.4(b) (alternating red and black line). The time units on this plot are in optical cycles of the driving laser field (at 800 nm, so 1 O.C. is 2.6 fs). We see that this broad spectral window has generated a sequence of bursts of XUV light that last about 260 attoseconds each. The time axis being in optical cycles also allows us to clearly see that we get two bursts of light, both a red and black peak, every half cycle of the driving laser field.

This behavior of two bursts of light every half cycle should bring back memories of discussions from Chapter 1, related to long and short trajectories. In the three step model, when the electron returns it gives off a burst of XUV light and, for a given return energy, there are two returns every half cycle. Note that the burst of light resulting from the electron returning to the core, occurs over a very short time duration. Because of the Fourier relationship between time and frequency, we expect this short temporal burst of light to correspond to a broad spectral signal.

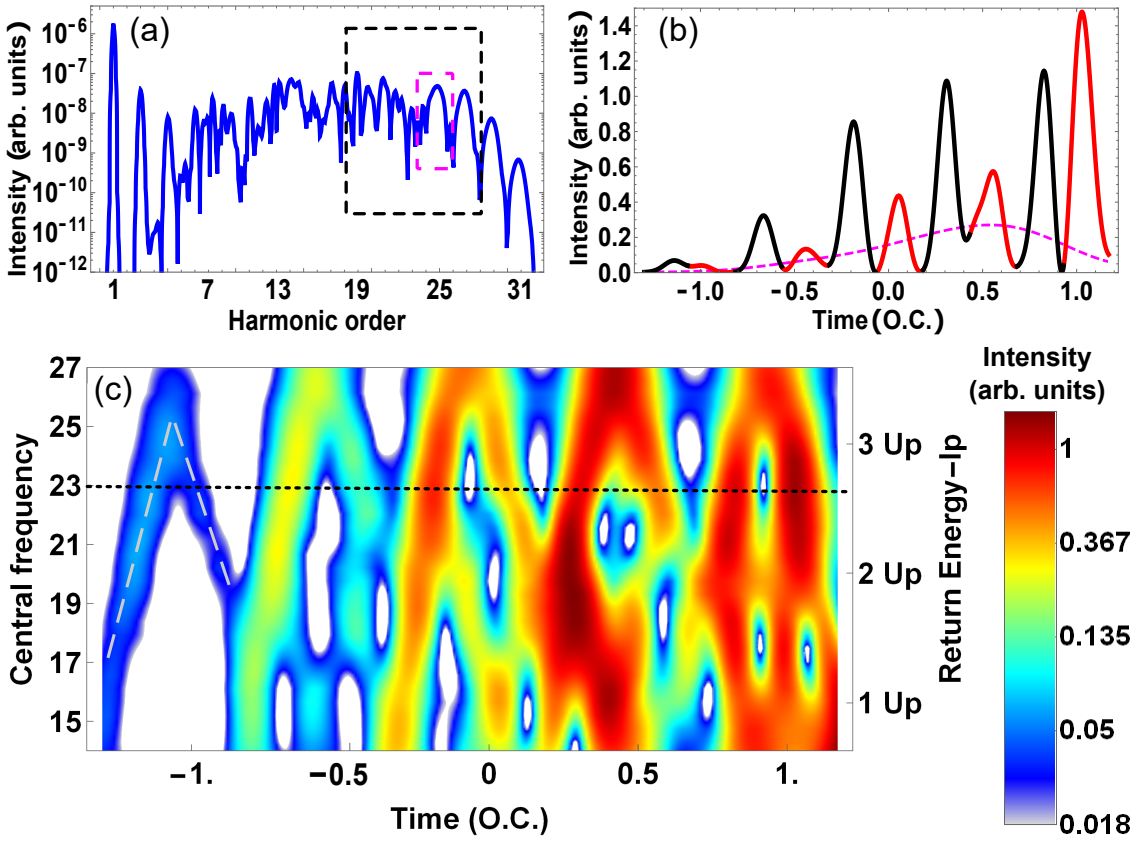


Figure 2.4: (a) A harmonic spectrum calculated for an argon atom interacting with an 8 O.C. total duration, cosine squared pulse with a sine carrier envelope. The thin black (purple) box demonstrates a spectral width of 5 (1) harmonics (harmonic) centered on H23 (H25). (b) The alternating red and black line shows the resulting temporal envelope of the wide spectral window in (a), demonstrating long (red) and short (black) trajectory behavior of two light bursts per half cycle. The dashed purple line shows the resulting temporal envelope of the narrow spectral window of H25. (c) A time-frequency plot generated by scanning the central frequency of the broad spectral window from harmonic frequencies 14.5 to 27. The black dotted line marks the subcycle lineout shown in (b), whereas the gray dashed lines demonstrate the attochirp with increased energy of the long (negative) and short (positive) trajectories. Also observed is the effect of much longer trajectories that occur after the first half cycle and complicate the time frequency interpretations. This figure was inspired from work in [57].

Now it becomes clear that this broad spectral window is giving us the ability to see the bursts of light that occur when the electron returns to the core. The two bursts of light in each half-cycle in Fig. 2.4(b) correspond to long and short trajectories of the electron during HHG. However, this single transformation does not have enough information in it to truly assign each burst of light to either the long or short trajectory. We could make educated assignments, depending on the timing of the bursts with respect to the peak of each oscillation of our driving pulse, but by

sliding the central frequency of our spectral window, we can explicitly assign each burst to a long or short trajectory, as well as see other trajectory dynamics. We demonstrate this in the following paragraph.

In Fig. 2.4(c), we do this transform multiple times, sliding the central frequency of our window from $\omega = 14.5$ to $\omega = 27$. The thin, black dashed line illustrates the lineout shown in Fig. 2.4(b). Now we can see clearly that the red (black) bursts of light from Fig. 2.4(b) shift later (earlier) in time with increased XUV pulse energy until they join together at around $I_p + 3.2U_p$. This shifting in time is known as the attochirp (demonstrated with the dotted gray line), and we know from the three-step model that long (short) trajectories have a negative (positive) attochirp [105]. This allows for the assignment of the red (black) bursts of light to the long (short) trajectories. Note that the first half cycle trajectories observed in Fig. 2.4(c), are very simple showing only a single long and short trajectory, whereas half cycles from later in the pulse become and more complicated. This can be due to trajectories even longer than the long trajectory, resonant effects, or other dynamics. Using this sort of window to get at this trajectory information of the electron makes this technique extremely useful.

We now turn our attention away from broad spectral window of several harmonics, and shift toward more narrow spectral windows. Here we focus on single harmonics. In Fig. 2.4(a), the purple box highlights the spectral width of H25 from $\omega = 24$ to $\omega = 26$. We use a spectral window of $W_q(\omega, 24, 26)$ and show the resulting $|A(t)|^2$ with the dashed purple line in Fig. 2.4(b). As we would expect, this narrow spectral window results in a signal that is temporally broader than the temporal signal of the broader spectral window. The broad spectral window led to an immediate interpretation that we were studying trajectory dynamics, so what are we studying with this narrow spectral window? Here we have direct information about the time that H25 was generated, which we could not infer from the broad spectral windowed signal, or from $a(t)$ itself. Information about the time of generation for a harmonic can be used in many ways, such as for studying resonant effects in specific harmonics by tracking how the temporal behavior of the harmonic changes as we change various pulse parameters.

These narrow spectral windows are not limited to the bandwidth of a single harmonic, but can also be used to select more narrow spectral features and look at them in the time domain. We can use these narrow windows to look at specific resonances, in order to see the long ringing dipole tail and study how it is perturbed by macroscopic propagation or the interaction with an IR pulse. We can also use them to select features in the harmonic spectrum that we might not understand and try to gain insight into what process is driving the feature by looking at what time during the pulse the feature is generated, and how this changes with different parameters. These narrow spectral windows can be quite helpful in separating and studying the temporal properties of different harmonic contributions, which can be greatly useful when studying resonant behavior at specific harmonic energies.

## 2.4 Summary

In this chapter we have discussed the numerical techniques that we use in order to calculate the single atom response to a strong laser field. We have also discussed the window functions that we use in order to gain physical information about the electron dynamics during that interaction with the laser field. In the following chapters of this thesis, the techniques for calculating the single atom response will be occurring mostly in the background, whereas the use of different window functions will come to the forefront and take the main role in our analysis. We will make use of various windowing functions in the time domain to study the spectral contributions of different temporal parts of $a(t)$. We will use spectral window functions to do trajectory analysis, as well as for studying the temporal behavior of specific harmonics, and selecting narrow spectral features to study their temporal dynamics and identify their generating mechanism in the electron dynamics. These will be the primary tools that we use to study resonant interactions of the electron during the strong field in the following chapters of this thesis.

# Chapter 3
# Resonant enhancement and quantum path dynamics in helium.

With the groundwork laid in the previous two chapters, we are now ready to begin discussing the influence of resonances in HHG. Our investigations into this topic center on the interplay of quantum trajectories and resonant enhancement via multiphoton Stark-shifted resonances [84]. The work presented in this chapter focuses primarily on how resonances can influence and alter the quantum trajectories of near-threshold harmonics in helium. This is an energy regime where the three-step model is ill-defined and the driving physics behind the HHG process is still unclear [106]. In this chapter we consider only resonances that occur near the peak of our driving laser pulse, leaving the study of effects related to the temporal wings of the driving laser pulse for the next chapter.

We divide the discussion into two parts: the frequency domain and the time domain. In the frequency domain we systematically study the high harmonic spectrum as a function of intensity and wavelength, in order to identify resonant enhancements in the harmonic spectrum and relate them to the responsible $np$ Stark-shifted resonance of helium. We also find that we can use resonant enhancement in the frequency domain to gain insight into the atomic structure, revealing energy level splittings due to near resonant couplings of nearby energy levels. In the time domain we look at the temporal structure of the harmonic emission, both on and off resonance, in order to study how resonances can alter the quantum path dynamics of the electron. In doing this, we identify temporal signatures of the resonantly enhanced high harmonic generation (REHHG) process and we relate these signatures to possible changes in the electronic ionization dynamics of the three-step model.

## 3.1 Frequency domain: Identifying resonant enhancement in HHG.

In this chapter we constrain ourselves to consider only linearly polarized laser fields with a time-dependent electric field given by

$$\mathcal{E}(t) = \mathcal{E}_0 \cos^2(\frac{c_2 t}{\tau}) \cos(2\pi t), \tag{3.1}$$

where $\mathcal{E}_0$ is the peak electric field, $c_2 = 2\arccos(\frac{1}{2}^{\frac{1}{4}})$, $t$ has been converted to units of optical cycles of the driving laser field, and $\tau = 6$ O.C. is the full width at half-maximum (FWHM) duration of the pulse. Note that we assume the field is zero for $|t| > \frac{\tau\pi}{2c_2}$. Using this form for the electric field and a helium pseudopotential that

well reproduces the energies and oscillator strengths of the singly excited states of helium, we calculate the time-dependent acceleration as outlined in Chapter 2. We then calculate the acceleration spectrum as

$$\widetilde{\mathcal{A}}(\omega) = \int a(t) W_H(t) e^{i\omega t} dt, \tag{3.2}$$

where the Hanning window $W_H(t)$ is given by

$$W_H(t) = .5(1 + \cos(\frac{\pi t}{\tau_H})). \tag{3.3}$$

For most of this work, we let $\tau_H = \frac{\tau\pi}{2c_2}$, which means we only consider the time-dependent acceleration over the extent of the laser pulse. However, we also show some calculations where $a(t)$ lasts for approximately 20 O.C. after the end of the laser pulse, which allows us to consider the excited state population contributions to $a(t)$, as we saw in Chapter 2. For this, we use an asymmetrical Hanning window in the same form as Eq. (3.3) but where we allow $\tau_H$ to vary as

$$\tau_H = \begin{cases} \frac{\tau\pi}{2c_2}, & t < 0 \\ \\ \frac{\tau\pi}{2c_2} + 20 \text{ O.C.}, & t \geq 0. \end{cases} \tag{3.4}$$

We define resonant enhancement as occurring when, for a given driving intensity of a pulse, the yield of a harmonic is larger (enhanced) at one wavelength, relative to the yield of nearby wavelengths, due to a multiphoton resonance between the ground state and an excited state [84, 107, 108]. While the field is on, the atomic energy levels will experience a Stark-shift, typically increasing in energy ponderomotively [93]. This increase in energy leads to Stark-shifted multiphoton resonances occurring at shorter wavelengths (higher energy) than the field free resonances would occur. In this work, we consider resonances that directly agree with the energies of the generated harmonics (odd multiphoton resonances), however, we have previously observed even multiphoton resonances leading to enhancements of harmonics through indirect processes. For a purely ponderomotive energy shift of the $np$ states in helium, this means that we expect resonant enhancement for the $n$th harmonic to occur when the following equation is true:

$$|E_{np} - E_0| + U_p = n\hbar\omega, \tag{3.5}$$

where $E_{np}$ is the field-free energy of the $np$ state, $E_0$ is the field-free energy of the ground state of helium, $U_p$ is the ponderomotive energy shift, $n$ is an odd integer, and $\hbar\omega$ is the energy of the driving laser. Note that when this equation is satisfied, we do not always observe that the $n$th harmonic is enhanced, but if we do then we refer to it as a direct resonant enhancement of harmonic $n$. If this equation is satisfied and we find that a nearby harmonic $m$ is enhanced, then we refer to this as an indirect resonant enhancement of harmonic $m$. Both of these effects can be

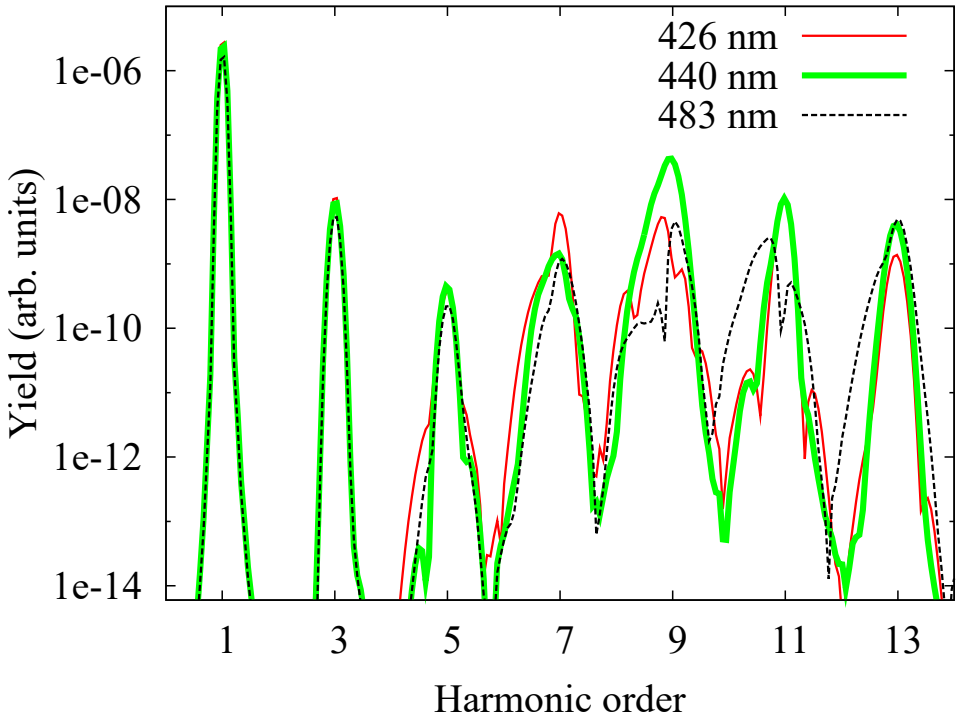


Figure 3.1: Comparison of the harmonic spectra at different driving wavelengths for a driving intensity of 140 TW/cm$^2$. We show the spectra, on a log scale, for three different driving wavelengths as a function of harmonic order. Reprinted from [84] with permission.

observed in Fig. 3.1, where we show the harmonic spectra for driving wavelengths 426, 440, and 483 nm for a peak intensity at 140 TW/cm$^2$. This is an atypical wavelength regime to study, as most HHG experiments have been performed using wavelength in the IR regime. However, we have been motivated to look at shorter wavelengths by recent experiments [109]. There are two clear enhancements of the spectrum illustrated in this figure, H9 at 440 nm and H7 at 426 nm. Evaluating Eq. (3.5) over these wavelengths and at this intensity, it turns out that both of these enhancements are due to a nine-photon resonance between the ground state and a Stark-shifted energy level. At 440 nm, a nine-photon resonance with the Stark-shifted $3p$ state leads to the direct resonant enhancement of H9, and at 426 nm, a nine-photon resonance with the $4p$ state leads to the indirect enhancement of H7. It is currently unclear why a nine-photon resonance can lead to an enhancement of H7 and not enhance H9, however, we clearly observe the effect here.

These enhancements can be seen more clearly by examining Fig. 3.2(a) and (b). Fig. 3.2(a) shows the harmonic yield as a function of driving wavelength and harmonic energy for a Hanning window that lasts only over the duration of the laser pulse. Here we have marked H7, H9, and H11 with dashed white lines and the enhancements of H9 at 440 nm and H7 at 426 nm are easy to identify and are obviously part of larger enhancement structures for these harmonics around these wavelengths. One can even identify another enhancement structure in H7,

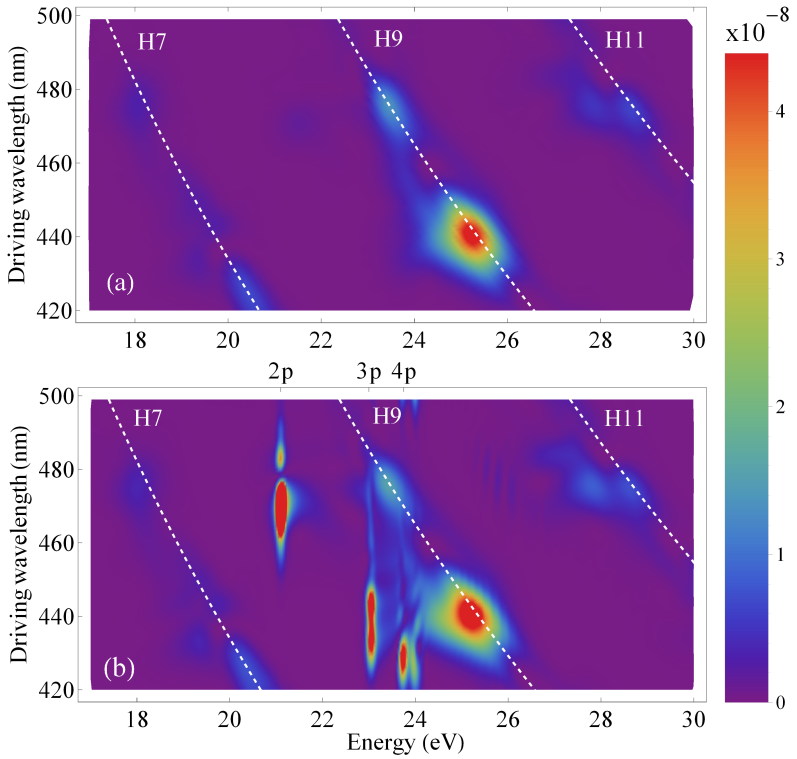


Figure 3.2: Comparison of the harmonic spectra at different driving wavelengths for a driving intensity of 140 TW/cm$^2$. (a) shows the spectra as a function of driving wavelength and energy for a Hanning window that matches the duration of the pulse. (b) shows the spectra as a function of driving wavelength and energy for a Hanning window that allows the time-dependent dipole to live for approximately 20 optical cycles after the pulse ends. The white dotted lines in (a) and (b) mark the position of H7-H11 as a function of driving wavelength. In (b) we have indicated the field-free energies of the $2p$-$4p$ states. Borrowed from [84].

H9, and H11 around 480 nm. Tying these enhancement structures to Stark-shifted resonances can be done by considering Fig. 3.2(b), which shows the resulting spectra if we allow the excited state population to contribute to the dipole response for 20 O.C. after the end of the laser pulse by using the asymmetrical Hanning window outlined above. The spectrum now exhibits features that are strong, narrow, and constant in energy at the labeled field-free $np$ energies. These features are directly associated with population being transferred into these states at the time of the field-driven resonance. Similar features have been recently experimentally observed in the harmonic spectrum of argon [67]. Thus we can use these features to identify which state is primarily responsible for a given resonant enhancement structure. For example, the enhancement of H9 at 440 nm is clearly related to a large population transfer to the $3p$ state, as we would expect from evaluating Eq. (3.5) at this wavelength. Also note that as we increase the driving wavelength in Fig. 3.2(b), we observe that H9 moves into resonance with lower lying energy states.

The ponderomotive energy shift, $U_p$, is proportional to $I\lambda^2$, where $I$ is the inten-

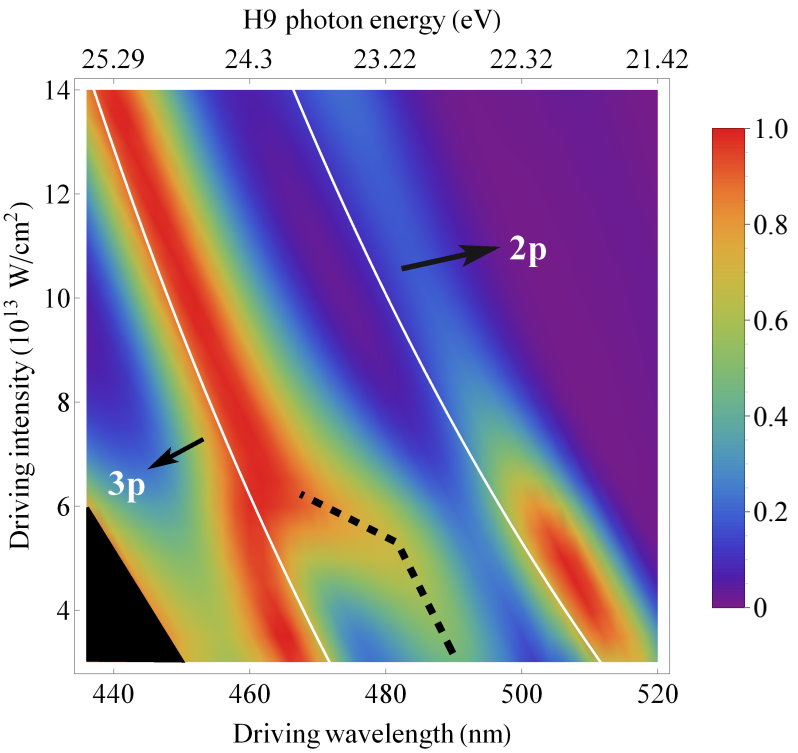


Figure 3.3: H9 spectrally integrated yield as a function of driving wavelength and intensity. For each intensity, the spectrum has been normalized. The white lines represent the photon energies of the resonant enhancements due to the $2p$ and $3p$ states predicted by Eq. (4). The dark dotted line highlights the lower energy feature of an Autler-Townes splitting of the $3p$ feature (see text). Reprinted from [84] with permission.

sity of the driving laser and $\lambda$ is the wavelength of the driving laser. This means that we can gain more insight into the relationship between the resonant enhancement of a harmonic and Stark-shifted multiphoton resonances, if we study the harmonic yield as both a function of driving wavelength and peak driving intensity [109]. In order to do this we calculate the harmonic spectra at a given intensity for a range of driving wavelengths, using a Hanning window only over the lifetime of the pulse. We then integrate the harmonic spectrum associated with each driving wavelength around the bandwidth of that harmonic and normalize the entire wavelength scan to have a maximum value of 1. This normalization allows for the direct comparison of high and low peak intensities, whose true harmonic yields will differ by orders of magnitude. We show the result of this for H9 in Fig. 3.3. The white lines in this figure represent the photon energies of direct resonant enhancements to H9 due to the $2p$ and $3p$ states predicted by Eq. (3.5). The $2p$ enhancement of H9 generally agrees well with the $2p$ predicted line, and the $3p$ enhancement feature agrees well with the $3p$ predicted line for moderate to high intensities, with the disagreement between the structures and the lines arising from the excited states shifting slightly less than ponderomotively. We also find similar agreement of enhancement struc-

tures following ponderomotive curves in H7 and H11 (not shown). However, the low intensity dependence of the $3p$ enhancement disagrees with our curves, showing two unique enhancement features. We explore this below.

The $3p$ enhancement feature splitting into two features at low intensities can be understood as a sort of generalized Autler-Townes energy splitting due to a near-resonant one photon coupling between the $3p$ and $2s$ states induced by the driving laser field [110]. The Autler-Townes effect refers to an energy level splitting that occurs when a strong field couples the ground state to an excited state and a second, weaker, field couples that excited state to a different excited state. The reason that it has to be understood as a generalized Autler-Townes splitting here is because we do not use two fields. Instead we couple the ground state to the $3p$ state with nine photons of our driving field, and then couple the $3p$ state to the $2s$ state with a single photon. We note that when this figure was published in [84], we believe it is the first time that an Autler-Townes splitting was characterized using only a harmonic spectrum. The fact that we can observe this energy splitting in the harmonic spectrum is interesting and indicative of exactly how much important atomic information that we can garner by carefully studying the light generated from HHG around threshold.

## 3.2 Time domain: Studying the temporal influence of resonant enhancement on HHG and quantum paths.

In the frequency domain we were able to identify resonant enhancements of the high harmonic spectrum. By studying the population left in excited states and the wavelength-intensity dependence of these harmonic enhancements, we were able to attribute these enhancements to specific nine-photon resonances between the ground state and Stark-shifted energy states. This work, however, told us nothing about the actual dynamics of the electron during this enhancement process since we were looking at values that were inherently time integrated, removing any time-dependent dynamical information. To study these dynamics, we must shift back to the time domain. We can now use what we learned in the frequency domain as a roadmap for where to look for signatures of the enhancement process in the temporal structure of the emitted XUV light. These signatures of the resonant enhancement process will be what we use to gain insight into the electron dynamics that occur in REHHG.

In order to study the emitted XUV light in the time domain, we follow our previously spelled out recipe from Chapter 2. We select a range of frequencies, $\omega_L$ to $\omega_H$ in $\widetilde{\mathcal{A}}(\omega)$ and inverse Fourier transform those frequencies back to the time domain. Our transform takes the form

$$A(t) = \frac{1}{2\pi} \int \widetilde{\mathcal{A}}(\omega) W_f(\omega, \omega_L, \omega_H) d\omega, \tag{3.6}$$

where we refer to $|A(t)|^2$ as the time profile for the range of frequencies we have

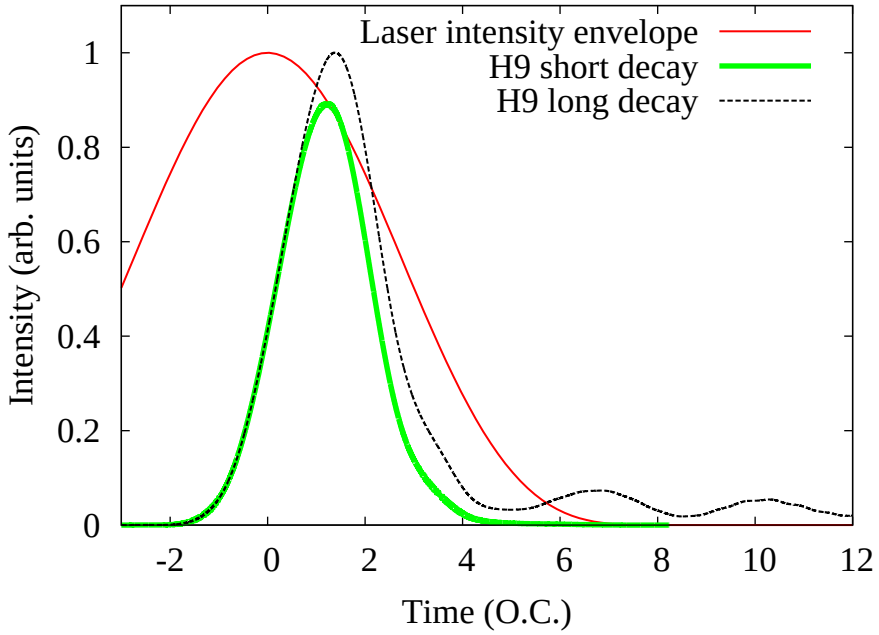


Figure 3.4: H9 time profile at 440 nm and 140 TW/cm$^2$ in helium with the (scaled) intensity envelope of the driving pulse, for the short and long Hanning windows. The time axis is in units of O.C. of the driving pulse. Reprinted from [84] with permission.

selected. $W_f(\omega)$ is a quadratic Hilbert frequency window in the form

$$W_q(\omega, \omega_L, \omega H) = \frac{-8(\omega - \omega_L)(\omega - \omega_H)}{(\omega_L - \omega_H)^2}, \tag{3.7}$$

where we implicitly assume $W_f(\omega)$ is zero outside of the chosen range of frequencies. Recall that if the frequency range only encompasses a single harmonic, then $A(t)$ represents when that harmonic was generated during the driving pulse. In contrast, if the frequency range encompasses several harmonics, then we will learn about the subcycle time dynamics (long and short trajectories) generated by the electron ionizing and returning to the core.

We begin by looking at the time profile of the $3p$-enhanced H9 at 440 nm and 140 TW/cm$^2$ using a $2\omega$-wide frequency window centered on H9. We show this in Fig. 3.4 for the two different Hanning windows that we consider in Fig. 3.2 (a) and (b). We first observe that the different Hanning windows make very little difference to the coherent, driven harmonic response generated near the peak of the driving field (shown in red). The difference in the magnitude of the two peaks is purely due to the different scaling imposed by the Hanning window at those points. The long Hanning window H9 profile shows a long oscillating tail that does not arise in the short Hanning window H9 profile. This long tail, as we observed in Chapter 2, is a result of population being left in excited states with a dipole connection to the ground state and gives rise to the narrow spectral features that we observed in Fig.

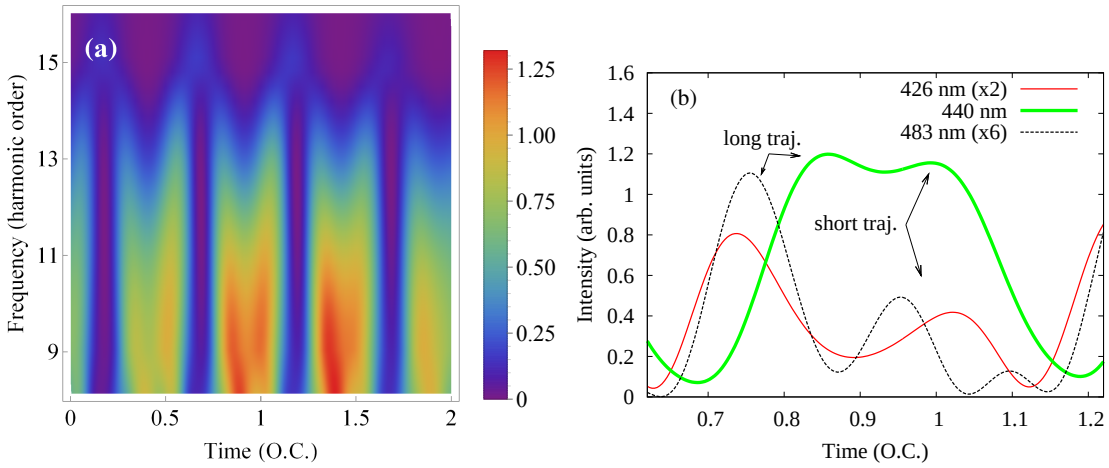


Figure 3.5: (a) Time-frequency profile of the harmonic radiation for a driving wavelength of 440 nm and intensity of 140 TW/cm$^2$, when H9 is resonant with the Stark-shifted $3p$ state. (b) Line-outs of the time-profile of H9 for driving wavelengths of 426 nm, 440 nm, and 483 nm. Note that the long and short trajectory emission peaks in (b) belong to successive half-cycles of the driving field as can be seen in (a). Reprinted from [84] with permission.

3.2(b). The oscillation in this tail would not occur if population was left in only one excited state and occurs here due to quantum beating between population left in the $3p$ and $4p$ states, whose energy difference give rise to a beat period of close to 4 O.C. of the IR pulse. This quantum beating process was recently experimentally observed using transient absorption in neon [111] and investigated theoretically for transient absorption in helium [112]. In terms of REHHG electron dynamics, we find that for the resonantly enhanced case, the peak harmonic emission occurs at 1 O.C., whereas the non-resonantly enhanced case (not shown) occurs peaked at .5 O.C. We suspect that this difference in behavior is caused by delayed ionization of the electron due to getting trapped in the excited state prior to ionization [113,114], which can cause delayed harmonic emission by a half cycle, but would still result in the traditonally expected long and short trajectory subcycle emission peaks that we still observe to occur in the resonantly enhanced case (demonstrated below). The other option for the observed delay, the electron getting trapped in an excited state upon return, is not very likely because this would not result in emission times corresponding to the long and short trajectory returns.

Fig. 3.5(a) illustrates the subcycle time-frequency profile at 440 nm and 140 TW/cm$^2$ using a $12\omega$ window with the central frequency of our frequency window varying between H8 and H16. We see that it follows the predictions of the three-step model, with central frequencies below the high harmonic cutoff showing two dominant emission peaks per half cycle that grow into a single emission peak at the high harmonic cutoff [40, 115, 116]. The earlier peak corresponds to the short trajectory returns and the later peak corresponds to the long trajectory returns. How well this works near and below the ionization threshold is somewhat surprising, as we expect the three-step model to break down in this energy regime, but yet we

see well defined trajectories all the way down to a central frequency of H8, which is well below the ionization threshold. This points towards us being able to take these near-threshold trajectories and compare the cases of resonantly enhanced to not resonantly enhanced, in order to identify the effect that the resonance has on the quantum trajectories.

Fig 3.5(b) shows lineouts centered on H9 of the time-frequency profile for the non-resonantly enhanced cases of 426 nm and 483 nm and the resonantly enhanced case of 440 nm. We have labeled the long and short trajectories in all three cases using time-frequency profiles like Fig. 3.5(a) and have chosen the time window such that we are looking at the long trajectory from one half cycle and the short trajectory from the next half cycle (these two trajectories do not grow together at the cutoff). We see that the enhancement on resonance leads equally to enhancements of both the long and short trajectory. One is not seemingly preferred over the other. We also see interesting time-dependence of this emission. For a constant frequency lineout in a time-frequency profile, one expects successive long and short trajectories, such as we are looking at in Fig. 3.5(b), to smoothly grow closer together as one increases the driving wavelength [19, 105, 117]. This means that the short trajectory should smoothly shift earlier in the cycle and the long trajectory should smoothly shift later in the cycle. We observe this action in Fig. 3.5(b) for the short trajectory, however, the long trajectory experiences a strong variation from this expectation around the resonant wavelength of 440 nm. That is, the contribution from the long trajectory at 440 nm is shifted much later in the cycle than the contribution from the long trajectory at 483 nm. This corresponds to a phase shift of the long trajectory, on resonance, of $\pi/4$.

Fig. 3.6 shows the H9 subcycle time profile as a function of driving wavelength. We overlay the plot with the approximate expected emission times of the short and long trajectory at the different driving wavelengths by connecting the trajectories at the lowest and highest non-resonant wavelengths. Starting at the bottom of Fig. 3.6, we see that as we vary the driving wavelength from 420 nm to 440 nm, the contribution from the long trajectory smoothly shifts later in the cycle by approximately 1/8 O.C. As we increase the driving wavelength above the 440 nm resonant case, we actually reach a point where we can no longer make out clear long and short trajectories, which is the case that one might actually expect from these low order harmonics. We then find the resurgence of an obvious long and short trajectory contribution as the driving wavelength increases to around the $2p$ resonant enhancement feature at 475 nm. At longer wavelengths (not shown), we find similar results as H11 comes into resonance with the Stark-shifted energy levels: the long and short trajectories are only recognizable for wavelengths near the resonant wavelength and as we tune our wavelength into resonance, the long trajectory can experience a sudden phase shift to later in the cycle.

This subcycle time behavior allows us to infer multiple things about the electron dynamics that are going on during the REHHG process. It suggests that for harmonics near the ionization threshold, where we expect the three-step model to break down, we can expect the electron to follow traditional three-step model behavior, if the near-threshold harmonic is near a Stark-shifted resonance. The fact that both

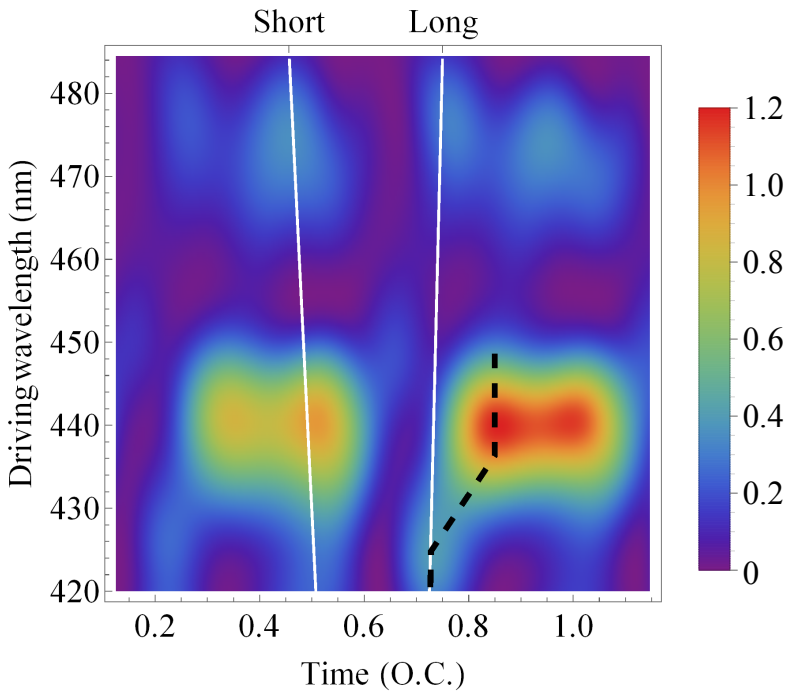


Figure 3.6: Sub-cycle time profile of the radiation centered on H9 as a function of driving wavelengths spanning the $3p$ and $2p$ resonant enhancement features, which are located at 440 nm and 470 nm for this intensity. The white lines are an approximate measure of the expected emission times for the short and long trajectory emission peaks. Reprinted from [84] with permission.

the long and short trajectory are enhanced on resonance can be used to point to the enhancement occurring during the ionization stage by a multiphoton resonance with the Stark-shifted energy state. We can also interpret the phase shift on the long trajectory as occurring during the recollision step, as the long trajectory spends a long time in the continuum and samples the entire spatial extent of the potential upon return, whereas the short trajectory returns very quickly after ionization. Our work also suggests that we can relate this phase shift to specific resonances, as we found that the phase shift of the long trajectory of both H9 and H11 was approximately the same for resonances with the same states.

## 3.3 Summary

By identifying specific wavelengths and intensities where resonant enhancement occurs, we have been able to look at how the resulting time profiles of the harmonic emission change when a resonance is involved. We have seen that despite being near and below the ionization threshold, around these resonances we can find the familiar long and short trajectory dynamics of the three-step model. On resonance we find that these trajectories are both greatly enhanced, suggesting that the res-

onance helps the electron ionize out of the ground state of our atom. We also find that the resonant interaction can leave distinct signatures on its interaction with the electron. On the subcycle level, we see this signature resulting in a phase shift of the subcycle emission related to the long trajectory, while on the single harmonic level we find that the signature results in delayed emission of our harmonic.

This all speaks to the interplay of the quantum trajectories and resonant enhancement. The resonant interaction does not drive the harmonic process for these near-threshold harmonics, but rather assists in freeing the electron to follow the natural three-step model behavior driven by the field. At wavelengths far from a resonance, we do not observe obvious long and short trajectories, but for wavelengths close to the resonance (but not resonant), the resonant interaction assists in the ionization and leads to our ability to very clearly see distinct below and near-threshold long and short trajectories. At wavelengths on resonance, population can be directly moved into the excited state and ionize from there, greatly increasing the yield of these trajectories while leaving a temporal signature of the resonant interaction on the generated harmonic, as well as leading to a phase shift on the long trajectory recombination.

# Chapter 4
# Spectral and temporal signatures of resonant enhancement.

In the previous chapter, we identified and studied resonant enhancement of the harmonic yield as we varied the driving wavelength. This proved a fruitful technique for identifying resonant enhancement in our calculations, however, most experimental studies are performed using fixed wavelength laser sources. Only recently have developments in laser technology moved the field toward systematic studies using sources with variable wavelengths [19, 109, 118–120]. For most HHG experiments, peak intensity and pulse duration are much easier variables to control and, because of the dependence of the Stark-shift on intensity, one should expect that intensity is an equally valid parameter to use as a probe in identifying REHHG. However, comparing harmonic yields at different driving intensities can be complicated [70, 121–124], with any emerging structures related to resonant enhancement often being masked by the rapid increase in harmonic yield with increased driving intensity [84, 106, 109, 121].

In this chapter, we explore a different technique for the identification and study of REHHG that is more accessible to use with varying peak intensity. Rather than requiring REHHG to occur at the peak of the laser pulse, we study the temporal and spectral signatures of REHHG occurring in the leading or trailing edges (the wings) of the pulse. In the time domain we identify a distinct signature of the resonant enhancement of a particular harmonic, that shifts with the time at which the resonance occurs [67, 84]. In the spectral domain, we identify the corresponding signature in the form of enhanced parts of that harmonic's spectral profile. We discuss how the spectral signatures, which are easily accessible in experiments, can be interpreted in terms of the two kinds of dynamics involved in REHHG: the timing of the resonance during the pulse that initiates the harmonic generation process, and the subsequent semi-classical electron dynamics that leads to emission of the harmonic light.

## 4.1 Introduction

Recall, from the previous chapter, that the resonant condition we expect to satisfy for REHHG to occur is given by [84, 107–109]:

$$|\Delta| + U_p = n\hbar\omega, \tag{4.1}$$

where we have generalized the condition away from helium, so that now $|\Delta|$ is the difference between an atomic ground state and any of the dipole-allowed excited states of the atom [125, 126]. Previously we treated this equation as if the intensity dependence of $U_p$ was fixed to the peak intensity of the driving laser pulse. This allowed us to consider Stark-shifted, multiphoton resonances that occurred only at the peak of the driving laser pulse. However, in actuality, $U_p$ is a time dependent value, varying during the laser pulse with the time-dependent intensity envelope [127, 128]. This means that Eq. (4.1) might be satisfied at any time during the pulse, not just at the peak. In this work, we extend our study of REHHG away from the peak of the pulse and instead look towards REHHG occurring in the wings of the pulse, studying how we can use the resulting signature to gain information about electron dynamics.

We illustrate more precisely how to think about these resonances occurring in the wings of a pulse in Fig. 4.1. Here we show the time-dependent intensity envelope of laser pulses in the form of Eq. (3.1) [104], explicitly given as

$$I(t) = I_0 \cos^4(\frac{c_2 t}{\tau}), \tag{4.2}$$

where $I_0$ is the peak intensity, and $\tau$ is the FWHM duration of the pulse. Note that in the fixed wavelength case, for a given $|\Delta|$ and $n$, there is exactly one resonant intensity that satisfies Eq. (4.1). In Fig. 4.1, we illustrate a resonant intensity, $I_r$, with the dashed line and show a pulse with $I_0 = I_r$, $\tau = \tau_0$ with the black curve, the case that we studied in the previous chapter. With the green curve, we illustrate

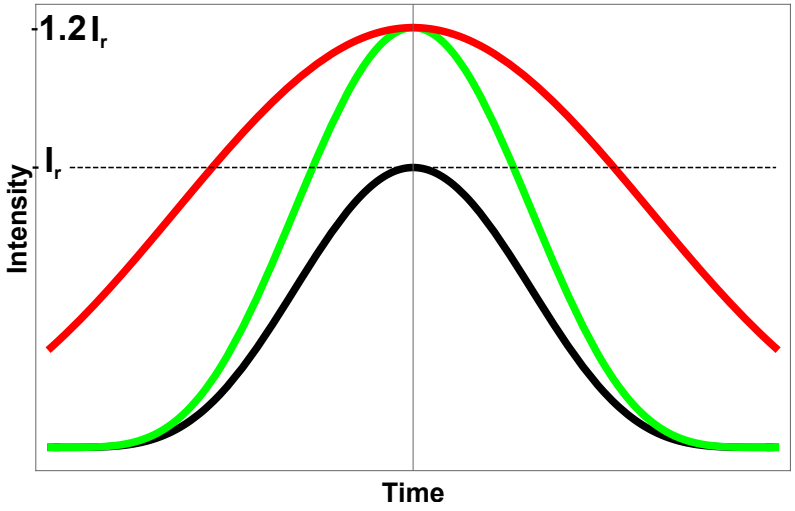


Figure 4.1: Three different laser intensity envelopes and a resonant intensity (dashed line). We have chosen the intensity envelopes so that one is resonant at the peak of the pulse (black), one has the same duration as the resonant pulse, but with a larger peak intensity (green), and one has a larger peak intensity and a longer pulse duration than the resonant pulse (red). We see that both the red and green curve cross the resonant intensity twice, once on the rise of the pulse and once on the fall.

a pulse with $I_0 = 1.2I_r$, $\tau = \tau_0$, while the red curve represents a pulse such that $I_0 = 1.2I_r$, $\tau = 2\tau_0$. In both the red and green case, the effect of having a peak intensity larger than $I_r$ is that the pulse crosses the resonant intensity twice, once on the rising edge and once on the falling edge. Because of the form that we have chosen for the pulses, these crossings occur symmetrically about $t = 0$.

When the resonant condition of Eq. (4.1) is satisfied at a particular time, we expect a temporal signature in the form of an enhancement of the harmonic yield at this time. In this chapter we identify these resonant enhancement signatures in the temporal and spectral domain by observing how the signatures shift as we vary when, during the driving pulse, the resonance occurs. This resonance time can be controlled by varying the peak intensity or the duration of a pulse. For example, with the green curve in Fig. 4.1, we could move the resonance time further away from $t = 0$ by increasing the peak intensity more, or by increasing the pulse duration, demonstrated by the red curve.

To better illustrate these signatures and how changing the time of the resonances influences the temporal and spectral profile of a resonantly enhanced harmonic, in Fig. 4.2 we look at the intensity-dependent time profiles and corresponding spectra of H11, calculated in an argon atom for an 800 nm, $\tau = 10$ O.C. pulse. We have chosen an intensity range around 26.5 TW/cm$^2$, an intensity for which we have observed H11 to be directly resonantly enhanced by an 11-photon resonance between the $3p$ ground state and the $7d$ state of argon ($|\Delta| = 15.44$ eV). In (a), we see that the temporal profile of H11 appears as a single peak for intensities below the resonant intensity, and branches into two distinct peaks for intensities larger than the resonant

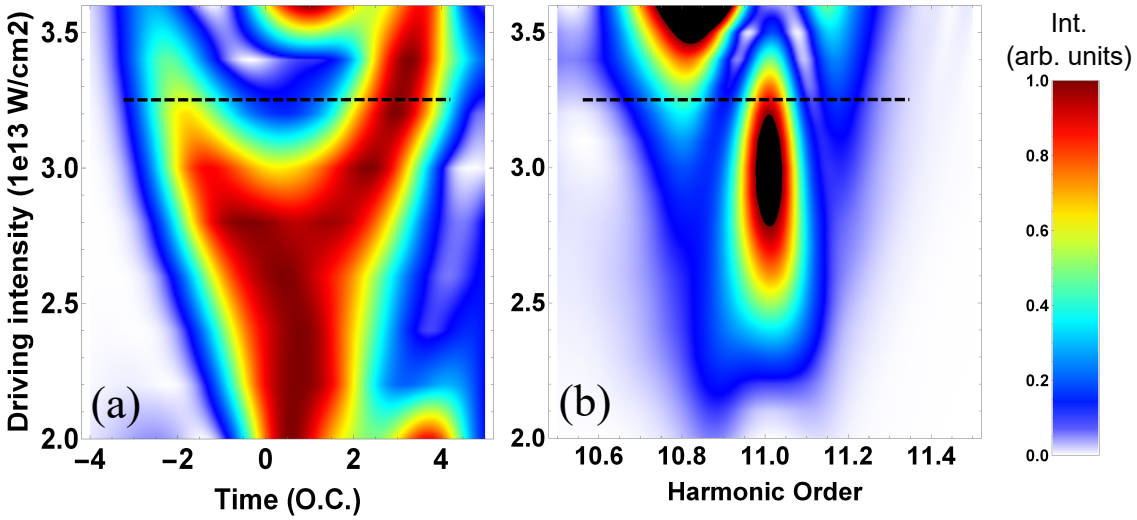


Figure 4.2: (a) Time profile of H11 in argon as a function of intensity for a $\tau = 10$ O.C., 800 nm pulse. Each intensity profile has been normalized to a maximum of 1. (b) Corresponding frequency profile, however, each spectrum has not been renormalized. The dashed lines in (a) and (b) correspond to the $\tau = 10$ O.C. lineouts in Fig. 4.3 (a) and (b), respectively. Note that black in a plot represents saturated maxima in the profile.

intensity. This branching occurs when there are two resonant interactions during the pulse and these two peaks serve as a temporal signature of the interactions. At the intensities for which the temporal peak begins to split in (a), we observe the appearance of two new spectral features in (b), one higher than the central harmonic frequency (H11) and one lower. These spectral features shift further away from the central harmonic frequency with increasing intensity. The appearance of these new spectral features serves as the spectral signature of resonant enhancement occurring in the wings. In section 3, we will discuss that the spectral feature above (below) the central frequency are due to resonantly enhanced contributions from the long trajectory on the rising (falling) edge of the pulse.

We can highlight interesting features of these signatures by looking at how they depend on other pulse parameters that also change the resonant time, such as pulse duration. In Fig. 4.3, we show this for a pulse with peak intensity of 32.5 TW/cm$^2$, which we highlight with the dashed lines in Fig. 4.2 (a) and (b). Here we see that with increased pulse duration, the temporal features move further apart in time, as we would expect from looking at Fig. 4.1. However, we see that the temporal signatures shift very differently with increased pulse duration than with increased intensity. Similarly, we observe that the spectral signatures actually shift much closer to the central harmonic frequency with increased pulse duration, unlike the dependence we observed with increased intensity. This difference in the spectral signature dependence must be related to the different temporal signature dependence, but the relationship between the two is not obvious.

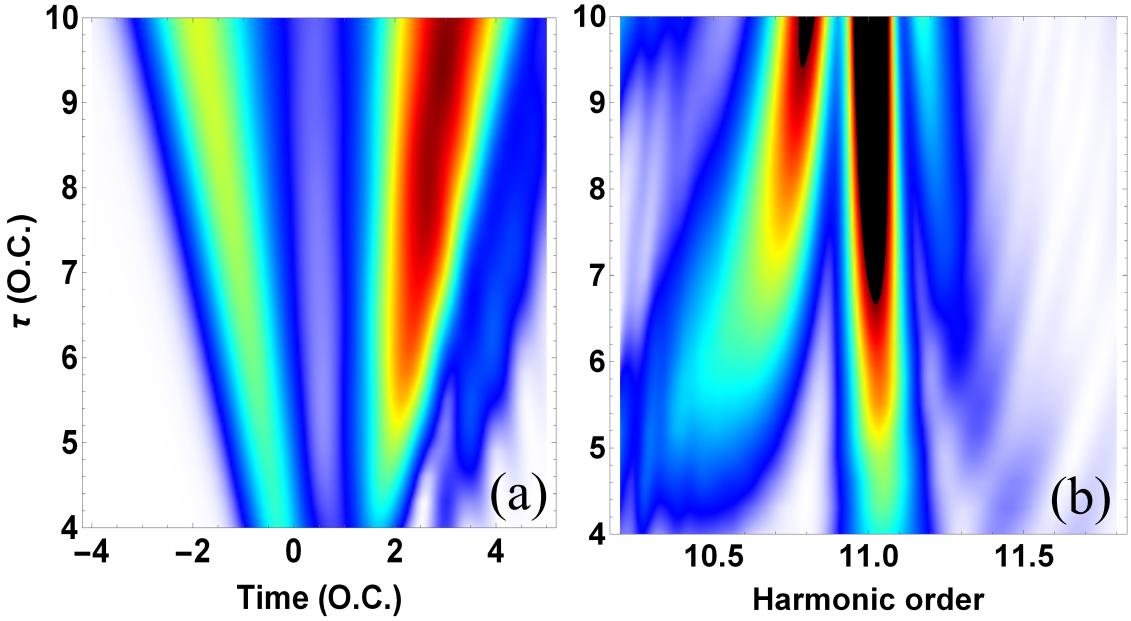


Figure 4.3: (a) Time profile of H11 in argon as a function of pulse duration for a $I_0 = 32.5$ TW/cm$^2$ pulse. Each pulse duration profile has been normalized to a maximum of 1. (b) Corresponding frequency profile, however, each spectrum has not been renormalized.

Lastly, taken together, Fig. 4.2 and Fig. 4.3 highlight interesting asymmetries in the signatures. The temporal signature appears asymmetrical about $t = 0$, despite the resonant intensities being symmetric. Spectrally, the high energy signature and the low energy signature do not mirror each other, and appear very different. In the following two sections, we will explore these asymmetries, as well as the other interesting dependencies discussed in this section, as we go into more depth discussing these signatures and applying them to the study of REHHG. We will illustrate how to best understand these signatures, and discuss the role of electron dynamics to their exact form.

## 4.2 Temporal signatures

In this section we are going to focus on the temporal signature of resonant enhancement in the wings of a pulse. We expect this signature to be tied to the time that a resonant intensity occurs as we vary the pulse parameters. This means that in order to understand how the temporal signature shifts, in time, as we vary the peak intensity or pulse duration, we must understand how a constant intensity evolves as we change $I_0$ and $\tau$. Assuming that we have a resonant intensity, $I_r < I_0$, then we can describe the time that we expect this resonant intensity to occur by solving the following equation for $t^r_\pm$, the time of the resonant intensity on the rising ($t^r_-$) and falling ($t^r_+$) edge of the pulse:

$$I_r = I_0 \cos^4\left(\frac{c_2 t^r_\pm}{\tau}\right). \tag{4.3}$$

Solving this equation yields,

$$t^r_\pm = \pm\frac{\tau}{c_2} \arccos\left(\sqrt[4]{\frac{I_r}{I_0}}\right). \tag{4.4}$$

This defines a curve of constant intensity in $(t, I_0)$ and $(t, \tau)$ parameter space, which we demonstrate in Fig. 4.4 (a) and (b), respectively, with solid blue (red) lines representing the intensity occurring on the rising (falling) edge. Observe that these curves of constant intensity behave very differently, depending on whether we vary $I_0$ (arccos-like) or $\tau$ (linear). Already we can recognize the dependency of these curves as being essentially the same that we previously observed, however, this gives us curves that are explicitly symmetric about $t = 0$, and we have observed that our temporal signatures are not symmetrical. In order to gain this asymmetry, we have to more carefully approach the expected temporal signature of REHHG, including the interaction of the field and the electron, as we do below.

Recall, from the previous chapter, that the major role of the resonance in the REHHG process is to help in the ionization of long and short electron trajectories related to the enhanced harmonics [84]. In that way, we expect the time of the resonant intensity to act as an ionization time. These trajectories, after being launched,

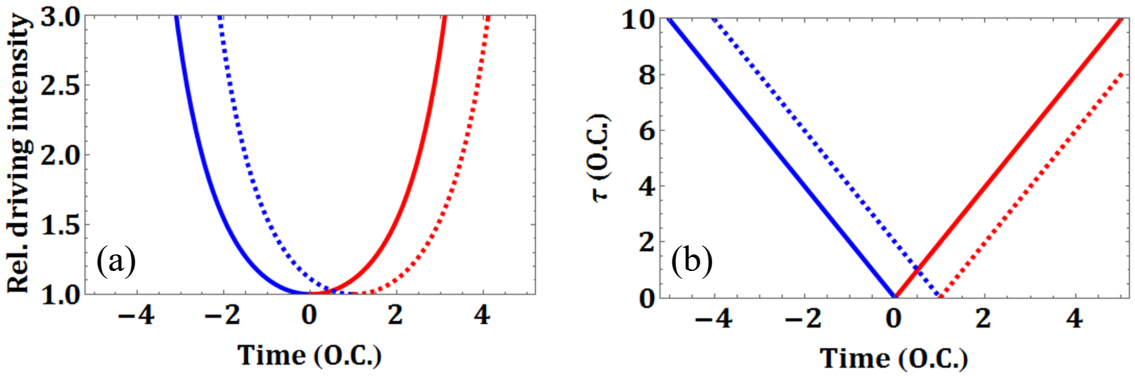


Figure 4.4: (a) The solid lines illustrate how a constant intensity in a pulse evolves with increased peak intensity relative to the resonant intensity, on the rising edge of the pulse (blue) and the falling edge (red) for a $\tau = 5$ O.C. pulse. The dashed lines show the solid lines shifted forward by 1 O.C. (b) The same thing as in (a), except as a function of pulse duration for a pulse that has a peak intensity twice the resonant intensity.

then take time to return to the core, recombine, and give us the related burst of light in the temporal profile of our harmonic. Depending on the primary trajectories launched, this return time can be between .25 O.C. and 1.25 O.C. [40,52,57,116,129]. We illustrate the expected curves of recombination for a trajectory taking 1 O.C. after ionization (at the resonant intensity) in Fig. 4.4 (a) and (b) with the dashed blue (red) lines for the rising (falling) edge resonance. This delay between the time of resonant intensity and the time of recombination is what breaks the symmetry of our temporal signatures about $t = 0$. Note that this delay between the resonant intensity and the recombination can be used to infer the primary trajectories involved in the generation of the harmonics we consider.

With a better understanding of these temporal signatures, we can now apply them to our study of REHHG. In Fig. 4.5, we again look at the temporal profile of H11 in argon at 800 nm, as a function of peak intensity (a) and pulse duration (b). We have overlaid (a) and (b) with black solid curves representing a recombination time of .75 O.C. after the $7d$ resonant intensity of 26.5 TW/cm$^2$. In (a), we also overlay a dashed line representing a resonant intensity at 38.9 TW/cm$^2$ shifted by 1.1 O.C., related to an indirect enhancement of H11 due to a 9-photon, $4s$ resonance. In both (a) and (b), the agreement between the curves and the observed temporal profile is good. This suggests that the observed temporal splitting of H11 is indeed directly related to enhancement through resonances whose "initiating" intensity varies in time as we increase the peak intensity. We note that for the $4s$ resonance in particular, the enhancement structures in (a) are a little higher in intensity than the overlaid curves. This could be indicative of the $4s$ state shifting slightly less than ponderomotively, as has been previously observed [84].

In fact, note that even when the resonant intensity is well into the temporal wings of the pulse, the only emission signal that we really observe is the REHHG signal. This is counter intuitive, as we would expect to observe emission from HHG

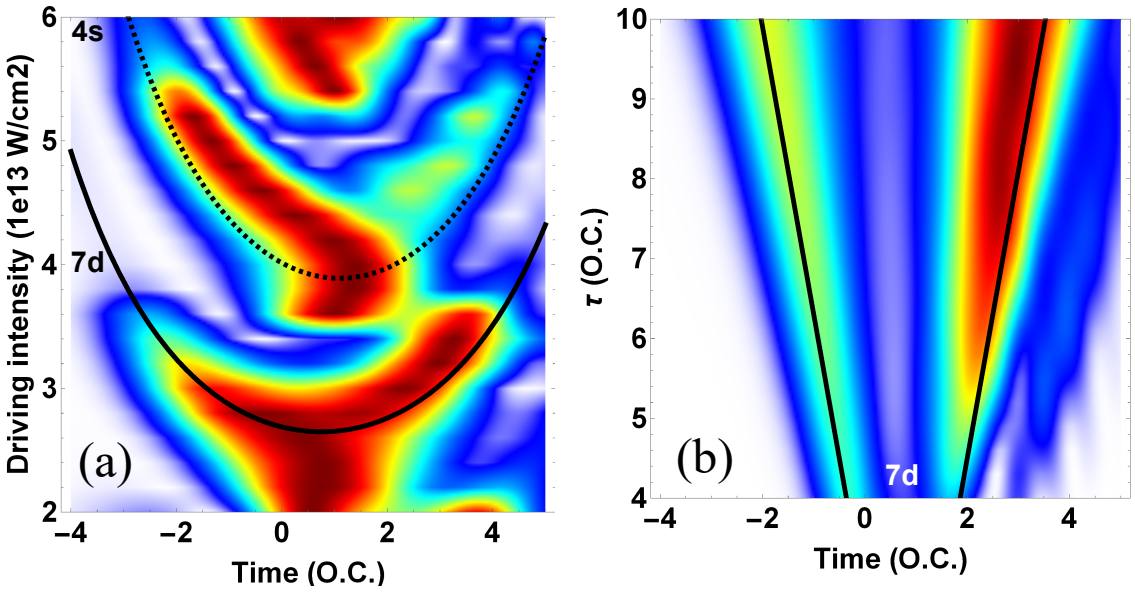


Figure 4.5: (a) Temporal profile of H11 as a function of intensity in argon for an 800 nm, $\tau = 10$ O.C. pulse. Overlaid with curves representing constant intensities of 26.5 TW/cm$^2$ (solid) and 38.9 TW/cm$^2$ (dashed) shifted in time by .75 O.C., and 1.1 O.C., respectively. (b) Temporal profile of H11 as a function of pulse duration for an 800 nm, $I_0 = 32.5$ TW/cm$^2$ pulse. Overlaid with curves representing a constant intensity of 26.5 TW/cm$^2$, shifted by .75 O.C.

processes driven by a higher intensity portion of the pulse. However, we do not see emission near the peak of the pulse, except for when we see another resonant process start to be driven. For example, the emission around $t = 0$ at the highest intensities of Fig. 4.5 (a) actually corresponds to the $3d$ state coming into resonance with H11. This serves to demonstrate that in these parameter ranges, the temporal dynamics of the near-threshold harmonics can be almost entirely dependent on these harmonic resonances

There are other interesting properties that we can infer from the temporal behavior of H11. The distinctive temporal shifts related to the different resonances in Fig. 4.5 (a) imply that the resonances initiate trajectory dynamics that is unique to each resonance. The peak emission time for the $7d$ resonance was .75 O.C. after the resonant intensity, which is a long trajectory return time related to harmonics close to the cutoff, whereas the $4s$ resonance led to a peak return time that was 1.1 O.C. after the resonant intensity, which is a characteristic of a long trajectory related to a low-order plateau harmonic [57, 116]. These are distinctively different trajectories, but the emission signal of each resonance is consistent in its unique return time. This indicates that these trajectories are very stable and depend only on being driven by a particular resonance.

We also see that there can be interesting differences between the emission on the rising and falling edge. The $7d$ resonant emission doesn't show much asymmetry between the rising and falling edge resonance, though it does consistently demonstrate

a stronger return for the later resonance. The $4s$ resonance, however, is asymmetric, with the early emission being unchanging with intensity, but the late emission showing a ripple-like structure. There is always a structure observed on the falling edge, but it is weak and changes strength rapidly. This asymmetry between the rising and falling edge is currently unexplained. It could be related to the fact that this is an indirect resonant enhancement. Asymmetries between resonant effects on the rising and falling edges of a pulse have been previously explained using the asymmetry between ionization before the peak of a pulse (low) and after the peak (high) [128]. But this physical explanation does not seem to fit here, as there are intensities where the rising edge emission returns after the peak of the pulse, but does not show any effects similar to what the falling edge demonstrates.

While this chapter is not focused on studying the temporal signatures as we vary the wavelength parameter, it is interesting, in discussing the difference in the behavior on the rising and falling edge, to look at the $\lambda$ dependence. Note that as we increase $\lambda$, we expect the intensity necessary to drive a resonance to decrease. This means that increasing the wavelength will move a resonant intensity into the wings for a pulse with a fixed peak intensity and duration. We show the H11 temporal emission as a function of driving wavelength for an $I_0 = 40$ TW/cm$^2$, $\tau = 10$ O.C. pulse in Fig. 4.6. This parameter range is chosen to show the $4s$ resonance and we overlay the plot with the $\lambda$-dependent time of recombination, assuming the same 1.1 O.C. delay that we observed with intensity. Again we see good agreement between the structure and the curve, however, the structure is still slightly higher than the curve, reiterating that the state seems to shift slightly less than ponderomotively. Notice that the splitting structure in $\lambda$ looks almost exactly

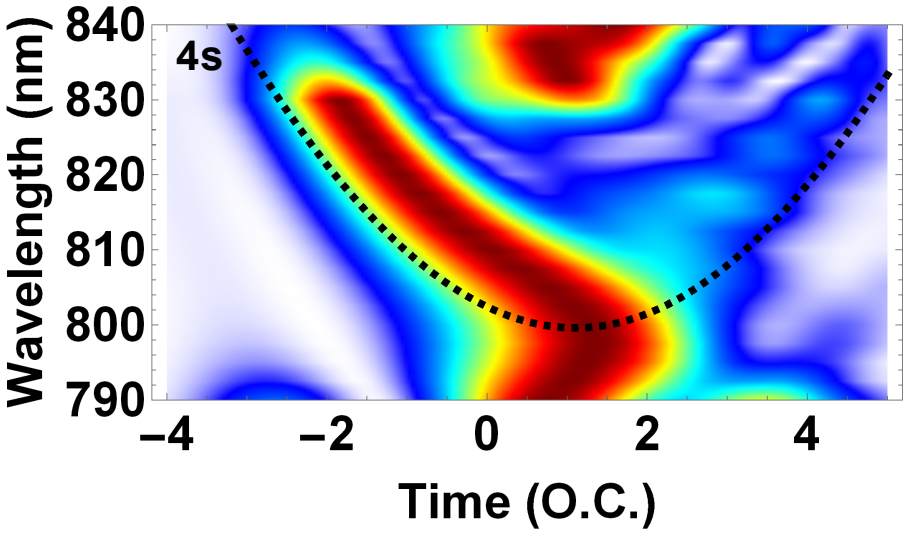


Figure 4.6: The temporal profile of H11 as a function of wavelength in argon for a $\tau = 10$ O.C. and $I_0 = 40$ TW/cm$^2$ pulse. We overlay the plot with curves of the $\lambda$-dependent intensities for an indirect enhancement of H11 by a 9-photon, $4s$ resonance (dashed), shifted by 1.1 O.C. Here the temporal profile at each driving wavelength have been normalized to a maximum value of 1.

as it looked in $I_0$, with the rising edge emission being well defined, but the falling edge emission showing a ripple-like structure. This is interesting because these processes in $\lambda$ and $I_0$ are occurring at very different parameters: different ponderomotive shifts, intensities and wavelengths. Yet we see the same emission signature on the rising and falling edges. This similarity seems to imply that the electron dynamics initiated in REHHG can be less dependent on the specific pulse parameters, and can depends more on the fact that a specific resonance was driven in a particular way, either with rising or falling intensity.

### 4.3 Spectral signatures

We now turn our attention to the spectral signatures. Previously, we have observed no distinct spectral signatures for harmonics enhanced at the peak of the field, *i.e.*, the resonantly enhanced H9 in the 440 nm case in Fig. 3.1 shows no distinctive spectral features, aside from being stronger than H9 at the other wavelengths. This is different for the case of REHHG in the wings of the pulse. For harmonic generation in the wings of a pulse, the harmonic frequency will be shifted away from the central frequency and will depend on the derivative of the intensity envelope at the time of recombination, as well as the trajectory taken to recombine [63,64,67–69,130]. From the intensity-dependent dipole phase discussed in Chapter 1, this instantaneous frequency of the $q$th order harmonic can be expressed as

$$\Omega_q(t) = q\omega + \alpha_q^{s,l}\frac{\partial I(t)}{\partial t}, \tag{4.5}$$

where $\alpha_q^{s,l}$ is the constant of proportionality for the intensity dependent phase coefficient of the short (s) and long (l) trajectories contributing to the $q$th harmonic, and $\omega$ is the frequency of the driving pulse. This instantaneous frequency shift for HHG emission in the wings of the pulse gives us our distinct spectral signature.

There are two interesting properties of the instantaneous frequency. First, note that this instantaneous frequency corresponds to different spectral shifts for the long and short trajectories since $\alpha_q^s \approx 0$ and $\alpha_q^s << \alpha_q^l$ for harmonics in the plateau [65, 131]. This introduces an interesting asymmetry between the spectral behavior of the two trajectories, because it means that when the primary harmonic emission is in the wings of the pulse, we expect the short trajectories to emit essentially unshifted from the harmonic frequency, whereas we expect the long trajectories to emit at frequencies well shifted from the harmonic frequency [68, 132]. This allows for a simple spectral separation of the two trajectory contributions, whereas typically the two trajectories spectrally overlap, complicating interpretations related to the trajectories [13,19,57,71,95,133]. The other interesting property of the instantaneous frequency is its asymmetric behavior with respect to HHG emission on the rising the falling edge of the pulse, since on the rising (falling) edge, the derivative of the intensity envelope is positive (negative). This means that we expect emission on the rising edge to be blueshifted (increased in energy) and emission on the falling

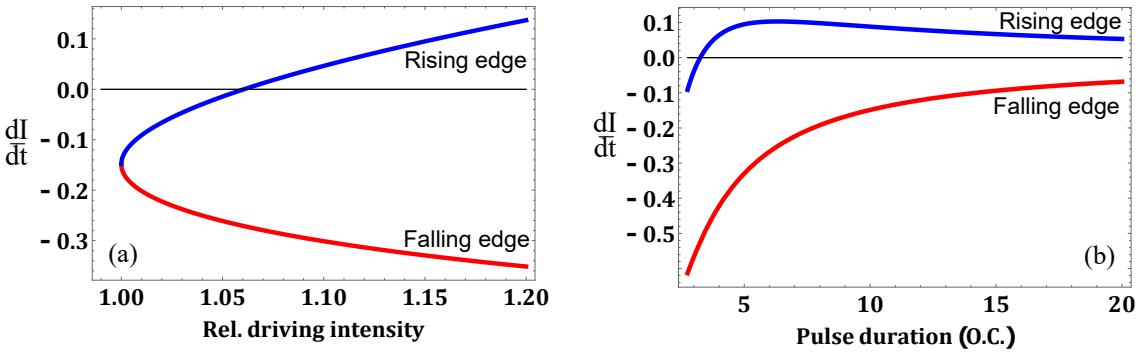


Figure 4.7: Variation of intensity profile derivative (Eq. (4.3)) with peak intensity and pulse duration when evaluated 1 O.C. after the resonant intensity. In (a) we show the intensity dependence for a $\tau = 5$ O.C. pulse and in (b) we show the pulse duration dependence for a peak intensity of $I_0 = 1.15I_r$, where $I_r$ is the resonant intensity. In both (a) and (b), the blue curves correspond to the return associated with the rising edge resonance and the red curves correspond to the return associated with the falling edge resonance.

edge to be redshifted (decreased in energy) [68]. This asymmetry allows us to easily spectrally distinguish between emission related to rising and falling edge resonances.

The specifics of the spectral signature are more complicated than the temporal signature, as the spectral signature depends on the derivative of the intensity envelope evaluated at some return time after the time of the resonant intensity. However, purely from the form of the derivative of the intensity envelope,

$$\frac{\partial I(t)}{\partial t} = \frac{4I_0 c_2 \cos^3(\frac{c_2 t}{\tau}) \sin(\frac{c_2 t}{\tau})}{\tau}, \tag{4.6}$$

we expect these spectral signatures to shift away from the central harmonic frequency at large $I_0$ and closer to the central harmonic frequency at large $\tau$. This is demonstrated in Fig. 4.7 (a) and (b), which shows the time derivative of a pulse evaluated 1 O.C. after a resonant intensity as a function of relative peak intensity to the resonant intensity (a) and pulse duration (b) with the rising (falling) edge resonance shown in blue (red).

Fig. 4.7 also serves to highlight complications introduced to the instantaneous frequency by evaluating it some time after the resonant intensity. Because of this delay, we can get unique behavior in this spectral signature when our pulse intensity is close to resonance or when our pulse is extremely short. In these situations, the resonant intensity can be closer to the peak of the pulse than the time required for long trajectory electrons to return, and the trajectories on the rising edge of the pulse can return on the falling edge of the pulse. This leads to redshifted spectral features that relate to rising edge resonances and is highlighted in Fig. 4.7 (a) and (b), when the blue curves have a negative value. Note that the recombination from the resonance on the falling edge of the pulse will always occur on the falling edge. This is due to the inherent time asymmetry between the rising and falling edge, with

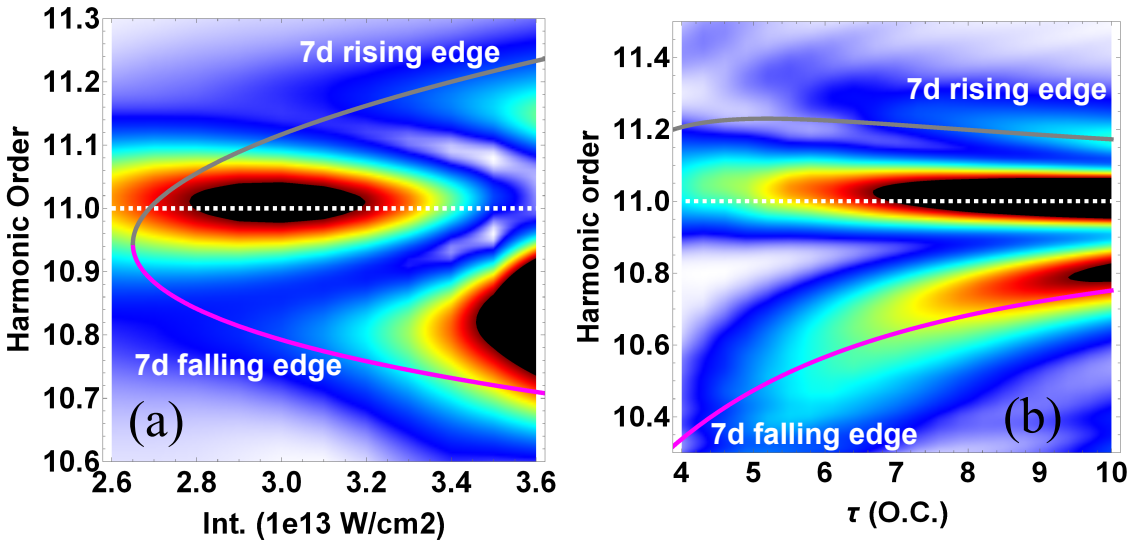


Figure 4.8: (a) and (b) show the spectra corresponding to Fig. 4.5 (a) and (b), respectively, though (a) has been chosen to look at the spectra around the $7d$ resonance only. The solid curves represent the instantaneous frequency expected from the $7d$ resonant enhancement on the rising and falling edge (shown in grey and purple, respectively). Note that $\alpha$ values have been chosen to fit the magnitude of the observed spectral features, and not directly calculated. Also note that here the spectra has not been renormalized, unlike the corresponding temporal profiles.

the rising edge emission always occurring closer to the peak of the pulse than the falling edge emission. When a situation arises where we have redshifted rising edge emission, the spectral signature will quickly correct itself with increased intensity or pulse duration, which is also demonstrated in Fig. 4.7 (a) and (b).

With a better understanding of the spectral signatures, we now turn our attention to applying them to study resonant enhancement. In Fig. 4.8 (a) and (b), we show the corresponding spectra of Fig. 4.5 (a) and (b), respectively, for intensities around the $7d$ resonance. We overlay the plots with the calculated instantaneous frequency from the temporal curves in Fig. 4.5 (a) and (b), where we have colored the blueshifted curves gray and the redshifted curves purple. Note that we have chosen an $\alpha$ value for Eq. (4.5) that fits the magnitude of the observed spectral shifts. This means that what should be considered here is not the magnitude of the curves, but rather the shape. While it is difficult to observe in Fig. 4.8, we find good agreement between the shape of the predicted curves and the resulting spectral signal. These agreement holds well except at small $\tau$, where the blueshifted feature becomes very hard to recognize. We can further confirm our explanation for the spectral signatures by observing that the redshifted feature is generally stronger than the blueshifted feature, corresponding to our temporal domain observation that the late $7d$ emission signal was stronger than the early.

These spectral signatures also contain a lot of information about the trajectory dynamics. In Fig. 4.8 (a), we see that with increasing intensity, the emission at the

central harmonic frequency (white dotted lines) decreases until there is no signal at all at 36 TW/cm$^2$. This implies that with increased intensity, there is actually less short trajectory emission. The short trajectory emission at the central frequency depends more weakly on $\tau$, as the unshifted emission in Fig. 4.8 (b) gains weakly in strength, but is essentially unchanged otherwise.

Conversely, the long trajectory depends much more sensitively to $\tau$, particularly depending on which edge the emission occurs on. We see that the rising edge long trajectory signature is weak and hard to recognize for short pulses, while the falling edge emission is much more consistent. This provides another asymmetry between the rising and falling edge emission signatures. In Fig. 4.8 (a), the long trajectory seems essentially unchanged with intensity for the $7d$ resonance and we observe a very strong long trajectory spectral signal from both the rising and falling edge of the pulse for all intensities above the resonance. This recognizable signal from the long trajectory is fairly consistent with the fact that we persistently observe emission at .75 O.C. after the resonant intensity on both the rising and falling edge, since that corresponds to a long trajectory return time [57, 116].

### 4.4 Application to recent experiments

Recent experiments looking at the intensity-dependent HHG spectra of argon discovered a spectral feature that redshifts as the intensity of a driving pulse is increased [67], atypical of normal HHG processes with increased intensity [68, 132]. Fig. 4.9 shows experimental spectra measured using 800 nm, 2.75 O.C. FWHM driving pulses with varying peak intensity. In this figure we highlight the redshifting feature and H13 by overlaying them with a dotted and solid line, respectively. Immediately, we can see that this redshifted feature looks like a spectral signature of REHHG in the falling edge of a pulse. Looking at the entire spectrum, we can get another hint at this, because of the observation of narrow spectral features between 14 and 16 eV, occurring at the resonant energies of argon due to population being left in excited states. As we saw in the last chapter, this is a calling card of REHHG.

Follow-up experiments were performed that added more evidence for this redshifting feature to be falling edge REHHG emission: By looking at the spatial profile in the far field, as a function of intensity, the experimentalists were able to show that this redshifted spectral feature was very divergent and thus had a large atomic dipole phase, similar to that of a long trajectory [65, 131]. Hence this emission looks like a long trajectory spectral contribution. By performing complicated attosecond lighthouse experiments [134], the experimentalists also demonstrated that this emission temporally occurred far into the wings of the pulse. They showed the redshifted emission occurring 2 O.C. after the peak of the pulse at one particular intensity [67]. All of these experimental observations conform to properties that we would expect with a redshifted spectral signature of REHHG in the falling edge of a pulse.

For this parameter range, we expect that there are no direct Stark-shifted resonances with H13, meaning that this process needs to be related to an indirect

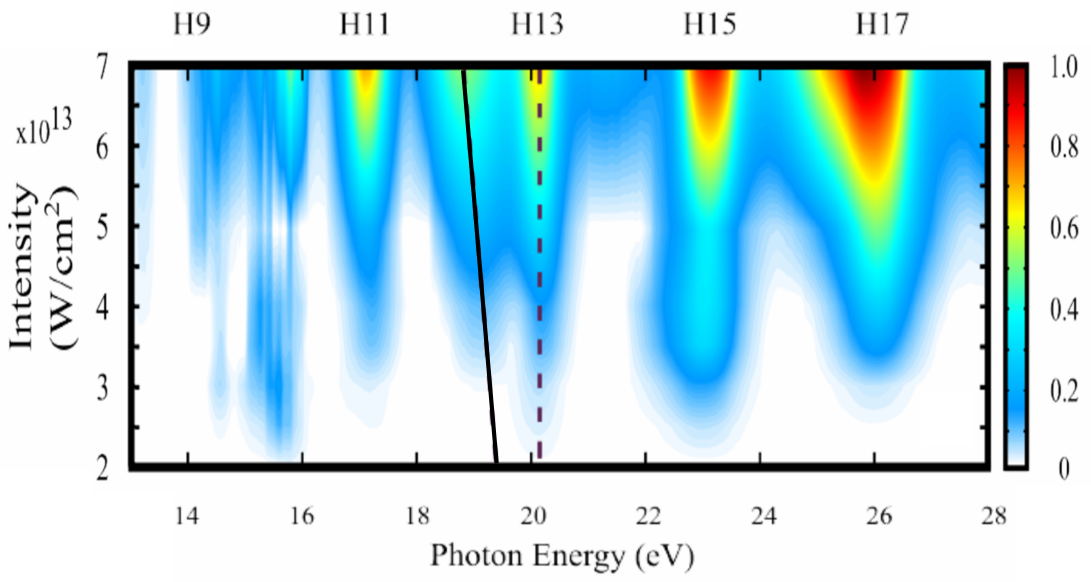


Figure 4.9: Experimentally measured HHG spectra in argon as a function of driving pulse intensity for an 800 nm, 7 fs FWHM driving laser pulse. The intensity dependent spectrum show the expected emission occuring at the harmonic energies, such as H13 (dotted line), as well as narrow spectral features at the resonant energies (spectral features between 14 ev and 16 eV) and a new intensity dependent, red-shifting spectral feature (eHHG) shown with the solid line. This new intensity dependent, red-shifting spectral feature is directly related to emission occuring several fs after the peak of the pulse. Adapted from [67] with permission.

resonant enhancement of H13. However, using Eq. (4.1) for argon in this intensity range, we find that this falling edge emission is likely due to a $3d$ resonance with H11. At 800 nm, we expect this resonance to be driven at 50 TW/cm$^2$. Note that the lack of experimental observation of any signal on H11 is not entirely disconcerting, as we observed that the spectral signature of H11 for pulses less than $\approx$ 4.5 O.C. was extremely weak and ill-defined for both the rising and falling edge. The observation of a long trajectory spectral signature for an indirect resonant enhancement to H13 at such a short pulse might indicate that indirect resonances leading to higher return energies, corresponding to long trajectories that spend less time in the continuum [57], can be less sensitive to pulse duration. Again, using Fig. 4.8 (b) as a guide, it is also understandable that the experiment might not observe an H13 emission signature from the rising edge resonance, as we saw that for H11, the rising edge emission was much more sensitive to pulse duration than the falling edge.

We show our calculated H13 temporal profile and HHG spectra around H13 as a function of intensity in Fig. 4.10. In the time domain, we find a much more complicated harmonic profile than we saw in the previous section. There is no well defined rising edge emission signal, however, there does seem to be a well defined falling edge emission signal. We overlay Fig. 4.10 (a) with the curve of recombination from the 11 photon, $3d$ resonance, assuming a .25 O.C. delay after the

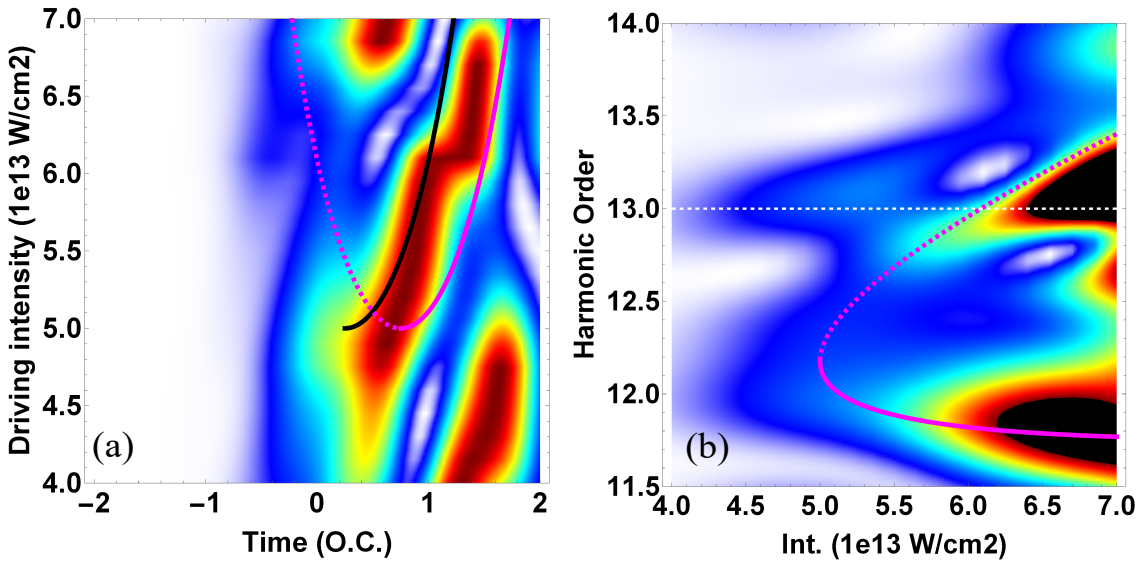


Figure 4.10: (a) The temporal profile of H13 in argon as a function of intensity for a $\tau = 2.75$ O.C. pulse. Overlaid with curves of constant intensity for a 50 TW/cm$^2$ resonance shifted by .25 O.C. (black) for the falling edge only, and .75 O.C. for the rising (purple, dashed) and the falling (purple, solid) edge. (b) The corresponding spectral profile of H13 as a function of intensity. Overlaid with curves corresponding to the instantaneous frequency evaluated with the corresponding purple curve of (a). The value of $\alpha$ has been chosen to fit the spectral magnitude of the shift.

resonant intensity for the falling edge (black). This curve agrees very well with the primary emission signal observed and, because a .25 O.C. return time corresponds to a short trajectory, implies that we should spectrally observe a lot of emission at the central frequency. We also show a long trajectory recombination curve for the rising (purple, dashed) and falling (purple, solid) edge resonance, shifted .75 O.C. after the resonant intensity. Here the falling edge purple curve agrees with a weaker portion of the emission, while the rising edge purple curve seems to overlap temporal emission, but has no temporal features that track along with it.

In the frequency domain, shown in Fig. 4.10 (b), we have overlaid the calculated instantaneous frequencies generated from the corresponding (dashed or solid) purple curves in the temporal domain. We immediately see that the redshifted feature (solid) agrees well with our calculated curve, and with the experimental redshifted feature from Fig 4.9. Spectrally, we also observe a blueshifted emission feature that agrees with the rising edge resonant curve, even though the temporal structure was not as well defined as for the falling edge emission. However, this spectral signature was not measured in the experiment, which hints that because its temporally less well defined, it might be more sensitive to macroscopic phase matching that would play a role in the actual experiment. Also note there is always a strong emission signal at the central harmonic frequency (white dashed line). This corresponds well to our observation that the black curve in (a) agrees very well with the primary emission feature.

Note that fitting our expected signatures here is more complicated than in the last section, which is likely a combination of two factors: First, the pulses considered here are extremely short. In the previous section, we saw that this led to issues in observing clear spectral signatures of REHHG. Second, because of the experimental observation of this effect happening on H13, we are forced to consider indirect resonant enhancements and to try to infer dynamics related to them. Indirect resonant enhancements are currently not well understood. The indirect resonance that we considered in section 2 was fairly well behaved, with respect to our calculated signatures, though we did find an interesting asymmetry between the rising and falling edge signatures in that case. Because it is not a direct resonant process, the dynamics leading to this harmonic could be very complicated. This might explain why the temporal profile of the indirectly enhanced harmonics that we have observed have been more complicated than for the directly enhanced harmonic. With both of these complications, however, we still generally find a very good fit between the experimental observations of this redshifted feature and the indirect resonant enhancement of H13 due to a Stark-shifted, 11 photon resonance with the $3d$ state of argon in the falling edge of the pulse.

### 4.5 Summary

In this chapter we have seen that the technique of looking at temporal and spectral signatures imposed by shifting REHHG resonances into the wings of a pulse has many uses. It can allow for identification of REHHG in variables that are typically complicated to work with for resonant enhancement, such as peak pulse intensity. It can also allow for the study of resonant enhancement in variables that have never been associated with the topic, such as pulse duration. We have seen that one strength of this technique is that it allows for the study of trajectory dynamics in REHHG in the spectral domain, automatically separating the long and short trajectory contributions in the spectrum. It also allows us to separate long trajectory dynamics on the rising and falling edge of the pulse. The technique is not as strong for short trajectories, as we can not easily relate them to falling or rising edge emission, however, this technique could potentially be used to gain insight into the complicated trajectory dynamics of REHHG. This could potentially allow for better tailoring of attosecond pulse trains and single attosecond pulses from resonantly enhanced harmonics around threshold [46, 47, 52, 135]. Further, this technique was applied directly to the interpretation of recent experimental observations and found to explain them in a very simple manner.

# Part II

# Resonant interactions in transient absorption in a macroscopic medium

# Chapter 5
# Transient absorption and macroscopic numerical methods.

We now transition to the study of resonant interactions in transient absorption in a macroscopic medium. In Chapters 6 and 7, we show that a resonant interaction with a medium can introduce many different effects that can not be accounted for at the single atom level alone. We also transition from thinking about the generation of HHG to an application of the HHG light source in transient absorption. We must also construct the numerical framework for modeling laser beams propagating through and interacting with a macroscopic gas medium, namely the coupled solutions of the TDSE and the Maxwell wave equation. This chapter sets out to accomplish both of these things.

The chapter is structured as follows: Section 1 gives an introduction to transient absorption, focusing primarily on attosecond transient absorption, which makes use of attosecond XUV pulses to study XUV-initiated electron dynamics in the presence of a moderately strong IR field. Section 2 demonstrates how to calculate the single atom response function and explains typical features of the transient absorption spectrum. Section 3 discusses the numerical framework for the macroscopic calculations.

## 5.1 Introduction to transient absorption

In time domain studies of dynamic processes, it is important to probe the process on the characteristic time scale that it occurs. This requirement has driven development of shorter and shorter laser pulse durations in order to study faster and faster atomic and electronic dynamics. With the creation of picosecond (1 ps $= 10^{-12}$ second) laser pulses around 1970, scientists were able to study the rotation of large molecules [136–138]. Pushing the limits to femtosecond (1 fs $= 10^{-15}$ second) laser pulses in the 1980's opened up the world of rapid molecular vibrations for study [139–142]. The advent of laser pulses with attosecond (1 as $= 10^{-18}$ second) duration, near the beginning of the 21st century, gave the world access to the fastest dynamics outside of the atomic nucleus, those of the electron [44, 45].

These XUV attosecond laser pulses have been used many different ways to probe and study electronic dynamics [26, 28, 47, 74–76]. One promising application is attosecond transient absorption (ATA), a technique in which one measures the frequency-resolved, time integrated absorption spectrum by a medium interacting with both an attosecond pump pulse and a time-delayed moderately strong IR

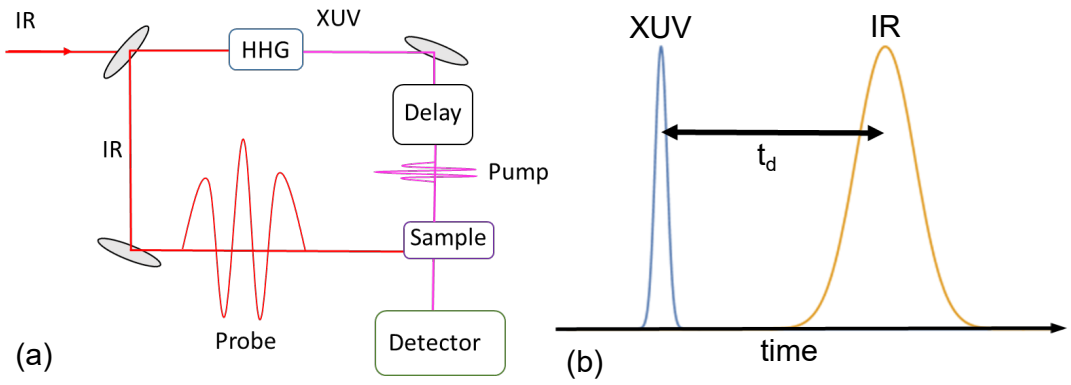


Figure 5.1: (a) Typical setup for a transient absorption experiment. A strong IR pulse is split into two separate IR pulses. One IR pulse is used as the probe pulse, while the other IR pulse goes through an HHG process to generate the XUV pump pulse. The absorption of the XUV pump pulse is then measured as a function of delay with respect to the IR probe pulse. (b) Illustration of the time profile for the XUV pump pulse and the IR probe pulse with a relative delay $t_d$ between the pulses. Note that the intensities in (b) are not shown to scale.

probe pulse [48, 143–146]. The IR pulse is typically in the range of a few times $10^{12}$ W/cm$^2$, which is strong enough to couple excited states to other nearby states, but not to excite the electron out of the ground state. The attosecond pump pulse typically has photon energies in the range of $20 - 100$ eV and can excite the atoms in the medium, while the IR probe pulse has photon energies in the range of 1.5 eV and cannot excite or ionize the atoms from the ground state, but can induce multiphoton absorption or ionization processes after the atoms have been excited [48]. By studying the change in the XUV absorption as a function of delay between the two pulses, one can learn about the time-dependent dynamics that occur during the interaction between the fields and the electron. ATA has been implemented and studied in dilute noble gases [77–81, 143, 144, 146–151], molecular gases [82, 83, 145, 152], and even thin-films [153, 154]. These ATA studies have provided key insight into many basic physical processes, such as light-induced virtual states [79, 80], molecular dissociation [145, 152], line-shape modifications in the absorption spectra [77, 78, 149, 150], autoionization from doubly excited states [83, 147], the motion of valence electrons [143], and many other physical phenomena. For the work in this thesis, we constrain our focus to ATA in rare/noble gases.

We illustrate the usual set-up for an ATA experiment in Fig. 5.1(a). A strong IR pulse is split into two separate IR pulses. One pulse is used as the probe pulse, while the other is used in an HHG cell to generate the attosecond XUV pump pulse. Generating the probe and pump pulse from the same initial IR pulse results in the pump and probe pulse being automatically synchronized, allowing experimentalists to gain the high delay resolution necessary to study ultrafast electronic dynamics in ATA. The two pulses, with a chosen delay between them, then pass through the sample gas after which the XUV spectrum is measured on a detector. In Fig. 5.1(b),

we illustrate the time profile of the two pulses with a relative delay between them of $t_d$.

Absent the IR, the effect of the XUV field is to excite the electron to dipole-allowed excited states of the atom (bright states). This gives rise to an excited state energy contribution to the dipole, $d(t)$, that decays over some finite lifetime, as we observed in Chapters 2 and 3. In a macroscopic medium, this dipole contribution generates an electric field that is exactly out of phase with the driving field and therefore leads to absorption when added to the driving (propagating) electric field [13]. The time-dependence of this newly generated electric field (which decays with the lifetime of the time-dependent dipole moment) gives rise to the characteristic Lorentzian shape in the absorption spectrum around these excited energy levels, which we demonstrate in Fig. 5.2 with the black curve [150]. When the IR field is present, either during or after the XUV excitation, it couples the XUV-excited states to nearby states. This leads to a Stark-shift of the bright state energy and thereby a phase shift of the time dependent dipole moment. The amount of the phase shift and the time that it is imposed onto the decaying dipole moment can alter the absorption line shape. When this phase shift is $\pi/2$ and imposed when the states are first excited, the absorption line shape changes and becomes dispersive (Fano-like) instead of Lorentzian, which we illustrate in Fig. 5.2 with the red curve. This has been explored in detail in [149, 150]. Understanding how the XUV absorption line shape changes at different delays between the XUV and IR fields provides insight into the dynamics of the atomic system while it is interacting with these two fields. We explore this in more detail in the following section after calculating the single atom transient absorption spectrum.

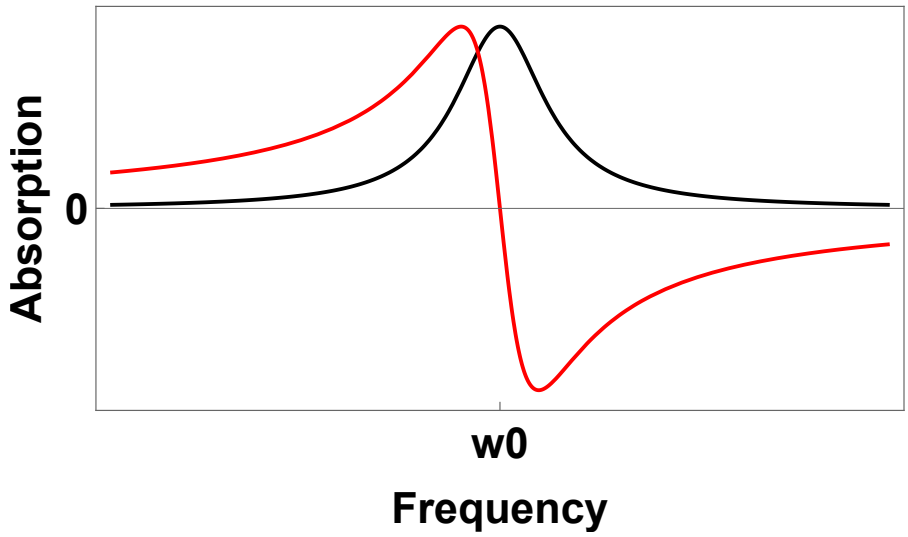


Figure 5.2: Demonstration of Lorentzian (black) and dispersive (red) absorption line shapes. Here $\omega_0$ represents the excited state energy that we consider.

## 5.2 Calculation of the single atom transient absorption spectrum

At the single atom level, we can calculate the interaction of an electron with a two-color (IR + XUV) field, using the numerical techniques of Chapter 2. We first describe the two-color field as the sum of a linearly polarized IR field and a linearly polarized XUV field, so that

$$\mathcal{E}(t) = \mathcal{E}_{IR}(t) + \mathcal{E}_{XUV}(t). \tag{5.1}$$

These fields take the same form that we used for the driving fields in Part I, such that

$$\mathcal{E}_{IR}(t) = \mathcal{E}_0 \cos^2(\frac{c_2 t}{\tau}) \cos(2\pi t), \tag{5.2}$$

$$\mathcal{E}_{XUV}(t) = \mathcal{E}_1 \cos^2(\frac{c_2(t-t_d)}{\tau_1})^2 \cos(2\pi X(t-t_d)), \tag{5.3}$$

where $\mathcal{E}_0$ and $\mathcal{E}_1$ are the peak IR and XUV field strengths, respectively, $t$ is in units of O.C. of the IR field, $c_2 = 2\arccos(\frac{1}{2}^{\frac{1}{4}})$, $\tau$ and $\tau_1$ are the FWHM duration of the IR and XUV field, respectively, $X$ is the photon energy of the XUV relative to the photon energy of the IR, and $t_d$ is the delay between the two fields. Note we assume the IR field is zero for $|t| > \frac{\tau\pi}{2c_2}$ and that the XUV field is zero for $t > (\frac{\tau_1\pi}{2c_2} + t_d)$ and $t < (-\frac{\tau_1\pi}{2c_2} + t_d)$. With the fields modeled, we can now solve the TDSE and calculate the dipole spectrum, $\widetilde{\mathcal{D}}(\omega)$. To describe the single atom absorption probability at a given frequency, we calculate a response function derived from requiring conservation of energy between the atom and the field [48, 79, 149, 155], given as

$$\widetilde{S}(\omega) = 2\,\mathrm{Im}\left[\widetilde{\mathcal{D}}(\omega)\widetilde{\mathcal{E}}^*(\omega)\right], \tag{5.4}$$

where $\widetilde{\mathcal{E}}(\omega)$ is the Fourier transform of the two-color driving field. $\widetilde{S}(\omega)$ represents the absorption probability per unit frequency at a given frequency, so that $\omega\widetilde{S}(\omega)$ represents the energy gained or lost by the atom per unit frequency at $\omega$ [149, 156]. If $\omega\widetilde{S}(\omega)$ is positive, the atoms absorb XUV light, and if $\omega\widetilde{S}(\omega)$ is negative, then the atoms emit XUV light at that frequency.

We show the delay dependent absorption spectrum, the spectrogram $\widetilde{S}(\omega, t_d)$ in Fig. 5.3 for a helium atom interacting with an 800 nm, 4 O.C. FWHM IR pulse with a peak intensity of 3 TW/cm$^2$ and a 330 as (1/8 O.C.) XUV pulse with energy centered at 25 eV ($X = 16.13$). Fig. 5.3 illustrates many of the characteristic features found in a ATA spectra and demonstrates that different delays between the XUV pulse and the IR pulse can greatly alter how the XUV light is absorbed [48]. Our delay convention is such that large positive (negative) delays correspond to the IR pulse arriving completely before (after) the XUV pulse. For large positive delays, the IR field is not strong enough to excite the atom out of the ground state, so that when the XUV field arrives it interacts with the unperturbed ground state of the atom and is only absorbed at the bright state energies, with no dependence on the relative delay with the IR pulse. This gives rise to Lorentzian-like absorption line shapes at the energies corresponding to bright states. For large negative delays, the

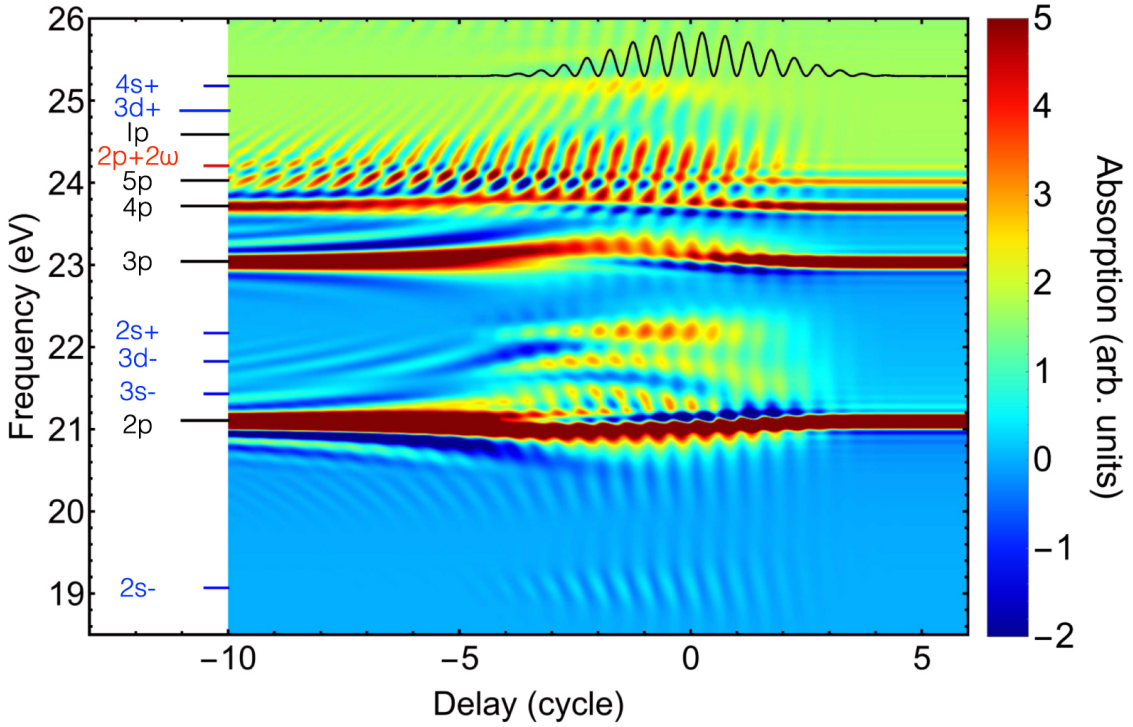


Figure 5.3: Single atom absorption spectrogram, calculated in helium using a 330 as XUV pulse with photon energy centered at 25 eV and an IR pulse with a wavelength of 800 nm and a peak intensity of $3\text{x}10^{12}$ W/cm$^{-2}$. On the left side are labels showing selected singly excited states plus or minus some number of IR photons. Note that negative delay refers to the XUV pulse arriving before the IR pulse. The black curve at the top of the figure represents the time profile of the IR pulse. Reprinted from [48] with permission.

XUV pulse first excites bright states in the atom and the IR pulse then couples these populated bright states to nearby states. This coupling alters the absorption line shape from Lorentzian and gives rise to hyperbolic sidebands off of the absorption features due to perturbed free-induction decay. In this delay regime, as well as the regime where the XUV and IR pulses overlap, we get delay-dependent oscillations in absorption features, due to which-way interferences that arise during the atomic interaction with the two fields [48, 157]. For delays where the XUV and IR pulses overlap, then we observe the IR pulse to, again, alter the absorption line shape of bright states from Lorentzian, but we further observe these XUV absorption features to shift in energy due to the IR pulse inducing a Stark-shift on the atomic energy levels. We also observe the appearance of light-induced states (LISs) (features that only exist while the fields overlap) due to the absorption of XUV light at frequencies corresponding to (XUV $\pm$ IR) processes that move population into dark states. The work of this thesis will not address LISs.

### 5.3 Extending to a macroscopic medium

In Part I of this thesis, our numerical methods focused on solving the semiclassical microscopic problem of a single atom interacting with a laser field. This required only a representation for the atom, a time-dependent electric field, and solving the TDSE for the interaction of the two. Now we wish to focus on the macroscopic problem of a linearly polarized laser field propagating through a gas and interacting with a macroscopic number of atoms. To do this, we need a real space representation for the time-dependent electric field, a real space representation of our gas, and to solve the coupled TDSE and MWE for the light propagating through this medium. This requires more sophisticated field and medium modeling than we have discussed previously in this thesis. We base these numerical methods on work previously described in [57, 158] using cylindrically symmetric fields.

We begin by describing the gas medium, defined in the cylindrical coordinates $r$ and $z$, where $z$ will serve as the propagation direction for the laser. We define $z = 0$ as the center of the gas and the total length to be $z_l$, so that we consider the propagation of the electric field from $z = -\frac{z_l}{2}$ to $z = \frac{z_l}{2}$. We assume the density of the gas is uniform in the radial direction and trapezoidal in the $z$ direction. Radially, the medium ranges from $r = 0$ to $r = r_{max}$, where $r_{max}$ is chosen to ensure that the radial extent of the electric fields are contained. We project the $r$ coordinate onto a grid $r_i = (i - 1/2)\Delta r$ for $i = 1...n_r$, where $\Delta r = r_{max}/n_r$, and the $z$ coordinate onto a grid $z_j = -\frac{z_l}{2} + (j - 1)\Delta z$ for $j = 1...n_z$, where $\Delta z = z_l/n_z$. The goal of this discretization is to use the $z_j$ grid to step the electric field through the gas one plane at a time using the MWE and using the $r_i$ grid in each plane as sample gas atoms that the field interacts with to calculate the atomic response for the source term of the MWE, in order to step the electric field to the next plane. We will more carefully outline this scheme a little further below.

Using this discretization, we can model our electric fields in this coordinate

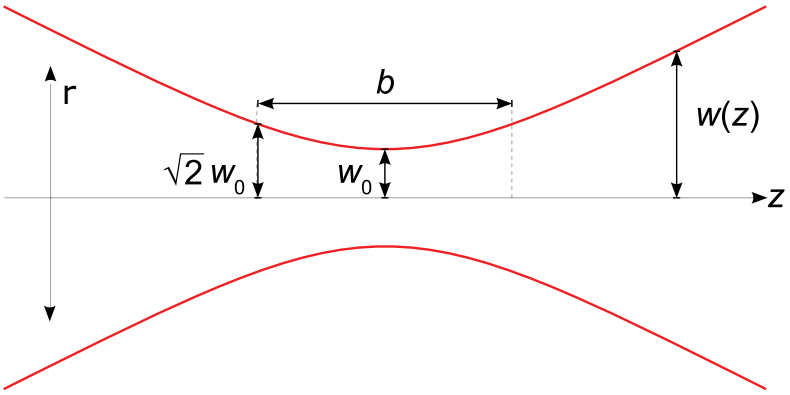


Figure 5.4: Gaussian beam as a function of $z$ and $r$ illustrating the beam waist at the focus, $w_0$, the confocal parameter, $b$, and the waist as a function of $z$, $w(z)$. The spatial profile of the beam is defined entirely by driving wavelength of the beam, the choice of the location of the focus, and the confocal parameter. Adapted from [159], which is released under the Creative Commons Attribution-Share-Alike License 3.0.

system. Because we march the electric fields forward through the gas medium, we need only define them at the beginning of the medium. The initial electric fields are cylindrically symmetric Gaussian beams as illustrated in Figure 5.4. A Gaussian beam is defined by its wavelength, the confocal parameter of the beam, and the location of the focus, which we define relative to the center of the gas medium [160]. Working in the frequency domain, we construct the initial Gaussian pulse for the IR field as

$$\widetilde{E}_{IR}(\omega, r_i) = \frac{\widetilde{\mathcal{E}}_{IR}(\omega)}{1 + 2\left[(z_1 - z_{foc})/b(\omega)\right]^2} \exp\left(\frac{-2r_i^2 k(\omega) b(\omega)}{b(\omega)^2 + 4(z_1 - z_{foc})^2}\right) \exp\left(i\phi(\omega, r_i)\right) \tag{5.5}$$

where $\widetilde{\mathcal{E}}_{IR}(\omega)$ is the Fourier transform of the IR field, $b(\omega) = \frac{b\omega_0}{\omega}$ is the confocal parameter scaled relative to the frequency of the driving wavelength, $\omega_0$, $k(\omega)$ is the wavenumber at that frequency, $z_{foc}$ is location of the focus along our $z$ axis, and $\phi(\omega, r_i)$ is the frequency and radially dependent phase, given by

$$\phi(\omega, r_i) = \left[-\arctan\left(\frac{2(z_1 - z_{foc})}{b(\omega)}\right) + \frac{2k(\omega)(z_1 - z_{foc})r_i^2}{b(\omega)^2 + 4(z_1 - z_{foc})^2}\right] \frac{\omega}{|\omega|}. \tag{5.6}$$

We repeat this using Eq. (5.3) for the XUV field using the driving wavelength of the XUV, a different confocal parameter, and possibly a different focus position to generate $\widetilde{E}_{XUV}(\omega, r_i)$. In setting up the fields this way, we allow ourselves to give the XUV and IR fields entirely different focusing conditions, which allows us to robustly vary the macroscopic properties of the two fields. Summing these two fields, we have the initial electric field at the beginning of our medium, $\widetilde{E}(\omega, r_i) = \widetilde{E}_{IR}(\omega, r_i) + \widetilde{E}_{XUV}(\omega, r_i)$. Currently, we constrain ourselves to a two-color field consisting of an IR field and a single XUV field, such as those illustrated in Eq. (5.2) and Eq. (5.3), but the techniques we demonstrate here are also valid for including multiple XUV fields, such as those used when creating an attosecond pulse train.

Having built models for the field and gas medium, we are ready to approach the MWE. In the time domain, using SI units, the MWE with source terms can be expressed as

$$\nabla^2 E(t) - \frac{1}{c^2}\frac{\partial^2}{\partial t^2} E(t) = \frac{1}{e_0 c^2}\frac{\partial^2}{\partial t^2} P(t). \tag{5.7}$$

Here $E(t)$ is the time-dependent total electric field and $P(t)$ is the time-dependent polarization field representing all source terms for the driving and the generated field. The full solution of Eq. (5.7) is complicated, requiring a very fine resolution in the propagation direction in order to account for forward and backward propagating waves [13, 57]. However, in gases, well below atmospheric density, we can generally safely ignore backward propagating waves since for the regime that we are interested in, the laser and the generated radiation are strongly phase matched in the forward direction. This allows us to transform to a coordinate system moving at the speed of light and apply the slowly evolving wave approximation to the field, where we assume that the electric field changes slowly in the propagation direction in comparison to the driving wavelength (equivalent to ignoring the backward propagating solution)

[14, 57, 158]. This is equivalent to ignoring the second derivative in the propagation direction and allows us to simplify the MWE and express it in the frequency domain as

$$\nabla_{\perp}^{2}\widetilde{E}(\omega)+\frac{2i\omega}{c}\frac{\partial}{\partial z}\widetilde{E}(\omega)=-\frac{\omega^{2}}{\epsilon_{0}c^{2}}\widetilde{P}(\omega). \tag{5.8}$$

We now need to discuss the calculation of the polarization field.

At a given step on the $z_j$ grid, the polarization field can be divided into two parts,

$$\widetilde{P}(\omega,r)=\widetilde{P}_{rad}(\omega,r)+\widetilde{P}_{ion}(\omega,r) \tag{5.9}$$

where $\widetilde{P}_{rad}(\omega,r)$ represents the dipole radiation source term induced by the atomic interaction with the driving field and $\widetilde{P}_{ion}(\omega,r)$ is related to the free-electron contribution to the refractive index, which we generally ignore in this work [13, 57]. We can express $\widetilde{P}_{rad}(\omega,r)$ as

$$\widetilde{P}_{rad}(\omega,r_j)=2\rho(z_j)\widetilde{\mathcal{D}}(\omega,r_j), \tag{5.10}$$

where $\rho(z_j)$ is the gas density at $z_j$ and $\widetilde{\mathcal{D}}(\omega,r_i)$ is the single atom dipole spectrum at point $r_i$, calculated by solving the TDSE for the interaction of the atom and the driving field at the radial grid point (this is what we calculated in Chapter 2). The factor of two in this relationship arises from the fact that, for the noble gases we are considering in this work, there are often two electrons with the same $m$ quantum number that contribute to the response of the atom. This source term generally gives rise to absorption as $\widetilde{\mathcal{D}}(\omega,r_i)$ gives rise to an electric field that is exactly out of phase with the driving field. As we saw in Chapter 2, the dipole, in the time domain, has a long-time contribution arising due to population being left in excited states that would unphysically survive forever in our calculation. We impose a lifetime on this dipole contribution (typically on the order of 60 fs) with a Hanning window, such as we did in Part I of this thesis. This lifetime is typically chosen to give absorption features that are comparable in width with the spectral resolution of experimental spectrometers.

With this source term calculated, we now solve Eq. (5.8) using a traditional Crank-Nicolson approach to march the field forward in space [97]. The general scheme that we use is one of marching the field, expressed in the frequency domain, along the $z_j$ grid, one plane at a time. When the field arrives at a $z_j$ grid point, we inverse Fourier transform the field to the time domain and do a single atom TDSE calculation at every $r_i$ grid point with $z = z_j$ to calculate $d(t)$. We then Fourier transform to the frequency domain and calculate the source term as given by Eq. (5.10). This source term is then used to propagate the full electric field to the next plane in $z$. This approach results in the propagating fields experiencing dispersion and linear and nonlinear absorption and emission in a realistic and self-consistent way. This allows us to describe ultrafast or dynamical reshaping of an XUV pulses due to the interaction with a medium, as well as study processes due to the combined response of a strong IR field and an XUV field that are important in getting good agreement with ATA experiments.

At the end of the medium, we calculate the macroscopic optical density (OD) from the electric field to compare with experimental observations. The OD is given by [161, 162]

$$\mathrm{OD}(\omega) = -\log_{10}\left[\frac{I_{out}(\omega)}{I_{in}(\omega)}\right], \tag{5.11}$$

where $I_{out}$ is the intensity of light at $\omega$ coming out of the gas (end of the medium) and $I_{in}$ is the intensity of the light at $\omega$ going into the gas (beginning of medium). To date, the majority of ATA experiments have assumed that features observed in this OD can be attributed only to the single atom response to the two-color field. This assumption is based off of Beer's law for dilute gas-absorption, which is valid in the thin gas limit. Beer's law can be expressed as

$$I_{out}(\omega) = I_{in}(\omega)e^{-\rho\sigma(\omega)z}, \tag{5.12}$$

where $I_{out}$ is the intensity of light at $\omega$ coming out of the gas, $I_{in}$ is the intensity of the light at $\omega$ going into the gas, $\rho$ is the gas density, $z$ is the propagation distance, and $\sigma(\omega)$ is the single-atom absorption cross section, which is given by the single atom response function of equation 5.4 through the relationship, in SI units,

$$\sigma(\omega) = 4\pi\alpha\omega\widetilde{S}(\omega)/|\widetilde{\mathcal{E}}(\omega)|, \tag{5.13}$$

where $\alpha$ is the fine structure constant [158]. This means that in the thin-gas limit, the OD can be expressed as

$$\mathrm{OD}(\omega) = -a\rho\sigma(\omega)z, \tag{5.14}$$

where $a$ is just the constant of proportionality to change logarithm bases from base 10 to base $e$.

Here we see that in the thin gas limit, the OD is directly proportional to the single atom absorption probability and that this response scales linearly with both the length of the gas medium and the density of the gas. This thin gas limit assumption ignores all macroscopic effects on the XUV absorption spectrum that could result from the XUV and IR fields propagating through the gas medium, such as temporal and spectral pulse reshaping, defocusing due to atomic ionization, or phase matching effects. While this seems like a large assumption, it has been very successful in explaining the absorption features in most ATA experiments. So much so, that that very little work has been put into studying macroscopic effects on ATA experiments, with much of the work being published just in the last 4 years [48, 149, 161–168]

However, as the field of ATA moves toward more dense systems, better understanding how the XUV absorption spectrum can be influenced by macroscopic effects when the thin gas limit breaks down is going to be important. One illustration of this can be seen in Fig. 5.5, where we can see the breakdown of Beer's law for ATA in a dense gas. In this figure we show the calculated macroscopic OD around the $2p$ (21.1 eV) line shape of helium for a laser pulse passing through a low density gas (red) or a high density gas (blue), calculated by solving the coupled TDSE and

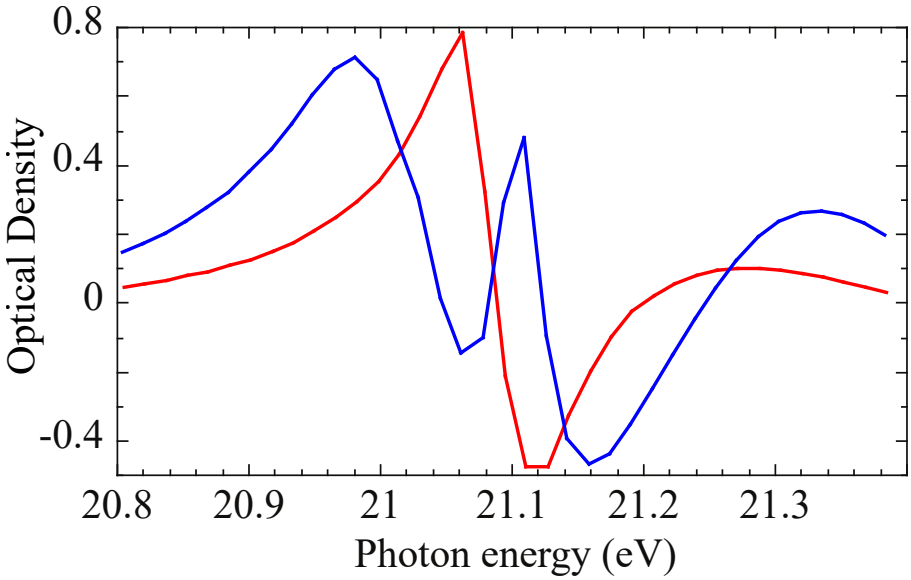


Figure 5.5: Macroscopic absorption line shape in helium around the $2p$ energy level (21.1 eV) for a low density gas medium (red) and a high density gas medium (blue).

Maxwell wave equation (MWE) for a weak 800 nm IR pulse and a $2p$ resonant XUV pulse, with zero relative delay. The low density gas results show the expected single atom response of a general dispersive shape, similar to the $2p$ line shape that we observed around $2p$ in Fig. 5.3. Beer's law would predict that increasing the density should result in the same same absorption line shape, but with increased magnitudes of absorption and emission. However, the high density gas result illustrates a $2p$ absorption line that looks much different than the single atom prediction, showing the appearance of narrow features representing positive absorption in the center of the line, at the $2p$ resonance energy. This feature can only be understood inside the realm of macroscopic effects, and we discuss it in more detail in Chapter 6 [48]. Needless to say, however, if one were trying to infer the ultrafast dynamics of the electron with the high density absorption line shape, macroscopic effects are something that would definitely need to be understood and accounted for in any interpretations.

# Chapter 6
# Resonant pulse propagation

We next discuss a specific example of a macroscopic effect in transient absorption: resonant pulse propagation (RPP). RPP is a general temporal reshaping phenomenon that occurs when a pulse propagates through a medium and excites a long lived resonance (relative to the duration of the driving pulse) [169,170]. Historically, RPP has been ignored in attosecond transient absorption, as the samples studied are usually not dense enough to lead to substantial reshaping. However, RPP has recently been shown to directly alter the absorption line shape of an XUV pulse propagating through a dense gas medium with an IR dressing field [161]. This is important because in a typical transient absorption experiment, we rely on the assumption that the absorption line shape will only depend on the XUV-IR delay, in order to infer dynamics [79, 111, 148, 171–173]. RPP introduces new line shape modifications and must be well understood to properly interpret line shapes measured in experiments. This makes it an important physical process to explore for transient absorption, as the field shifts toward studying more dense media, where RPP reshaping will be unavoidable.

This chapter focuses on exploring and understanding RPP spectral reshaping, in order to help disentangle macroscopic reshaping of the absorption line shape from the IR controlled absorption line shape. In section 1, we give an introduction to the RPP macroscopic phenomenon and discuss the spectral changes it can introduce to a transient absorption line shape. Section 2 focuses on understanding the macroscopic dependence of this RPP spectral reshaping, illustrating how it depends on the macroscopic variables of length and pressure, and exploring the interplay with the IR pulse. Finally, in section 3, we discuss some of the interesting physics to be explored going forward.

## 6.1 Resonant pulse propagation and transient absorption.

When a pulse propagates through a medium and excites a long-lived resonance, its time structure will undergo RPP reshaping. This is in Fig. 6.1 for a 5 fs XUV pulse propagating through a 16 Torr helium gas medium, where the XUV pulse is resonant with the $1s - 2p$ helium transition, which has an imposed dipole lifetime time of 100 fs. Here we see that as the pulse travels through the medium, it develops a tail consisting of a series of subpulses. The electric field in each subsequent subpulse is $\pi$ out of phase with the subpulse before it and also has a longer duration, but is weaker than the previous subpulse. The amount of reshaping that the pulse undergoes depends on the optical thickness $Pz$, where $P$ is the pressure of the gas and $z$ is length of the medium. Throughout this chapter, we will discuss calculations

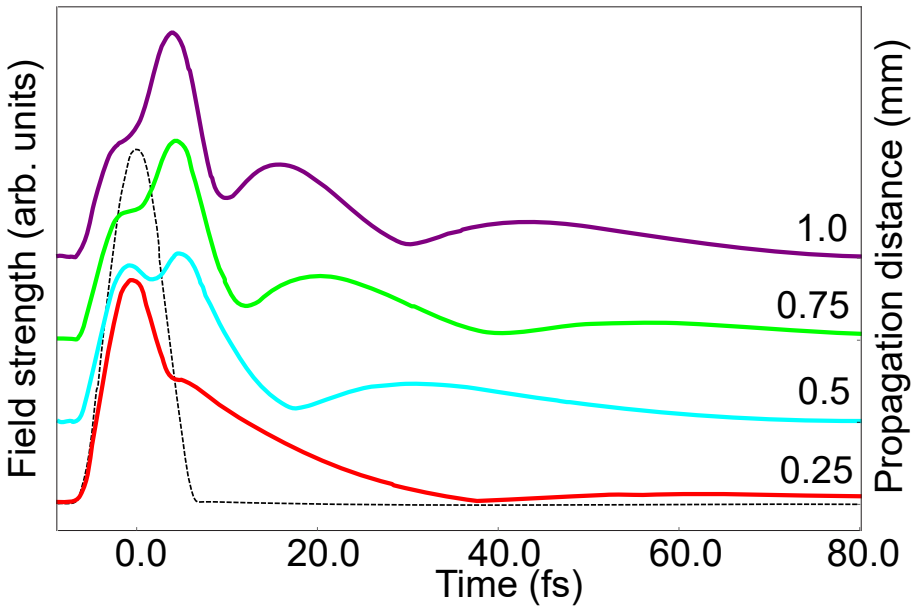


Figure 6.1: Demonstration of resonant pulse propagation temporal reshaping of a 5 fs XUV pulse propagating through a 16 torr helium gas for which the XUV light excites a resonance with a 100 fs dipole lifetime. Shown is the XUV electric field profile at different propagation distances up to 1mm, with the initial pulse illustrated by the dotted line. The XUV pulse quickly develops a long tail consisting of several subpulses that shorten with propagation. Reprinted from [162] with permission.

where we vary the pressure of the medium, however, note in our calculations that we are actually changing the atomic density of the gas. We translate this atomic density into a pressure to better compare with experiment, which has a better grasp over pressure than atomic density. Considering a fixed volume, pressure and atomic density are linearly related and in this work an atomic density of $1e17$ per $cm^2$ corresponds to a pressure of 5 Torr.

As outlined in [161], in the temporal domain we can understand this RPP temporal reshaping of the XUV as a consequence of the long tail of the electric field, generated by the resonantly excited time-dependent dipole moment. The duration of this tail is determined by the effective lifetime of the dipole coherence and is out of phase with the driving XUV pulse, which leads to absorption at the excited state energy. As this long tail of the electric field propagates through the medium, it will excite new time-dependent dipole moments that give rise to electric fields out of phase with the tail. This eventually gives rise to a new subpulse, where the phase changes by $\pi$. This new subpulse then excites new time-dependent dipole moments that give rise to electric fields out of phase with this generating subpulse and the process repeats as the XUV propagates through the medium. We can observe this occurring in Fig. 6.1, which by 1 mm has three subpulses built into its time structure, in addition to the initial pulse. Overall, this leads to a reduction in total absorption, as compared to Beer's law [48, 161, 162]. In the spectral domain, RPP can be less intuitively understood as an effect of accumulated spectral phase due to

temporal dispersion [161].

This RPP phenomenon has been studied in many previous contexts, [169, 170, 174–177], but has only recently been applied to ATA [48, 161, 162]. Historically, RPP has primarily been studied in the time domain [169, 170, 174, 175, 177]. This is because most previous studies focused on RPP for a single resonant pulse traversing a medium. We demonstrate the temporal and spectral results of studying RPP reshaping when no other field is present in Fig. 6.2 (a) and (b). We show the calculated time profile of the electric field and the spectral profile of the OD (the absorption line shape), respectively, for an XUV field resonant with the $2p$ resonance of helium (21.1 eV) traversing a low (red) and high (blue) pressure gas medium. In the time domain, the effects of RPP are obvious when comparing the low and high pressure mediums, but in the frequency domain the shape of the spectral profile is essentially the same in both cases. The larger width in the high pressure case can be understood from the shorter effective lifetime imposed by the first subpulse ending much earlier than in the low pressure case. In the time domain, we can

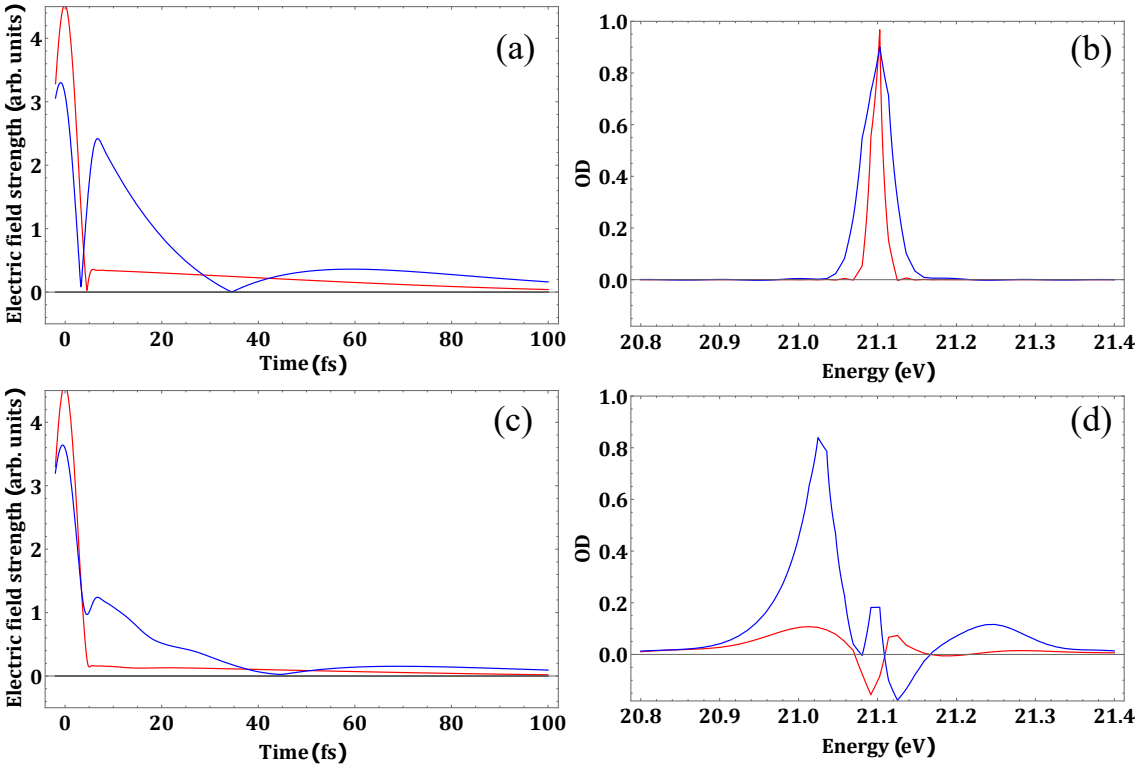


Figure 6.2: (a) Time profile of a 5 fs XUV pulse propagating through a .4 Torr (red) and 4 Torr (blue) helium gas over a distance of 1 mm, in which the XUV light excites a resonance with a 180 fs dipole life time and (b) shows the corresponding (by color) absorption line shape. (c) and (d) show the same thing as (a) and (b), respectively, but with a 1e12 W/cm$^2$, 770 nm, 12 O.C. FWHM IR pulse, with 0 relative delay with the XUV pulse, copropagating through the medium. Note that in (d), we have scaled the OD of the high pressure line shape by .6 to make the comparison between the two easier.

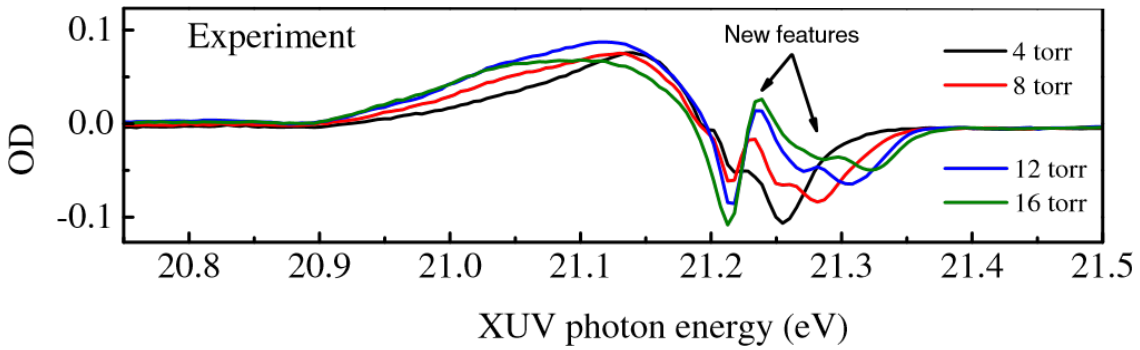


Figure 6.3: Experimental OD spectra around the He $1s2p$ state in the prescence of the IR field, and at different backing pressures. At low pressures we find primarily a Fano-like line shape, but as the pressure is increased, new narrow spectral features related to RPP appear. The experiment used a 40 fs FWHM duration, 786 nm IR pulse with a peak intensity of 3 TW/cm$^2$ and a 4 fs FWHM APT composed of H13, H15, and H17 (1:10:6 ratio) with a peak intensity of $10^{10}$ W/cm$^2$ and the OD is shown for zero delay. Adapted from [161] with permission.

point to distinctive subpulses and observe when new subpulses develop as the pulse propagates through the medium, but in the frequency domain there is nothing in the line shape that can be pointed to as a characterization of the buildup of these subpulses.

In transient absorption, however, we use two pulses: an XUV pulse which generally excites one or more resonances in the medium, and a moderately strong IR pulse which dresses the excited states and therefore introduces changes to the absorption line shape [149, 150, 155]. We demonstrate the changes to the observation of RPP that result from adding this second field in Fig. 6.2 (c) and (d). Here we show the same plots as in Fig. 6.2 (a) and (b), but now with a moderately strong IR pulse traversing the medium with the XUV pulse (relative zero delay between the pulses). In the time domain, we see similar reshaping of the XUV pulse, though slightly modified from the no IR case. In the frequency domain, however, we observe a significant change to the line shape behavior. At low pressure, the absorption line shape, due to the IR coupling the excited state to nearby states [150], now has a general dispersive line shape. The high pressure line shape is still recognizable as generally dispersive, but is distorted and broadened, and a new sharp peak has appeared in the line shape at the resonant energy. The broadening and general distortion of the line shape is related to the shortening of the first subpulse, while the sharp peak at 21.1 eV is directly due to the buildup of the second subpulse in our electric field. If we were to look at higher pressures, we would see more distortion and broadening of our line shape as the first subpulse continued to shorten, as well as more sharp peaks appear around the resonant energy as more subpulses built up in our electric field. This indicates that transient absorption presents a unique opportunity to study and observe RPP effects in the frequency domain.

The first application of RPP to transient absorption arose from experiments performed by Arvinder Sandhu's group at the University of Arizona [161, 162]. They

performed transient absorption experiments in a 10 mm long helium gas cell with different backing pressures. The experiment used a 40 fs FWHM duration, 786 nm IR pulse with a peak intensity of 3 TW/cm$^2$ and a 4 fs FWHM attosecond pulse train (APT) with a peak intensity of $10^{10}$ W/cm$^2$ that was resonant with the $2p$ and $np$ ($n > 4$) excited states of helium. At low pressures, the experimentalists observed a Fano-like line shape around the $2p$ resonance. However, with increased pressure, they observed the line shape to broaden and develop new, narrow features. We show this in Fig. 6.3, where we illustrate the new, narrow, spectral features near the resonant energy due to the buildup of additional subpulses in the electric field. This experimental observation is the first illustration of RPP features appearing in transient absorption experiments and demonstrates, in practice, that RPP can introduce a strong distortion to the absorption profile of the XUV pulse at pressures already reachable in the lab. Currently, this RPP buildup on the $2p$ resonance of helium is the only experimental observation of RPP in a transient absorption experiment.

To a first order approximation, it has been shown that RPP is a phenomenon that occurs independent of the added IR, depending primarily on the macroscopic variables of the medium, gas pressure and length [48, 161, 162]. Of course, we have already seen a demonstration that RPP reshaping can be influenced by the IR, *i.e.*, the difference in the high density time profiles of Fig. 6.2 (a) and (c). However, this influence in the spectral domain is much harder to observe. In the next section, we explore how the RPP line shape modification depends on the macroscopic variables, generally explain how the line shape evolves with increased optical thickness, and highlight the break down of the first order approximation, discussing when the IR becomes important to consider. We will also pay particular attention to defining macroscopic regimes when RPP reshaping can be considered as a perturbation to our line shape, and essentially ignored, and when the macroscopic reshaping is too drastic to ignore.

## 6.2 Understanding the RPP line shape modification

To explore the OD line shape modification with respect to the macroscopic variables, let us first explore, in more detail, how we expect the time profile reshaping to depend on these macroscopic variables. In the limit of the excited resonance lifetime, $\Gamma$, being much longer than the duration of the exciting pulse, we expect the resulting RPP modified electric field after a medium of length $z$, with a pressure $P$, to have a temporal envelope related to a first-order Bessel function in the following way [162, 175]:

$$E(t, z) \propto \frac{J_1(\sqrt{a\sigma_0 \Gamma P z t})}{\sqrt{t}}, \tag{6.1}$$

where $a$ is a proportionality constant and $\sigma_0$ is the absorption cross section at the resonant energy considered. We show the related temporal envelope of Eq. (6.1) in Fig. 6.4, such that $a\sigma_0\Gamma P z = .5$ per O.C. (black), and $a\sigma_0\Gamma P z = 1$ per O.C.

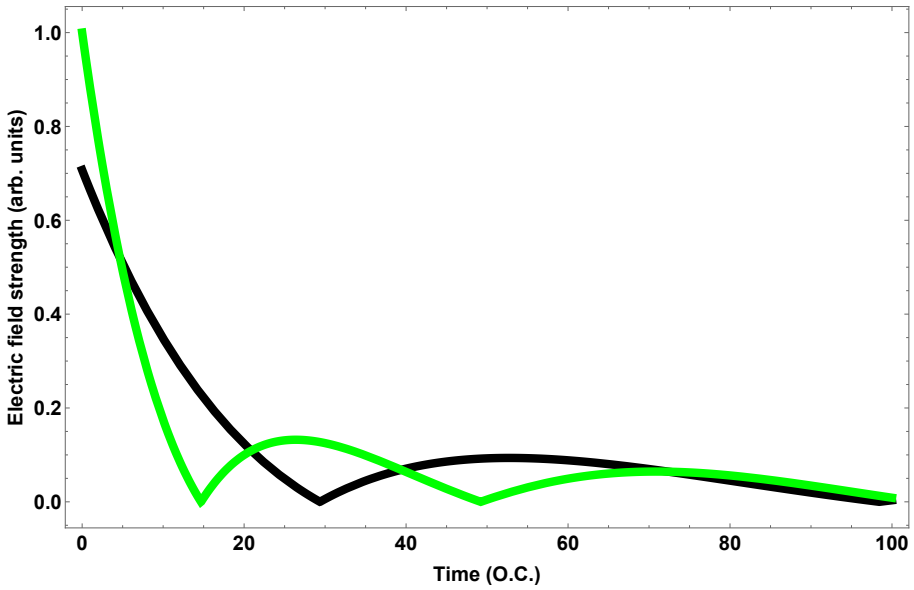


Figure 6.4: Demonstration of how RPP temporal reshaping varies with the product of $\sigma_0 \Gamma P z$. Here we show the temporal profile of Eq. 6.1 for $a\sigma_0 \Gamma P z = .5$ per O.C. (black) and 1 per O.C. (green). For a given resonance, this serves to illustrate increasing the optical thickness, $Pz$. However, it can also serve to illustrate the different RPP temporal reshaping of resonances with different lifetimes or absorption cross sections.

(green). In this figure, we see two distinct subpulses in the black curve, ending at 30 O.C. and 100 O.C., while we observe three subpulses in the green curve, ending at 15 O.C., 50 O.C., and 100 O.C. This demonstrates that over a fixed time duration, such as we consider in our calculations, the number of subpulses and their duration depend directly on this $a\sigma_0 \Gamma P z$ quantity. As this number gets larger, we expect more subpulses to build up in our field and the duration of each subpulse to get shorter (but still remain longer in duration than the previous subpulse). With this, we can make two clear observations: (i) The $\sigma_0$ dependence of this reshaping illustrates why RPP reshaping has currently only been observed experimentally for the $2p$ state of helium, which has a very large $\sigma_0$ [158]. (ii) For a fixed resonance, $\sigma_0$ and $\Gamma$ are constant and thus, in an experiment, the RPP reshaping of an electric field depends directly on the optical thickness of the medium, $Pz$. This is important because so far we have only considered the line shape modification with respect to pressure, but this highlights that we expect this RPP spectral modification to equally depend on the length of the medium. We explore this below.

We can verify that the evolution of the OD line shape with increased pressure is equivalent to the evolution with increased propagation distance by considering Fig. 6.5. Here we show a theoretical study of the evolution of the OD as a function of distance for two different pressures, 4 Torr in (a) and (b) and 8 Torr in (c) and (d). In order to directly see the equivalence between pressure and distance, it is helpful to compare the 1 mm lineout in (a) (gray) to the .5 mm lineout in (c) (orange). These two lineouts share an optical thickness value, and we indeed see that the two curves

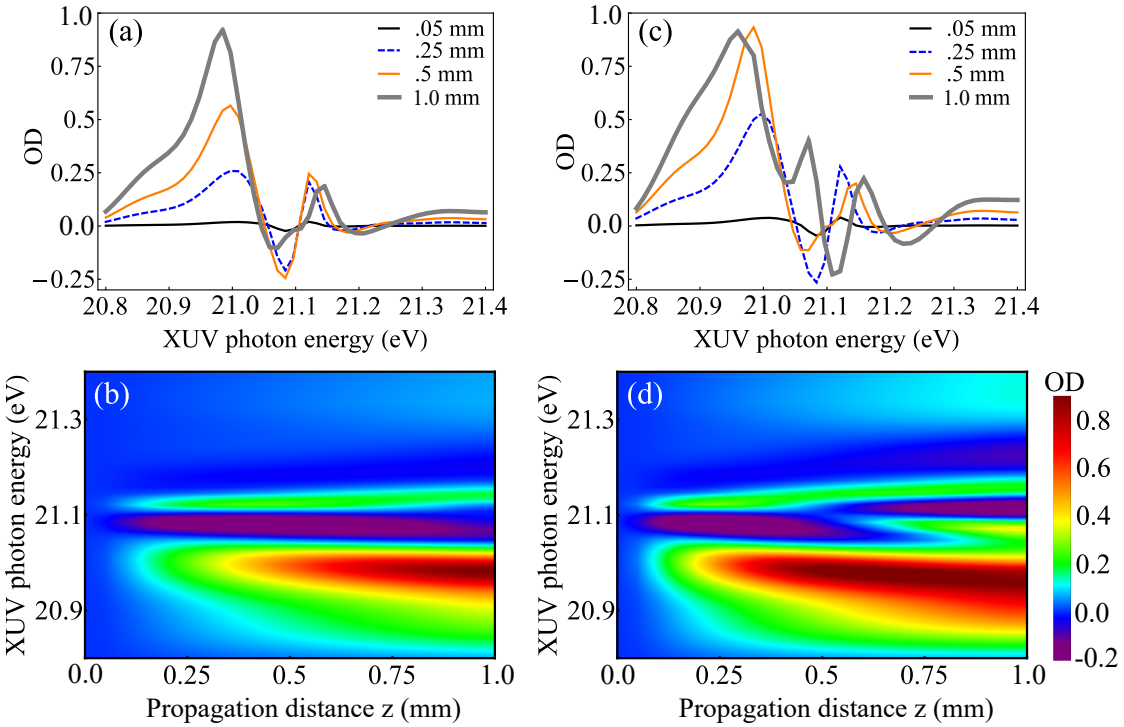


Figure 6.5: (a,b) Calculated OD as a function of propagation distance for the case of a 4 Torr medium with a 5 fs, 2p resonant XUV pulse and a 12 O.C. FWHM IR pulse with intensity of 2.25 TW/cm$^2$ at delay zero. Panel (a) shows lineouts from panel (b) at four different propagation distances. (c) and (d) show the same values as (a) and (b), respectively, but for an 8 Torr medium. Reprinted from [162] with permission.

are the same. We can also compare the .5 mm lineout in (a) (orange) to the .25 mm lineout in (b) (blue, dotted), which also have the same optical thickness, and again the curves are the same. Further, in comparing the density plots of (b) and (d), it is clear that the evolution with distance that the 4 Torr calculations experience over 1 mm is the same evolution that the 8 Torr calculations experience over .5 mm. This serves to highlight that an important quantity to consider, when thinking about the evolution of the RPP OD reshaping, is optical thickness. This is nice because it is a value that can be easily explored both experimentally and theoretically, to investigate how the line shape evolves with increased RPP reshaping.

With this understanding that, macroscopically, we expect the RPP reshaping of the OD to evolve with increased optical thickness, we are now ready to study this evolution. In order to do this, we consider the experimentally measured OD as a function of pressure, shown in Fig. 6.6. This allows us to consider the absorption line shape as the optical thickness increases. We can characterize the pressure-dependent absorption line shape behavior of Fig. 6.6 into distinctive pressure regimes: (i) As the pressure increases from 1 Torr to 4 Torr, the only change that we observe to the absorption line shape is a linear broadening effect. For this regime, we observe a broadened single atom response. (ii) At 5 Torr, we see the appearance of the

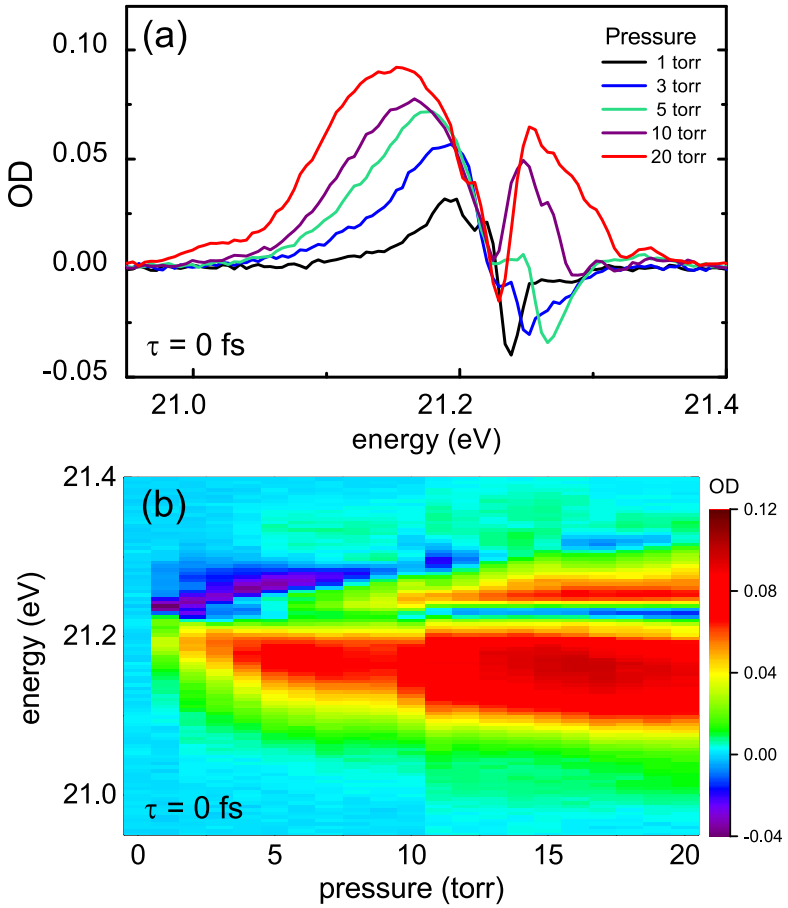


Figure 6.6: (a,b) Experimentally measured OD as a function of backing pressure for the case of IR intensity of 2.25 TW/cm$^2$ at delay zero with an XUV resonant with the $2p$ resonance in helium, with the rest of the pulse parameters being given in Fig. 6.3. Panel (a) shows lineouts of panel (b) at different pressures. Adapted from [162] with permission.

new, sharp spectral feature. From 5 Torr to 10 Torr, we see the linear broadening of the line shape slow down and the new spectral feature build up in strength. In this regime, the line shape is recognizable as the sum of the broadened single atom response and this new sharp peak. (iii) For pressures above 10 Torr, the broadening of the line shape seems to almost stop, and the new spectral feature rapidly grows in strength, dominating the line shape around resonance and leading to a highly distorted absorption line shape. For this regime, the absorption line shape of the single atom response is generally unrecognizable and results from the break down of our first order approximation that the IR effects are negligible.

We can understand these different spectral reshaping pressure regimes by discussing the RPP temporal reshaping that occurs in each regime: (i) For this pressure regime, the only temporal reshaping that occurs is the shortening of the first subpulse. This effectively reduces the lifetime of the excited state, leading to broader absorption features and giving rise to linear spectral broadening. In this regime,

there are no real changes to the physics at the single atom level, so we generally observe the single atom response. (ii) At 5 Torr, we build a second subpulse into our electric field. This second subpulse is much longer than than the first subpulse and gives rise to a new spectral feature that is more narrow than the original line shape. The second subpulse is also $\pi$ out of phase with the first subpulse, changing the characteristic absorption, *i.e.*, if the first subpulse led to emission at resonance, then the second subpulse leads to increased absorption. With increased pressure, this second subpulse shortens and builds in strength, leading to broadening and growth of this new absorption feature. In this regime we also see the slow down of the linear broadening of the primary absorption line shape. This is due to the first subpulse beginning to reach a duration length that is comparable to the IR duration, which slows the broadening effect due to the interaction with the IR pulse [161]. In this regime the physics driven by each subpulse is generally independent of the other, so we see the absorption line shape as the sum of the contribution from the two subpulses. (iii) For this regime, the first subpulse shortens to within the IR duration. This leads to the IR imposed phase shift on the time-dependent dipole moment decreasing as we increase the pressure, fundamentally changing the line shape related to this subpulse (shifting it back toward Lorentzian). While this is happening, the second subpulse continues to shorten and build up, leading to a extremely strong and broad feature. These two effects lead to a line shape that is unrecognizable from the single atom expectation.

While this evolution of the absorption line shape with increased optical thickness is very general, the upper pressure regime, where the line shape becomes unrecognizable from the single atom response, clearly depends on the IR pulse. This is because the third regime begins when first subpulse is comparable in duration to the IR pulse. If we were to repeat the above study for an experiment using a shorter duration IR pulse, then we would extend the second pressure regime much further. That is, we would build in the second subpulse to our field at the same optical thickness, but it would take much more optical thickness to shorten the first subpulse to be comparable in duration to the shorter IR pulse. This would lead to the build up of more sharp features in our line shape, but we would still generally be able to observe them as added to our single atom response, and disentangle the two. Equally, with a longer IR duration, we would observe the second pressure regime to end much earlier with a weaker sharp feature before the line shape became unrecognizable.

As we have previously stated, in transient absorption we are concerned with interpreting the absorption line shape assuming a single atom response controlled by the IR pulse and its relative delay to the XUV. This means that we can accept RPP spectral reshaping, so long as we can easily disentangle it from the single atom response. In the above paragraphs, we saw that we are able to observe RPP spectral reshaping as simply a perturbation of sharp features to our single atom line shape so long as the first subpulse was longer in duration than our IR. This directly gives us a criteria for when macroscopic effects related to RPP can no longer be ignored in transient absorption: When the first subpulse is comparable to or shorter than the duration of the perturbing IR pulse [161].

### 6.3 Interesting physics going forward.

Understanding how RPP spectral reshaping in transient absorption occurs with increased optical thickness proved to be a very powerful tool. It highlighted when macroscopic effects can be ignored, or accounted for, and when macroscopic effects can greatly alter a result. We also saw the role of the IR in altering the spectral result. With a good grasp on how RPP depends on optical thickness, we believe there are many interesting ways forward in the future study of RPP in transient absorption. This section will briefly highlight some of the interesting physics to be explored in this topic.

In Fig. 6.2, we saw that the RPP temporal reshaping changed slightly when we introduced an IR pulse. However, it turns out that this change in the temporal profile is highly sensitive to the duration of the IR pulse. We illustrate this in Fig. 6.7(a), where we compare the XUV temporal reshaping for two different duration IR pulses. Here we see that the longer duration IR pulse introduces a kink into the temporal profile at around 18 fs and moves the zero of the field back from 20 fs, for the short duration pulse, to 30 fs. Longer pulses would introduce more changes to the XUV temporal profile and shorter pulses would approach the XUV only temporal profile. Currently this effect has been observed theoretically, but it is not well understood currently. A better understanding of how the RPP temporal reshaping is influenced by the IR could provide great insight into the interplay of RPP and IR in a transient absorption experiment. A better understanding of this interplay could also potentially lead to better control over the IR induced spectral

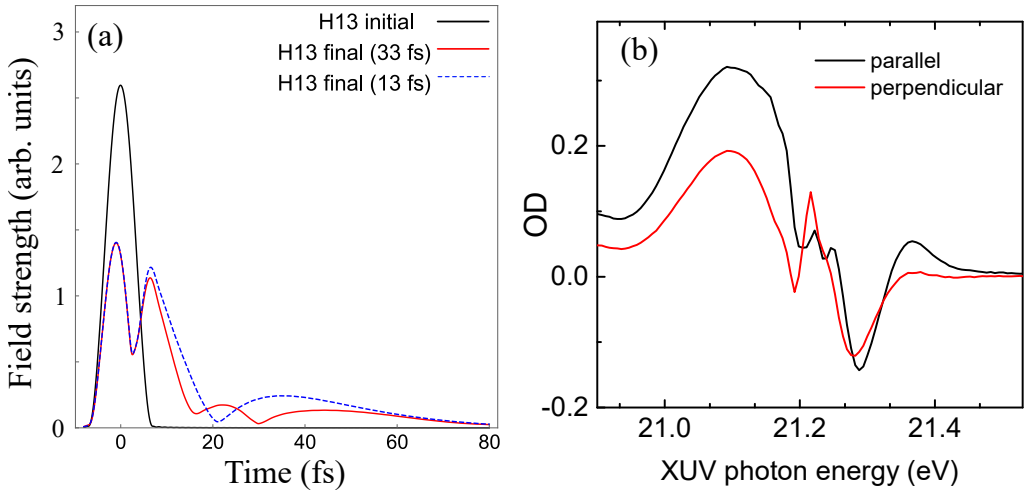


Figure 6.7: (a) Calculated XUV time profiles at the beginning (black) and end (solid red or dashed blue) of the helium gas at a pressure of 8 Torr, dressed by a 2.25 TW/cm$^2$ IR pulse. The final time profiles for two different IR pulse durations are shown, 33 fs (solid red) and 13 fs (dashed blue). The imposed lifetime is 100 fs and the XUV pulse is resonant with the $2p$ transition in helium. (b) Experimentally measured OD for an XUV pulse propagating through a helium medium with either parrallel or perpendicularly polarized IR pulse. Adapted from [162] with permission.

reshaping that occurs when the first subpulse of the XUV tail is comparable to the IR.

Another interesting avenue for studying the interplay of RPP and the IR pulse lies in explicitly studying the dependence of RPP reshaping on the polarization of the copropagating IR pulse, with respect to the polarization of the XUV pulse. Previously this topic has been explored experimentally and theoretically for case of parallel and perpendicular pulses [162]. In Fig. 6.7(b), we show the experimentally measured OD for an XUV pulse propagating with an IR pulse that is polarized parallel (black) or perpendicular (red) with respect to the polarization of the XUV pulse, demonstrating that the line shape and RPP spectral reshaping can explicitly depend on the polarization of the IR. Currently, theoretical calculations exploring this polarization dependence have been based on simple models, and full MWE-TDSE calculations with truly perpendicular polarizations of the fields have yet to be explored in this realm of study. Beyond the spectral domain, it would also be very interesting to study how the temporal structure changes with the polarization angle of the IR pulse as well. In extension of this work, studying RPP temporal and spectral reshaping for elliptically polarized XUV and IR pulses could further explore the interplay of RPP with the IR pulse.

Lastly, we again say that this RPP spectral reshaping effect has currently only been observed in the $2p$ excited state of helium. Exploring the effect on other atomic resonances could be very interesting and allow for rich exploration of the interplay of different resonant effects with RPP. For example, we could imagine studying two excited states that simulataneously demonstrate RPP reshaping (in the same experiment), and exploring how the temporal and spectral reshaping varies when the two states are resonantly coupled by two IR photons. We could also explore RPP in doubly-excited states of helium. These autoionizing states inherently have a Fano-characteristic line shape and much shorter lifetimes, allowing for interesting comparisons to be made against the RPP reshaping of singly excited states [43,178]. Exploring RPP in other singly and double-excited states opens up an entire realm for exploration interesting physics related to resonant interactions in strong field laser physics.

# Chapter 7
# Space-time control of XUV light using an IR pulse

Strong field laser physics has built up around the central hub of being able to control and manipulate light. This control is what allows us to use intense IR, visible, and near ultraviolet laser beams in increasingly elaborate experimental schemes [179–181]. One important aspect of this control is the ability to manipulate the direction that light pulses are traveling in. With the recent development of XUV light sources from HHG [9–11,44,45,47,50,63] and soft X-ray light sources from free electron lasers [182,183], there is now a growing need to be able to spatially control short wavelength light. However, optics in this regime are very difficult to make and, even when constructed, are typically very inefficient [184]. In this chapter we demonstrate a new technique that we have developed for controlling the direction of XUV and x-ray light, in collaboration with Johan Mauritsson's experimental group at Lund University [43]. This chapter will focus on the control of XUV light, however, it is perfectly applicable to x-ray light.

We divide the chapter into four sections: First, we introduce our technique for spatially controlling XUV light using an opto-optical modulator (using light to control light). This XUV light originates as free induction decay (FID) from atoms excited by an XUV pulse, and is controlled by the subsequent application of an IR pulse. This is done in a transient absorption setup in which the XUV and IR pulses are not coaxial. In section 2, we show experimental results demonstrating this control in an argon gas. In particular, we investigate the temporal and spectral properties of the controlled emission. In section 3, we show calculations illustrating the spatial control in a helium gas for a different beam geometry. We also use the theoretical framework to look at the spectral and temporal properties of the emission, comparing the results to the experiment. We then close the chapter with a brief summary. Note that this chapter follows closely with the work presented in [43].

## 7.1 Introduction

Fig. 7.1 illustrates the XUV spatiotemporal control scheme. We excite a gas of atoms with a resonant XUV pulse, and then use an IR pulse to sweep the light emitted by the excited atoms in a direction of our choosing. This resonant emission, referred to as FID, is the long-lived dipole response that we have discussed in previous chapters [84,161,162,185–188]. In the absence of an IR pulse, this light is

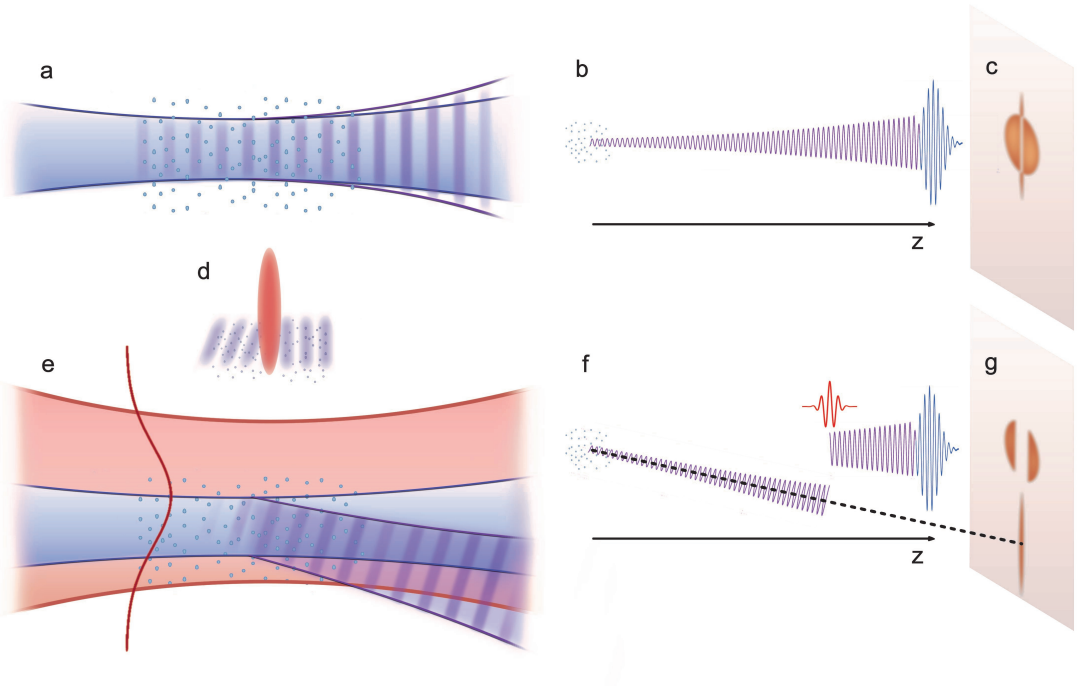


Figure 7.1: Schematic illustration of FID radiation control. (a) A gas of atoms excited by an XUV pulse emit FID radiation (purple) after the XUV pulse (blue) has passed. The atoms oscillate in phase orthogonal to the propagation direction of the excitation pulse (illustrated by the vertical purple lines). Phase matching creates a well-defined FID beam. (b) The temporal structure of the FID emission decays over a long time. (c) The phase relation between the excitation pulse and the FID leads to destructive interference at the detector in the far-field, giving absorption. (d) An IR pulse (red) that co-propagates with the XUV pulse through the medium creates a spatially dependent phase shift of the dipoles via the AC-Stark effect. This phase shift depends on the integrated IR intensity for each atom and results in a rotation of the wave fronts after the IR pulse. (e) This rotation redirects the FID emission after the IR pulse. (f)-(g) In the far field this yields an off-axis emission component as well as an altered on-axis absorption. Reprinted from [43] with permission.

emitted primarily in the same direction as the excitation pulse and, because it has the opposite phase, appears as absorption in the XUV spectrum, as demonstrated in Fig. 7.1 (a)-(c). We can understand how the IR pulse can alter the direction of FID emission by considering the phase shift imposed on the XUV emission by the IR. In a single interaction plane (assuming $z$ is the propagation coordinate), we can express this phase shift as:

$$\Delta\varphi(x,y) = \int_{\mathrm{T_{IR}}} \frac{\Delta E(x,y,t)}{\hbar}\mathrm{dt}, \tag{7.1}$$

where $\Delta E$ is the intensity-dependent shift of the energy levels and $T_{IR}$ is the duration of the IR pulse [79, 111, 147, 149, 156, 161, 189, 190]. In a typical transient absorption setup, the XUV beam is coaxial with the IR beam and spatially much narrower. This leads to all of the atoms interacting with the XUV pulse experiencing roughly the same IR intensity, and thus the same phase shift. However, if we break this coaxial symmetry, but keep the beams collinear, as observed in the beam setup of Fig. 7.1 (e), then we can set up a situation where some atoms interacting with the XUV pulse experience large IR intensities (large phase shift) and other atoms experience small IR intensities (small phase shift). This puts a spatial gradient on the phase of the induced FID electric field, which leads to the turning of the fields wavefront and a change in the propagation direction. This is shown in Fig. 7.1 (d) and (e). In a typical transient absorption setup, this wavefront is unaffected because the entire field experiences the same phase shift, thus the FID emission travels along with the excitation pulse.

This turning of the electric field can be intuitively understood as a similar effect to that of light passing through a prism wedge [191], such as we show in Fig. 7.2. As is well known, when visible light interacts with a prism wedge, the direction of propagation is changed. This change in direction is similarly a result of a spatial phase gradient being put on the electric field. This phase gradient results from the fact that as the light passes through the wedge, it accumulates a phase proportional to the thickness of the wedge where the light passed [191]. This means light passing through thick portions of the wedge will experience a large phase shift and thin portions will lead to small phase shifts. This inputs a spatial phase gradient across the electric field after it passes the wedge and results, similarly, in a change in the direction of the wavefront of the field. Note that the difference in the spatial direction of the resulting electric field between Fig. 7.2 and Fig. 7.1 (e), which are both oriented so that the larger magnitude phase shift is towards the top of the page, is a result of the signs of the phase shifts being opposite. The change in direction of the wavefront to an imposed spatial phase shift is dependent on the slope of the phase shift, and not just the magnitude.

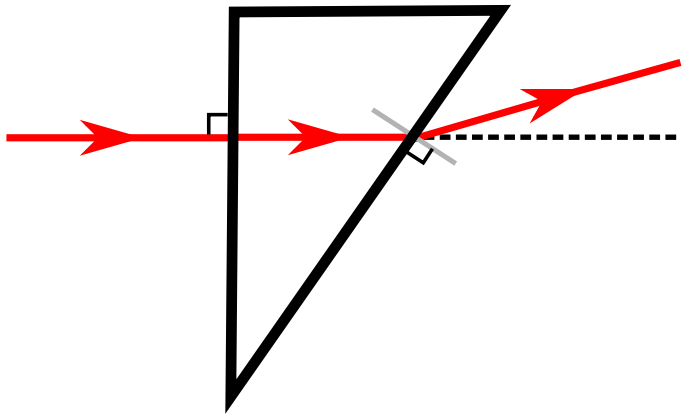

Figure 7.2: Illustration of a wedge prism changing the travel direction of light passing through it.

While similar to the prism, our technique of using an IR pulse to impose the necessary spatial phase shift on the FID has a unique difference. When a light pulse is incident on a prism, the entire pulse will pass through and be redirected, indiscriminately. That is, at the femtosecond time scale the prism can not be inserted to redirect some portions of the incident beam and then removed to not redirect other portions of the beam. However, our direction modulator does allow us to choose to redirect specific portions of the FID emission, because we can control the delay between the excitation pulse and the IR. We can thus send an XUV into a gas of atoms to induce FID, which is initially emitted in the same direction as the excitation pulse, and then come in with an IR pulse at a later time and redirect the remainder of the FID in a direction of our choosing. This is demonstrated in Fig. 7.1 (f), where the FID that occurs before the IR pulse travels in the same direction as the excitation pulse, but the FID after the IR is sent in a new direction. Further, we could come along with a second IR pulse at a later time, and cut off the redirection effect for light emitted after this second IR pulse. This temporal control is an important aspect of this spatial control technique.

Sending the FID in a different direction than the excitation pulse has multiple spectral implications that should be considered. First, experimentally, FID and the excitation pulse end up being measured at the same location on a spectrometer, meaning that FID emission is usually studied as a change in the spectrum of the excitation pulse. The excitation pulse thus serves as a kind of background against which we measure the FID signal, which is problematic for weak signals and/or noisy backgrounds. However, our technique allows us to spatially separate the excitation and the FID, meaning that we can study the FID emission in a background-free setting. This is illustrated in Fig. 7.1 (g), where we now have a Lorentzian emission signal appearing off-axis from the excitation pulse due to the spatially shifted FID. Here we also have, on-axis, a much broader absorption line shape than in Fig. 7.1 (c). This is due to the IR delay chosen in (f) allowing a much shorter duration FID signal to travel in the same direction as the excitation pulse than that shown in (b). This shorter duration acts an effectively shorter lifetime which, as we observed in the previous chapter, leads to broader absorption features. By studying these spectral signals in experiment and theory and how they vary with delay of the IR, we can show that the off-axis emission has the temporal properties of FID. We will see this in section 2 and 3.

We refer to this spatial control technique as a background-free resonance-redirecting opto-optical modulator (BROOM), with which we can effectively sweep FID in a direction of our choosing. In the next section, we extend our discussion of BROOM to showing actual experimental results performed by Johan Mauritsson's group at Lund University, which demonstrate control of the BROOM technique in argon. This will allow us to illustrate and investigate many of the effects that we have previously mentioned.

## 7.2 Experimental demonstration of BROOM

The experimental measurements discussed in this section are performed in a transient absorption setup in argon [143, 147, 150], with the IR and XUV beams fixed in a non-coaxial geometry. These experiments use a 780 nm IR pulse and an XUV pulse consisting of the 9th harmonic of the IR. This spectrally centers the XUV pulse at 14 eV, allowing it to cover resonances with the singly excited $5s$ (14.09 eV) and $3d$ (14.15 eV) excited states of argon (recall from Chapter 4 that argon's ground state is the 3p state). The duration of the IR pulse is approximately 30 fs and the XUV pulse is approximately 20 fs. Though the lifetime of the FID from these excited states is on the order of nanoseconds, we expect the coherence time to be much shorter than this. However, we still expect this coherence time to be orders of magnitude longer than the duration of the IR pulses used. This allows the experiment to send the IR pulse into the gas long after the XUV pulse ($> 100$ fs), when the only electric field that can be manipulated is that of the induced FID. This acts as a confirmation method for verifying that the IR is controlling the FID emission, and not manipulating some other physics going on.

Fig. 7.3 shows the experimentally measured spatial–spectral profile of the XUV pulse. In (a), we show the no-IR case and we see the resulting FID results in narrow spectral lines that are slightly more divergent than the rest of the XUV pulse. The narrowness of these features, as we have discussed throughout this thesis, arises from the long lifetime of the emission, while the large divergence arises from dephasing

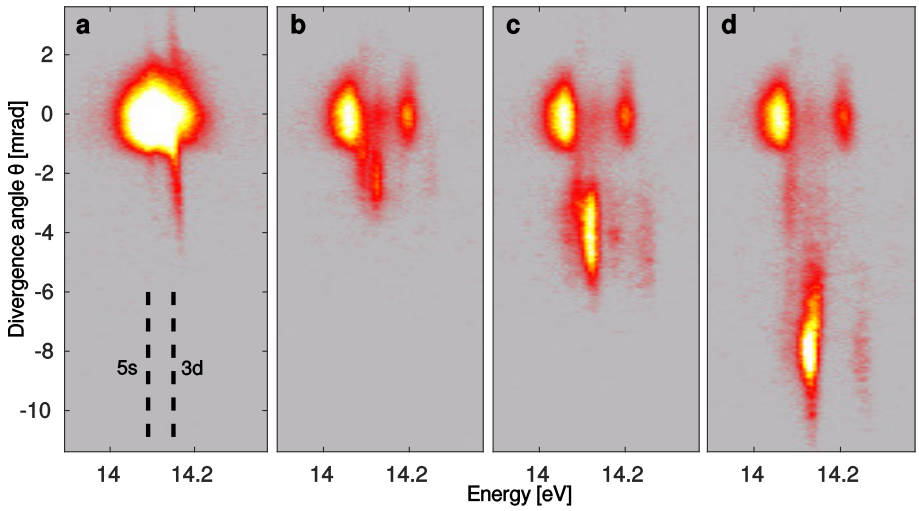


Figure 7.3: Experimental spatial–spectral profile of the XUV pulse (a) No-IR case. The emission from the 3d state is stronger since it has three times higher oscillator strength from the ground state compared to the 5s state. (b) An off-centered IR pulse follows the XUV through argon, and redirected, off-axis emission is seen from the resonant states states. (c)-(d) Increasing the IR intensity increases the induced wavefront rotation and thus also the deflection angle. The small broadening and spectral shift is due to propagation effects. The weak signal near 14.3 eV is due to higher-lying excited states. Reprinted from [43] with permission.

of the emission over this lifetime. In (b)-(d), we show the result of sending in a IR pulse 200 fs after the XUV pulse, with increasing intensity, so that the IR has a small intensity in (b) and a large intensity in (d). The IR pulse induces a spatial phase gradient across the induced electric field of the FID due the Stark-shifting of the atomic energy level. This results in the on-axis signal being terminated and the subsequent FID signal being redirect off-axis. In the beam setup used for this experiment, the phase gradient deflects the FID emission downward. As we increase the intensity of the IR, we observe that the off-axis emission is redirected further down. This is a result of the larger intensity IR pulse imposing a larger spatial phase gradient (higher intensity leads to larger phase shifts). In the prism analogy of the previous section, increasing the intensity of the IR is the same as making the prism wider, but maintaining its height. As is well known, this acts to increase the slope of the spatial phase gradient imposed by the prism, and leads to a larger angle of deflection for incident light.

The delay-dependent spectral properties of the off-axis and on-axis emission have also been investigated experimentally and are shown in Fig. 7.4. Here the beam setup has been flipped in order to send the FID emission upward. Also, the IR intensity and gas pressure have been reduced relative to Fig. 7.3 in order to minimize spectral reshaping due to propagation effects [161, 162]. In Fig. 7.4 (a), we show an example spatial–spectral profile for an 800 fs delay between the two pulses, with

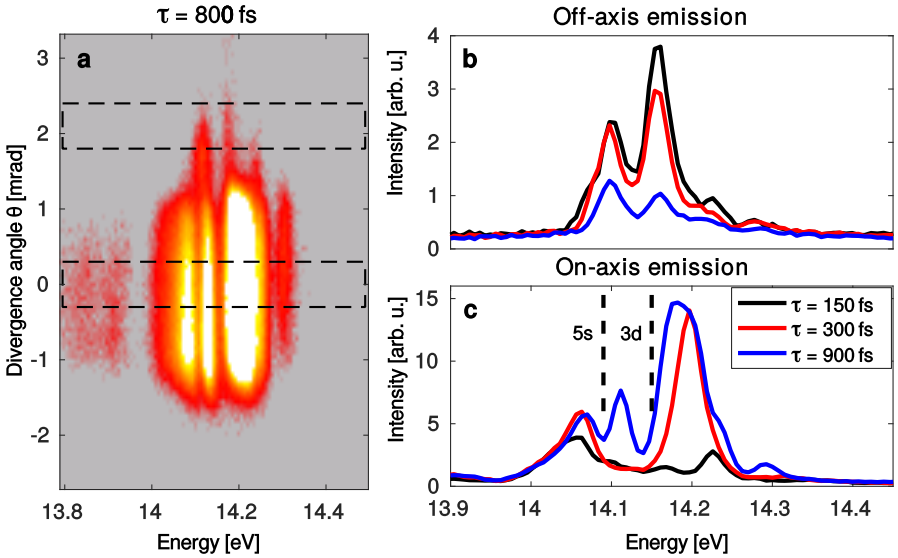


Figure 7.4: Delay dependence of the on- and off-axis emission. (a) A spatial–spectral profile at a delay of 800 fs. The dashed lines show where the off-axis (upper) and on-axis (lower) line-out is taken. (b) A line-out of the off-axis emission showing the same spectral width for all delays. (c) A line-out of the on-axis emission for different delays. The dark dashed lines show the energies corresponding to states in argon (5s and 3d). With increasing delay the absorption holes become narrower, and at a delay of 900 fs both states can be fully resolved. Reprinted from [43] with permission.

the two boxes marking the regions that we consider for the spectral lineouts in the off-axis (b) and on-axis (c) cases. In (b), we see that the off-axis emission weakens as we increase the delay. Intuitively, this is because we send less FID emission off-axis when the IR pulse comes later. The spectral width of the off-axis feature remains constant in all three cases shown, as this depends on the decay time of the emission, which is independent of the IR delay. However, the spectral width on-axis is strongly influenced by the delay. As we mentioned, this is because killing the on-axis signal imposes an effective lifetime on this feature and broadens it. While the off-axis emission at the resonant energies is observable for all delays, the on-axis emission is only observable as absorption peaks (since the FID is out of phase with the excitation pulse) at the largest delay.

Experimentally, these are brilliant demonstrations of the BROOM technique and that the off-axis emission generated by the BROOM technique results from the FID emission. These results are limited to the spectral domain, as experimentally measuring the time profile in these experiments can be fairly complicated [192]. This time profile can be achieved much easier in our theory calculations. In the next section, we discuss how we can model BROOM using the macroscopic numerical techniques that we have discussed in this thesis. We then extend these techniques to investigate the temporal profile of the off-axis emission, as a function of XUV-IR delay, and demonstrate directly that the off-axis emission arises from the FID that occurs during and after the IR pulse interacts with the medium.

### 7.3 Theoretical investigation of BROOM

Note that the numerical techniques we discussed in Chapter 5 explicitly assumed a radially symmetric geometry [164], whereas we have currently only discussed BROOM as occurring in a non-radially symmetric geometry (non-coaxial beams). However, experimentally, this non-coaxial geometry is required because the XUV beam is always spatially narrower than the IR beam and in a coaxial geometry, this leads to it being very hard to get a large phase shift on the atoms interacting with the XUV. In our calculations, we can maintain a radially symmetric geometry by modeling the XUV beam as being as spatially broad as the IR (same Gaussian beam waist size). This results in the atoms interacting with the XUV pulse experiencing the entire range of IR beam intensity (ranging from a large IR intensity in the center of the beam to a weak IR intensity at the edges), inducing a spatial phase gradient. This spatial phase gradient, however, is now radially symmetric unlike the experimental setup. This means that instead of sending the FID off in a single direction, we send it off-axis in a symmetric halo around the shared axis. For the work shown in this section, we use a helium pseudopotential, a 770 nm, 30 fs IR pulse, and a 20 fs XUV pulse resonant with the $2p$ (21.1 eV) state of helium. On the FID from this state, we input a decay lifetime of 360 fs. Further, to simplify the calculations, we solved the coupled TDSE-MWE for a single plane of atoms and then transformed the resulting electric field into the far-field and considered the

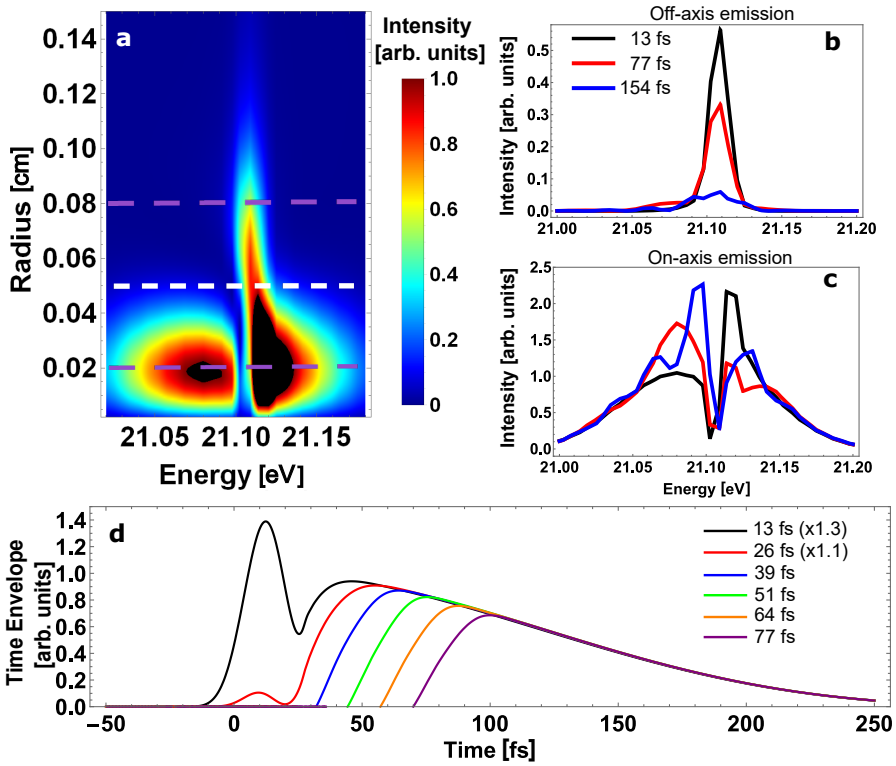


Figure 7.5: (a) Calculated, azimuthally integrated, spectral intensity for an XUV pulse centered on the $2p$ excitation energy of helium, with an XUV-IR delay of 13 fs. Note that black is saturated above the maximum. The purple dashed lines show where the off-axis (upper line) and on-axis (lower line) line-out is taken for (b) and (c), respectively. The white dashed line shows the lower boundary of what we consider to be the off-axis emission signal analyzed in (d). (b) A line-out of the off-axis emission showing the same spectral width for all delays. (c) A line-out of the on-axis emission for different delays. With increasing delay the profile approaches the no-IR case and the absorption line shape narrows. (d) The radially averaged near-field time profile of the off-axis emission for different delay. In these time profile calculations, the XUV pulse was centered at t = 0, and the IR pulse is centered at the given delay. Reprinted from [43] with permission.

azimuthally integrated result.

In Fig. 7.5 (a), we show the resulting far-field spatial–spectral profile for an IR pulse delayed by 13 fs from the XUV pulse and we indeed see a strong off-axis emission feature. We do not show it here, but we find that generally this off-axis emission has a nice quantitative agreement with the experimental results of the previous section, in that if we increase (decrease) the intensity, then the radial extent of the feature also increases (decreases). Further, this off-axis emission feature only occurs in our calculations when the IR pulse temporally overlaps the XUV pulse, or arrives after it. In Fig. 7.5 (b) and (c), we also find good quantitative agreement with the experiment between the delay-dependent behavior of the off-axis and on-axis emission features. That is, we observe the off-axis emission feature

grows weaker with increased delay, but maintains a Lorentzian shape and a constant spectral width, while the on-axis feature grows spectrally narrower at longer delays, and approaches the no IR pulse case at very long delays (not shown). This all serves to indicate that our theoretical setup has probed the same physical phenomenon (BROOM) as the experiment, despite the different geometric approach to getting the spatial phase gradient to occur. It also serves to indicate the robustness of the BROOM technique to different geometries.

This theoretical framework provides us with a way of directly testing the idea of BROOM controlling the FID. We do this by calculating the far-field spatial–spectral profile and spatially selecting the off-axis emission. In Fig. 7.5 (a), this corresponds to emission occurring at radii larger than the dashed white line. We then transform this emission back to the near-field and radially integrate the result. For normalization purposes, we subtract the time profile when no IR is present, allowing us to directly access the time profile of the off-axis emission resulting from the IR-induced spatial phase gradient. We show in Fig. 7.5 (d) as a function of delay between the XUV and IR. For a 13 fs delay (black curve), the time profile of the off-axis emission demonstrates the expected dipole response, showing a linear response to the excitation pulse until the end of the XUV (at t=25 fs), and then a long FID tail. As we increase the delay between the two pulses, the time profile of the off-axis emission shifts increasing later in this dipole response, always beginning around the temporal peak of the IR pulse, where the maximum Stark-shift will occur. This demonstrates very thoroughly that the off-axis emission from the BROOM technique results from controlling the emission direction of the FID.

## 7.4 Summary

In this chapter we have discussed BROOM, a new technique that we have developed for spatially controlling the FID of atoms in a macroscopic medium. In doing this, we have shown that an IR pulse can be used to induce a spatial phase gradient over a gas of excited atoms, and control the direction of FID emission, not unlike the ability of a wedge prism to redirect light. We have directly demonstrated this control in two different beam geometries, non-coaxial in our experimental results and coaxial in our theory results. We have also shown, in both experiment and theory, that separating the FID and the excitation pulse drastically changes the absorption line shape of the XUV pulse. This serves as nice evidence for the field picture of absorption that we have discussed in previous chapters. While this technique is still new and work is being done to better understand it, it has has many potential benefits. These benefits run the gamut from simply allowing us to study FID free of an excitation background signal, to potentially serving as a modulator in a free-electron laser, with the possibility of increasing XUV-IR pulse synchronization in these light sources to the femtosecond precision level [42, 43].

# Bibliography


[1] D. B. Milošević, S. Hu, and W. Becker. *Quantum-mechanical model for ultrahigh-order harmonic generation in the moderately relativistic regime.* Phys. Rev. A **63**, 011403 (2000).

[2] M. Herrmann, M. Haas, U. Jentschura, F. Kottmann, D. Leibfried, *et al. Feasibility of coherent xuv spectroscopy on the 1S-2S transition in singly ionized helium.* Phys. Rev. A **79**, 052505 (2009).

[3] T. Schultz and M. Vrakking. *Attosecond and XUV Spectroscopy: Ultrafast Dynamics and Spectroscopy.* John Wiley & Sons (2013).

[4] M. Desselberger, T. Afshar-Rad, F. Khattak, S. Viana, and O. Willi. *Time resolved imaging at 130 Å with submicron resolution.* Appl. Opt. **30**, 2285 (1991).

[5] F. Calegari, G. Sansone, S. Stagira, C. Vozzi, and M. Nisoli. *Advances in attosecond science.* J. Phys. B **49**, 062001 (2016).

[6] P. á. Corkum and F. Krausz. *Attosecond science.* Nat. Phys. **3**, 381 (2007).

[7] G. H. C. New and J. F. Ward. *Optical Third-Harmonic Generation in Gases.* Phys. Rev. Lett. **19**, 556 (1967).

[8] J. Wildenauer. *Generation of the ninth, eleventh, and fifteenth harmonics of iodine laser radiation.* J. Appl. Phys. **62**, 41 (1987).

[9] A. McPherson, G. Gibson, H. Jara, U. Johann, T. S. Luk, *et al. Studies of multiphoton production of vacuum-ultraviolet radiation in the rare gases.* J. Opt. Soc. Am. B **4**, 595 (1987).

[10] M. Ferray, A. L'Huillier, X. F. Li, L. A. Lompre, G. Mainfray, *et al. Multiple-harmonic conversion of 1064 nm radiation in rare gases.* J. Phys. B **21**, L31 (1988).

[11] K. J. Schafer, B. Yang, L. F. DiMauro, and K. C. Kulander. *Above threshold ionization beyond the high harmonic cutoff.* Phys. Rev. Lett. **70**, 1599 (1993).

[12] K. J. Schafer. *Numerical Methods in Strong Field Physics.* In T. Brabec (ed.), *Strong Field Laser Physics.* Springer Series in Optical Science (2008).

[13] M. B. Gaarde, J. L. Tate, and K. J. Schafer. *Macroscopic aspects of attosecond pulse generation.* J. Phys. B **41**, 132001 (2008).

[14] T. Brabec and F. Krausz. *Intense few-cycle laser fields: Frontiers of nonlinear optics.* Rev. Mod. Phys. **72**, 545 (2000).

[15] C. Heyl, C. Arnold, A. Couairon, and A. LHuillier. *Introduction to macroscopic power scaling principles for high-order harmonic generation.* J. Phys. B **50**, 013001 (2016).

[16] M. Lewenstein and A. LHuillier. *Principles of single atom physics: high-order harmonic generation, above-threshold ionization and non-sequential ionization.* In *Strong Field Laser Physics*, pp. 147–183. Springer (2008).

[17] F. Silva, S. M. Teichmann, S. L. Cousin, M. Hemmer, and J. Biegert. *Spatiotemporal isolation of attosecond soft X-ray pulses in the water window.* Nat. Comm. **6** (2015).

[18] C. Spielmann, N. Burnett, S. Sartania, R. Koppitsch, M. Schnürer, *et al. Generation of coherent X-rays in the water window using 5-femtosecond laser pulses.* Science **278**, 661 (1997).

[19] J. Tate, T. Auguste, H. Muller, P. Salieres, P. Agostini, *et al. Scaling of wave-packet dynamics in an intense midinfrared field.* Phys. Rev. Lett. **98**, 013901 (2007).

[20] A.-T. Le, H. Wei, C. Jin, and C. Lin. *Strong-field approximation and its extension for high-order harmonic generation with mid-infrared lasers.* J. Phys. B **49**, 053001 (2016).

[21] C. Hernández-García, T. Popmintchev, M. Murnane, H. Kapteyn, L. Plaja, *et al. Group velocity matching in high-order harmonic generation driven by mid-infrared lasers.* New J. Phys. **18**, 073031 (2016).

[22] T. Popmintchev, M.-C. Chen, D. Popmintchev, P. Arpin, S. Brown, *et al. Bright coherent ultrahigh harmonics in the keV x-ray regime from mid-infrared femtosecond lasers.* Science **336**, 1287 (2012).

[23] K. Midorikawa. *High-order harmonic generation and attosecond science.* Jpn. J. Appl. Phys. **50**, 090001 (2011).

[24] L. Nugent-Glandorf, M. Scheer, D. A. Samuels, A. M. Mulhisen, E. R. Grant, *et al. Ultrafast time-resolved soft x-ray photoelectron spectroscopy of dissociating Br 2.* Phys. Rev. Lett. **87**, 193002 (2001).

[25] W. Li, X. Zhou, R. Lock, S. Patchkovskii, A. Stolow, *et al. Time-resolved dynamics in N2O4 probed using high harmonic generation.* Science **322**, 1207 (2008).

[26] M. Drescher, M. Hentschel, R. Kienberger, M. Uiberacker, V. Yakovlev, *et al. Time-resolved atomic inner-shell spectroscopy.* Nature **419**, 803 (2002).

[27] D. Descamps, C. Lyngå, J. Norin, A. LHuillier, C.-G. Wahlström, *et al. Extreme ultraviolet interferometry measurements with high-order harmonics.* Opt. Lett. **25**, 135 (2000).

[28] P. Johnsson, J. Mauritsson, T. Remetter, A. L'Huillier, and K. J. Schafer. *Attosecond Control of Ionization by Wave-Packet Interference.* Phys. Rev. Lett. **99**, 233001 (2007).

[29] O. Smirnova, Y. Mairesse, S. Patchkovskii, N. Dudovich, D. Villeneuve, *et al. High harmonic interferometry of multi-electron dynamics in molecules.* Nature **460**, 972 (2009).

[30] P. Salières, L. Le Déroff, T. Auguste, P. Monot, P. d'Oliveira, *et al. Frequency-domain interferometry in the XUV with high-order harmonics.* Phys. Rev. Lett. **83**, 5483 (1999).

[31] R. Sandberg, D. Raymondson, A. Paul, K. Raines, J. Miao, *et al. Tabletop soft-x-ray Fourier transform holography with 50 nm resolution.* Opt. Lett. **34**, 1618 (2009).

[32] C. Vozzi, M. Negro, F. Calegari, G. Sansone, M. Nisoli, *et al. Generalized molecular orbital tomography.* Nat. Phys. **7**, 822 (2011).

[33] M. Zürch, J. Rothhardt, S. Hädrich, S. Demmler, M. Krebs, *et al. Real-time and sub-wavelength ultrafast coherent diffraction imaging in the extreme ultraviolet.* Sci. Rep. **4**, 7356 (2014).

[34] J. Miao, T. Ishikawa, I. K. Robinson, and M. M. Murnane. *Beyond crystallography: Diffractive imaging using coherent x-ray light sources.* Science **348**, 530 (2015).

[35] J. Schwenke, A. Mai, M. Miranda, X. He, G. Genoud, *et al. Single-shot holography using high-order harmonics.* J. Mod. Opt. **55**, 2723 (2008).

[36] L.-O. Chan, M. Siemens, M. M. Murnane, H. C. Kapteyn, S. Mathias, *et al. Ultrafast demagnetization dynamics at the M edges of magnetic elements observed using a tabletop high-harmonic soft X-ray source.* Phys. Rev. Lett. **103**, 257402 (2009).

[37] R. Carley, K. Döbrich, B. Frietsch, C. Gahl, M. Teichmann, *et al. Femtosecond laser excitation drives ferromagnetic gadolinium out of magnetic equilibrium.* Phys. Rev. Lett. **109**, 057401 (2012).

[38] J. Vura-Weis, C.-M. Jiang, C. Liu, H. Gao, J. M. Lucas, *et al. Femtosecond M2, 3-edge spectroscopy of transition-metal oxides: photoinduced oxidation state change in $\alpha$-Fe2O3.* J. Phys. Chem. Lett. **4**, 3667 (2013).

[39] C. Gohle, T. Udem, M. Herrmann, J. Rauschenberger, R. Holzwarth, *et al. A frequency comb in the extreme ultraviolet.* Nature **436**, 234 (2005).

[40] D. C. Yost, T. R. Schibli, J. Ye, J. L. Tate, J. Hostetter, *et al. Vacuum-ultraviolet frequency combs from below-threshold harmonics.* Nat. Phys. **5**, 815 (2009).

[41] P. Zeitoun, G. Faivre, S. Sebban, T. Mocek, A. Hallou, *et al. A high-intensity highly coherent soft X-ray femtosecond laser seeded by a high harmonic beam.* Nature **431**, 426 (2004).

[42] G. Lambert, T. Hara, D. Garzella, T. Tanikawa, M. Labat, *et al. Injection of harmonics generated in gas in a free-electron laser providing intense and coherent extreme-ultraviolet light.* Nat. Phys. **4**, 296 (2008).

[43] S. Bengtsson, E. Larsen, D. Kroon, S. Camp, M. Miranda, *et al. Space–time control of free induction decay in the extreme ultraviolet.* Nat. Photon. **11**, 252 (2017).

[44] P. M. Paul, E. S. Toma, P. Breger, G. Mullot, F. Augé, *et al. Observation of a train of attosecond pulses from high harmonic generation.* Science **292**, 1689 (2001).

[45] M. Hentschel, R. Kienberger, C. Spielmann, G. A. Reider, N. Milosevic, *et al. Attosecond metrology.* Nature **414**, 509 (2001).

[46] P. Agostini and L. F. DiMauro. *The physics of attosecond light pulses.* Rep. Prog. Phys. **67**, 813 (2004).

[47] F. Krausz and M. Ivanov. *Attosecond physics.* Rev. Mod. Phys. **81**, 163 (2009).

[48] M. Wu, S. Chen, S. Camp, K. J. Schafer, and M. B. Gaarde. *Theory of strong-field attosecond transient absorption.* J. Phys. B **49**, 062003 (2016).

[49] Wikipedia. *High harmonic generation — Wikipedia, The Free Encyclopedia* (2015). [Online; accessed 27-May-2015].

[50] P. B. Corkum. *Plasma perspective on strong field multiphoton ionization.* Phys. Rev. Lett. **71**, 1994 (1993).

[51] P. R. Griffiths and J. A. De Haseth. *Fourier transform infrared spectrometry.* John Wiley & Sons (2007).

[52] P. Antoine, A. L'huillier, and M. Lewenstein. *Attosecond pulse trains using high–order harmonics.* Phys. Rev. Lett. **77**, 1234 (1996).

[53] R. Lopez-Martens, K. Varjú, P. Johnsson, J. Mauritsson, Y. Mairesse, *et al. Amplitude and phase control of attosecond light pulses.* Phys. Rev. Lett. **94**, 033001 (2005).

[54] G. Sansone, E. Benedetti, F. Calegari, C. Vozzi, L. Avaldi, *et al. Isolated single-cycle attosecond pulses.* Science **314**, 443 (2006).

[55] L. Dinu, H. Muller, S. Kazamias, G. Mullot, F. Augé, *et al. Measurement of the subcycle timing of attosecond XUV bursts in high-harmonic generation.* Phys. Rev. Lett. **91**, 063901 (2003).

[56] K. T. Kim, C. Zhang, A. D. Shiner, S. E. Kirkwood, E. Frumker, *et al. Manipulation of quantum paths for space-time characterization of attosecond pulses.* Nat. Phys. **9**, 159 (2013).

[57] M. B. Gaarde and K. J. Schafer. *Theory of attosecond pulse generation.* In L. Plaja, R. Torres, and A. Zaïr (eds.), *Attosecond Physics.* Springer Berlin Heidelberg (2013).

[58] K. J. Schafer, M. B. Gaarde, A. Heinrich, J. Biegert, and U. Keller. *Strong field quantum path control using attosecond pulse trains.* Phys. Rev. Lett. **92**, 023003 (2004).

[59] P. Antoine, A. L'Huillier, M. Lewenstein, P. Salières, and B. Carré. *Theory of high-order harmonic generation by an elliptically polarized laser field.* Phys. Rev. A **53**, 1725 (1996).

[60] P. Antoine, D. B. Milošević, A. LHuillier, M. B. Gaarde, P. Salieres, *et al. Generation of attosecond pulses in macroscopic media.* Phys. Rev. A **56**, 4960 (1997).

[61] S. Kazamias and P. Balcou. *Intrinsic chirp of attosecond pulses: Single-atom model versus experiment.* Phys. Rev. A **69**, 063416 (2004).

[62] K. Zhao, Q. Zhang, M. Chini, Y. Wu, X. Wang, *et al. Tailoring a 67 attosecond pulse through advantageous phase-mismatch.* Opt. Lett. **37**, 3891 (2012).

[63] M. Lewenstein, P. Balcou, M. Y. Ivanov, A. Lhuillier, and P. B. Corkum. *Theory of high-harmonic generation by low-frequency laser fields.* Phys. Rev. A **49**, 2117 (1994).

[64] M. B. Gaarde, F. Salin, E. Constant, P. Balcou, K. Schafer, *et al. Spatiotemporal separation of high harmonic radiation into two quantum path components.* Phys. Rev. A **59**, 1367 (1999).

[65] K. Varjú, Y. Mairesse, B. Carré, M. B. Gaarde, P. Johnsson, *et al. Frequency chirp of harmonic and attosecond pulses.* J. Mod. Opt. **52**, 379 (2005).

[66] E. Larsen, S. Carlström, E. Lorek, C. Heyl, D. Paleček, *et al. Sub-cycle ionization dynamics revealed by trajectory resolved, elliptically-driven high-order harmonic generation.* Sci. Rep. **6**, 39006 (2016).

[67] S. Beaulieu, S. Camp, D. Descamps, A. Comby, V. Wanie, *et al. Role of excited states in high-order harmonic generation.* Phys. Rev. Lett. **117**, 203001 (2016).

[68] L. He, P. Lan, Q. Zhang, C. Zhai, F. Wang, *et al. Spectrally resolved spatiotemporal features of quantum paths in high-order-harmonic generation.* Phys. Rev. A **92**, 043403 (2015).

[69] C. M. Heyl, J. Güdde, U. Höfer, and A. LHuillier. *Spectrally resolved maker fringes in high-order harmonic generation.* Phys. Rev. Lett. **107**, 033903 (2011).

[70] A. Zair, M. Holler, A. Guandalini, F. Schapper, J. Biegert, *et al. Quantum path interferences in high-order harmonic generation.* Phys. Rev. Lett. **100**, 143902 (2008).

[71] S. Carlström, J. Preclíková, E. Lorek, E. W. Larsen, C. M. Heyl, *et al. Spatially and spectrally resolved quantum path interference with chirped driving pulses.* New J. Phys. **18**, 123032 (2016).

[72] C. Lyngå, M. Gaarde, C. Delfin, M. Bellini, T. Hänsch, *et al. Temporal coherence of high-order harmonics.* Phys. Rev. A **60**, 4823 (1999).

[73] L. Brugnera, D. J. Hoffmann, T. Siegel, F. Frank, A. Zaïr, *et al. Trajectory selection in high harmonic generation by controlling the phase between orthogonal two-color fields.* Phys. Rev. Lett. **107**, 153902 (2011).

[74] S. Baker, J. S. Robinson, C. A. Haworth, H. Teng, R. A. Smith, *et al. Probing proton dynamics in molecules on an attosecond time scale.* Science **312**, 424 (2006).

[75] H. Niikura, F. Legare, R. Hasbani, M. Y. Ivanov, D. M. Villeneuve, *et al. Probing molecular dynamics with attosecond resolution using correlated wave packet pairs.* Nature **421**, 826 (2003).

[76] M. Uiberacker, T. Uphues, M. Schultze, A. J. Verhoef, V. Yakovlev, *et al. Attosecond real-time observation of electron tunnelling in atoms.* Nature **446**, 627 (2007).

[77] S. Pabst, A. Sytcheva, A. Moulet, A. Wirth, E. Goulielmakis, *et al. Theory of attosecond transient-absorption spectroscopy of krypton for overlapping pump and probe pulses.* Phys. Rev. A **86**, 063411 (2012).

[78] M. Chini, B. Zhao, H. Wang, Y. Cheng, S. X. Hu, *et al. Subcycle ac Stark Shift of Helium Excited States Probed with Isolated Attosecond Pulses.* Phys. Rev. Lett. **109**, 073601 (2012).

[79] S. Chen, M. J. Bell, A. R. Beck, H. Mashiko, M. Wu, *et al. Light-induced states in attosecond transient absorption spectra of laser-dressed helium.* Phys. Rev. A **86**, 063408 (2012).

[80] M. Chini, X. Wang, Y. Cheng, Y. Wu, D. Zhao, *et al. Sub-cycle oscillations in virtual states brought to light.* Sci. Rep. **3** (2013).

[81] X. Wang, M. Chini, Y. Cheng, Y. Wu, X.-M. Tong, *et al. Subcycle laser control and quantum interferences in attosecond photoabsorption of neon.* Phys. Rev. A **87**, 063413 (2013).

[82] E. R. Hosler and S. R. Leone. *Characterization of vibrational wave packets by core-level high-harmonic transient absorption spectroscopy.* Phys. Rev. A **88**, 023420 (2013).

[83] C.-T. Liao, X. Li, D. J. Haxton, T. N. Rescigno, R. R. Lucchese, *et al. Probing autoionizing states of molecular oxygen with XUV transient absorption: Electronic-symmetry-dependent line shapes and laser-induced modifications.* Phys. Rev. A **95**, 043427 (2017).

[84] S. Camp, K. J. Schafer, and M. B. Gaarde. *Interplay between resonant enhancement and quantum path dynamics in harmonic generation in helium.* Phys. Rev. A **92**, 013404 (2015).

[85] J. Itatani, J. Levesque, D. Zeidler, H. Niikura, H. Pépin, *et al. Tomographic imaging of molecular orbitals.* Nature **432**, 867 (2004).

[86] T. Morishita, A.-T. Le, Z. Chen, and C. D. Lin. *Accurate Retrieval of Structural Information from Laser-Induced Photoelectron and High-Order Harmonic Spectra by Few-Cycle Laser Pulses.* Phys. Rev. Lett. **100**, 013903 (2008).

[87] A.-T. Le, T. Morishita, and C. D. Lin. *Extraction of the species-dependent dipole amplitude and phase from high-order harmonic spectra in rare-gas atoms.* Phys. Rev. A **78**, 023814 (2008).

[88] H. Wörner, J. Bertrand, D. Kartashov, P. Corkum, and D. Villeneuve. *Following a chemical reaction using high-harmonic spectroscopy.* Nature **466**, 604 (2010).

[89] C. Lin, A.-T. Le, Z. Chen, T. Morishita, and R. Lucchese. *Strong-field rescattering physicsself-imaging of a molecule by its own electrons.* J. Phys. B **43**, 122001 (2010).

[90] B. K. McFarland, J. P. Farrell, P. H. Bucksbaum, and M. Gühr. *High harmonic generation from multiple orbitals in N2.* Science **322**, 1232 (2008).

[91] B. D. Bruner, H. Soifer, D. Shafir, V. Serbinenko, O. Smirnova, *et al. Multidimensional high harmonic spectroscopy.* J. Phys. B **48**, 174006 (2015).

[92] K. C. Kulander and T. N. Rescigno. *Effective potentials for time-dependent calculations of multiphoton processes in atoms.* Comput. Phys. Commun. **63**, 523 (1991).

[93] D. J. Griffiths. *Introduction to quantum mechanics.* Cambridge University Press (2016).

[94] A. LHuillier, P. Balcou, S. Candel, K. J. Schafer, and K. C. Kulander. *Calculations of high-order harmonic-generation processes in xenon at 1064 nm.* Phys. Rev. A **46**, 2778 (1992).

[95] M. Bellini, C. Lyngå, A. Tozzi, M. Gaarde, T. Hänsch, *et al. Temporal coherence of ultrashort high-order harmonic pulses.* Phys. Rev. Lett. **81**, 297 (1998).

[96] R. Shankar. *Principles of quantum mechanics.* Springer Science & Business Media (2012).

[97] J. L. Krause and K. J. Schafer. *Control of THz emission from Stark wave packets.* J. Phys. Chem. A **103**, 10118 (1999).

[98] J. Henkel, T. Witting, D. Fabris, M. Lein, P. L. Knight, *et al. Prediction of attosecond light pulses in the VUV range in a high-order-harmonic-generation regime.* Phys. Rev. A **87**, 043818 (2013).

[99] F. J. Harris. *On the use of windows for harmonic analysis with the discrete Fourier transform.* Proc. IEEE **66**, 51 (1978).

[100] J. W. Cooley and J. W. Tukey. *An algorithm for the machine calculation of complex Fourier series.* Math. Comp. **19**, 297 (1965).

[101] R. B. Blackman and J. W. Tukey. *The measurement of power spectra from the point of view of communications engineering* (1958).

[102] M. Wu, D. A. Browne, K. J. Schafer, and M. B. Gaarde. *Multilevel perspective on high-order harmonic generation in solids.* Phys. Rev. A **94**, 063403 (2016).

[103] The Royal Society. *Measurements of lifetimes of excited states of helium atoms*, volume 234 (1956).

[104] S. L. Hahn. *Hilbert transforms in signal processing*, volume 2. Artech House Boston (1996).

[105] G. Doumy, J. Wheeler, C. Roedig, R. Chirla, P. Agostini, *et al. Attosecond Synchronization of High-Order Harmonics from Midinfrared Drivers.* Phys. Rev. Lett. **102**, 093002 (2009).

[106] W.-H. Xiong, L.-Y. Peng, and Q. Gong. *Recent progress of below-threshold harmonic generation.* J. Phys. B **50**, 032001 (2017).

[107] R. R. Freeman, P. H. Bucksbaum, H. Milchberg, S. Darack, D. Schumacher, *et al. Above-threshold ionization with subpicosecond laser pulses.* Phys. Rev. Lett. **59**, 1092 (1987).

[108] P. Agostini, P. Breger, A. L'Huillier, H. G. Muller, G. Petite, *et al. Giant Stark shifts in multiphoton ionization.* Phys. Rev. Lett. **63**, 2208 (1989).

[109] P. Ackermann, H. Münch, and T. Halfmann. *Resonantly-enhanced harmonic generation in Argon.* Opt. Express **20**, 13824 (2012).

[110] S. H. Autler and C. H. Townes. *Stark effect in rapidly varying fields*. Phys. Rev. **100**, 703 (1955).

[111] A. R. Beck, B. Bernhardt, E. R. Warrick, M. Wu, S. Chen, *et al. Attosecond transient absorption probing of electronic superpositions of bound states in neon: detection of quantum beats*. New J. Phys. **16**, 113016 (2014).

[112] M. Chini, X. Wang, Y. Cheng, and Z. Chang. *Resonance effects and quantum beats in attosecond transient absorption of helium*. J. Phys. B **47**, 124009 (2014).

[113] F. Mauger, A. Kamor, C. Chandre, and T. Uzer. *Mechanism of delayed double ionization in a strong laser field*. Phys. Rev. Lett. **108**, 063001 (2012).

[114] F. Mauger, A. Kamor, C. Chandre, and T. Uzer. *Delayed double ionization as a signature of Hamiltonian chaos*. Phys. Rev. E **85**, 066205 (2012).

[115] P.-C. Li, Y.-L. Sheu, C. Laughlin, and S.-I. Chu. *Role of laser-driven electron-multirescattering in resonance-enhanced below-threshold harmonic generation in He atoms*. Phys. Rev. A **90**, 041401 (2014).

[116] J. A. Hostetter, J. L. Tate, K. J. Schafer, and M. B. Gaarde. *Semiclassical approaches to below-threshold harmonics*. Phys. Rev. A **82**, 023401 (2010).

[117] A. D. DiChiara, S. Ghimire, C. I. Blaga, E. Sistrunk, E. P. Power, *et al. Scaling of high-order harmonic generation in the long wavelength limit of a strong laser field*. IEEE J. Sel. Top. Quantum Electron. **18**, 419 (2012).

[118] N. Harkema, C.-T. Liao, and A. Sandhu. *Controlling electronic couplings with tunable long wavelength pulses: Study of Autler-Townes splitting and XUV emission spectra*. Bull. Amer. Phys. Soc. (2017).

[119] G. Cirmi, C.-J. Lai, E. Granados, S.-W. Huang, A. Sell, *et al. Cut-off scaling of high-harmonic generation driven by a femtosecond visible optical parametric amplifier*. J. Phys. B **45**, 205601 (2012).

[120] B. E. Schmidt, A. D. Shiner, M. Giguère, P. Lassonde, C. A. Trallero-Herrero, *et al. High harmonic generation with long-wavelength few-cycle laser pulses*. J. Phys. B **45**, 074008 (2012).

[121] D. Milošević and W. Becker. *Role of long quantum orbits in high-order harmonic generation*. Phys. Rev. A **66**, 063417 (2002).

[122] P. Liu, P. Yu, Z. Zeng, H. Xiong, X. Ge, *et al. Laser intensity dependence of high-order harmonic generation from aligned CO 2 molecules*. Phys. Rev. A **78**, 015802 (2008).

[123] B. Borca, A. F. Starace, A. Flegel, M. Frolov, and N. Manakov. *Threshold-related effects in high-order harmonic generation*. Phys. Rev. A **65**, 051402 (2002).

[124] K. L. Ishikawa, K. Schiessl, E. Persson, and J. Burgdörfer. *Fine-scale oscillations in the wavelength and intensity dependence of high-order harmonic generation: Connection with channel closings.* Phys. Rev. A **79**, 033411 (2009).

[125] R. D. Evans and A. Noyau. *The atomic nucleus.* McGraw-Hill New York (1955).

[126] B. Di Bartolo. *Spectroscopy of the excited state*, volume 12. Springer Science & Business Media (2012).

[127] K. Schafer and K. Kulander. *Theory of resonant multiphoton population transfer in xenon.* Laser Phys. **7**, 740 (1997).

[128] M. B. Gaarde and K. J. Schafer. *Calculations of resonant multiphoton population transfer in potassium atoms at long wavelengths.* Phys. Rev. A **62**, 053411 (2000).

[129] M. Lewenstein, P. Salieres, and A. Lhuillier. *Phase of the atomic polarization in high-order harmonic generation.* Phys. Rev. A **52**, 4747 (1995).

[130] P. Salières, A. L'Huillier, P. Antoine, and M. Lewenstein. *Study of the Spatial and Temporal Coherence of High-Order Harmonics.* Advances in Atomic Molecular and Optical Physics **41** (1999).

[131] M. B. Gaarde and K. J. Schafer. *Quantum path distributions for high-order harmonics in rare gas atoms.* Phys. Rev. A **65**, 031406 (2002).

[132] P. Salières and I. Christov. *Macroscopic effects in high-order harmonic generation.* In T. Brabec (ed.), *Strong Field Laser Physics*, pp. 261–280. Springer (2008).

[133] H. Merdji, M. Kovačev, W. Boutu, P. Salieres, F. Vernay, *et al. Macroscopic control of high-order harmonics quantum-path components for the generation of attosecond pulses.* Phys. Rev. A **74**, 043804 (2006).

[134] H. Vincenti and F. Quéré. *Attosecond lighthouses: how to use spatiotemporally coupled light fields to generate isolated attosecond pulses.* Phys. Rev. Lett. **108**, 113904 (2012).

[135] N. Dudovich, O. Smirnova, J. Levesque, Y. Mairesse, M. Y. Ivanov, *et al. Measuring and controlling the birth of attosecond XUV pulses.* Nat. Phys. **2**, 781 (2006).

[136] T. Chuang and K. Eisenthal. *Studies of effects of hydrogen bonding on orientational relaxation using picosecond light pulses.* Chem. Phys. Lett. **11**, 368 (1971).

[137] G. R. Fleming, J. M. Morris, and G. W. Robinson. *Direct observation of rotational diffusion by picosecond spectroscopy.* Chem. Phys. **17**, 91 (1976).

[138] G. Porter, P. Sadkowski, and C. Tredwell. *Picosecond rotational diffusion in kinetic and steady state fluorescence spectroscopy.* Chem. Phys. Lett. **49**, 416 (1977).

[139] F. Laermer, T. Elsaesser, and W. Kaiser. *Ultrashort vibronic and thermal relaxation of dye molecules after femtosecond ultraviolet excitation.* Chem. Phys. Lett. **156**, 381 (1989).

[140] M. Dantus, R. Bowman, and A. Zewail. *Femtosecond laser observations of molecular vibration and rotation.* Nature **343**, 737 (1990).

[141] A. Taylor, D. Erskine, and C. Tang. *Femtosecond vibrational relaxation of large organic molecules.* Chem. Phys. Lett. **103**, 430 (1984).

[142] M. Rosker, F. Wise, and C. Tang. *Femtosecond relaxation dynamics of large molecules.* Phys. Rev. Lett. **57**, 321 (1986).

[143] E. Goulielmakis, Z.-H. Loh, A. A. Wirth, R. Santra, N. Rohringer, *et al. Real-time observation of valence electron motion.* Nature **466**, 739 (2010).

[144] T. E. Glover, M. P. Hertlein, S. H. Southworth, T. K. Allison, J. van Tilborg, *et al. Controlling X-rays with light.* Nat. Phys. **6**, 69 (2010).

[145] F. Kelkensberg, C. Lefebvre, W. Siu, O. Ghafur, T. Nguyen-Dang, *et al. Molecular dissociative ionization and wave-packet dynamics studied using two-color XUV and IR pump-probe spectroscopy.* Phys. Rev. Lett. **103**, 123005 (2009).

[146] J. Mauritsson, T. Remetter, M. Swoboda, K. Klünder, A. L'Huillier, *et al. Attosecond Electron Spectroscopy Using a Novel Interferometric Pump-Probe Technique.* Phys. Rev. Lett. **105**, 053001 (2010).

[147] H. Wang, M. Chini, S. Chen, C.-H. Zhang, F. He, *et al. Attosecond Time-Resolved Autoionization of Argon.* Phys. Rev. Lett. **105**, 143002 (2010).

[148] M. Holler, F. Schapper, L. Gallmann, and U. Keller. *Attosecond Electron Wave-Packet Interference Observed by Transient Absorption.* Phys. Rev. Lett. **106**, 123601 (2011).

[149] S. Chen, M. Wu, M. B. Gaarde, and K. J. Schafer. *Laser-imposed phase in resonant absorption of an isolated attosecond pulse.* Phys. Rev. A **88**, 033409 (2013).

[150] C. Ott, A. Kaldun, P. Raith, K. Meyer, M. Laux, *et al. Lorentz Meets Fano in Spectral Line Shapes: A Universal Phase and Its Laser Control.* Science **340**, 716 (2013).

[151] J. Herrmann, M. Weger, R. Locher, M. Sabbar, P. Rivière, *et al. Virtual single-photon transition interrupted: Time-gated optical gain and loss.* Phys. Rev. A **88**, 043843 (2013).

[152] J. E. Bækhøj, L. Yue, and L. B. Madsen. *Nuclear-motion effects in attosecond transient-absorption spectroscopy of molecules.* Phys. Rev. A **91**, 043408 (2015).

[153] M. Schultze, E. M. Bothschafter, A. Sommer, S. Holzner, W. Schweinberger, *et al. Controlling dielectrics with the electric field of light.* Nature **493**, 75 (2013).

[154] C.-M. Jiang, L. R. Baker, J. M. Lucas, J. Vura-Weis, A. P. Alivisatos, *et al. Characterization of Photo-Induced Charge Transfer and Hot Carrier Relaxation Pathways in Spinel Cobalt Oxide (Co3O4).* J. Phys. Chem. C **118**, 22774 (2014).

[155] S. Chen, M. J. Bell, A. R. Beck, H. Mashiko, M. Wu, *et al. Light-induced states in attosecond transient absorption spectra of laser-dressed helium.* Phys. Rev. A **86**, 063408 (2012).

[156] M. Wu, S. Chen, M. B. Gaarde, and K. J. Schafer. *Time-domain perspective on Autler-Townes splitting in attosecond transient absorption of laser-dressed helium atoms.* Phys. Rev. A **88**, 043416 (2013).

[157] S. Chen, M. Wu, M. B. Gaarde, and K. J. Schafer. *Quantum interference in attosecond transient absorption of laser-dressed helium atoms.* Phys. Rev. A **87**, 033408 (2013).

[158] M. B. Gaarde, C. Buth, J. L. Tate, and K. J. Schafer. *Transient absorption and reshaping of ultrafast XUV light by laser-dressed helium.* Phys. Rev. A **83**, 013419 (2011).

[159] Wikipedia. *Gaussian beam — Wikipedia, The Free Encyclopedia* (2017). [Online; accessed 21-May-2017].

[160] A. E. Siegman. *Lasers.* University Science Books (1986).

[161] C.-T. Liao, A. Sandhu, S. Camp, K. J. Schafer, and M. B. Gaarde. *Beyond the Single-Atom Response in Absorption Line Shapes: Probing a Dense, Laser-Dressed Helium Gas with Attosecond Pulse Trains.* Phys. Rev. Lett. **114**, 143002 (2015).

[162] C.-T. Liao, A. Sandhu, S. Camp, K. J. Schafer, and M. B. Gaarde. *Attosecond transient absorption in dense gases: Exploring the interplay between resonant pulse propagation and laser-induced line-shape control.* Phys. Rev. A **93**, 033405 (2016).

[163] A. N. Pfeiffer, M. J. Bell, A. R. Beck, H. Mashiko, D. M. Neumark, *et al. Alternating absorption features during attosecond-pulse propagation in a laser-controlled gaseous medium.* Phys. Rev. A **88**, 051402 (2013).

[164] M. B. Gaarde, C. Buth, J. L. Tate, and K. J. Schafer. *Transient absorption and reshaping of ultrafast XUV light by laser-dressed helium.* Phys. Rev. A **83**, 013419 (2011).

[165] W.-C. Chu and C. D. Lin. *Resonant enhancement of a single attosecond pulse in a gas medium by a time-delayed control field.* J. Phys. B **45**, 201002 (2012).

[166] M. Wu, S. Chen, K. J. Schafer, and M. B. Gaarde. *Ultrafast time-dependent absorption in a macroscopic three-level helium gas.* Phys. Rev. A **87**, 013828 (2013).

[167] E. Perfetto and G. Stefanucci. *Some exact properties of the nonequilibrium response function for transient photoabsorption.* Phys. Rev. A **91**, 033416 (2015).

[168] E. Perfetto, A.-M. Uimonen, R. van Leeuwen, and G. Stefanucci. *First-principles nonequilibrium Green's-function approach to transient photoabsorption: Application to atoms.* Phys. Rev. A **92**, 033419 (2015).

[169] M. Crisp. *Propagation of small-area pulses of coherent light through a resonant medium.* Phys. Rev. A **1**, 1604 (1970).

[170] G. Lamb. *Analytical descriptions of ultrashort optical pulse propagation in a resonant medium.* Rev. Mod. Phys. **43**, 99 (1971).

[171] S. Chen, M. Wu, M. B. Gaarde, and K. J. Schafer. *Quantum interference in attosecond transient absorption of laser-dressed helium atoms.* Phys. Rev. A **87**, 033408 (2013).

[172] L. Gallmann, J. Herrmann, R. Locher, M. Sabbar, A. Ludwig, *et al. Resolving intra-atomic electron dynamics with attosecond transient absorption spectroscopy.* Mol. Phys. **111**, 2243 (2013).

[173] A. R. Beck, D. M. Neumark, and S. R. Leone. *Probing ultrafast dynamics with attosecond transient absorption.* Chem. Phys. Lett. **624**, 119 (2015).

[174] U. Van Bürck. *Coherent pulse propagation through resonant media.* Hyperfine Interact. **123**, 483 (1999).

[175] M. A. Bouchene. *Phase control of dispersion effects for an ultrashort pulse train propagating in a resonant medium.* Phys. Rev. A **66**, 065801 (2002).

[176] J. C. Delagnes and M. A. Bouchene. *Gain-dispersion coupling induced by transient light shifts in an atomic medium.* Phys. Rev. A **76**, 023422 (2007).

[177] L. Costanzo, A. Coelho, D. Pellegrino, M. Mendes, L. Acioli, *et al. Zero-Area Single-Photon Pulses.* Phys. Rev. Lett. **116**, 023602 (2016).

[178] Z. Yang, D. Ye, T. Ding, T. Pfeifer, and L. Fu. *Attosecond XUV absorption spectroscopy of doubly excited states in helium atoms dressed by a time-delayed femtosecond infrared laser*. Phys. Rev. A **91**, 013414 (2015).

[179] P. Debye and F. Sears. *On the scattering of light by supersonic waves*. Proc. Natl. Acad. Sci. **18**, 409 (1932).

[180] T. A. Maldonado. *Electro-optic modulators*. Handbook of optics **2**, 13 (1995).

[181] A. M. Weiner. *Femtosecond pulse shaping using spatial light modulators*. Rev. Sci. Instrum. **71**, 1929 (2000).

[182] W. a. Ackermann, G. Asova, V. Ayvazyan, A. Azima, N. Baboi, *et al. Operation of a free-electron laser from the extreme ultraviolet to the water window*. Nat. Photon. **1**, 336 (2007).

[183] P. Emma, R. Akre, J. Arthur, R. Bionta, C. Bostedt, *et al. First lasing and operation of an ångstrom-wavelength free-electron laser*. Nat. Photon. **4**, 641 (2010).

[184] C. Schroer and B. Lengeler. *X-ray optics*. In *Springer Handbook of Lasers and Optics*, pp. 1153–1164. Springer (2007).

[185] F. Bloch. *Nuclear induction*. Phys. Rev. **70**, 460 (1946).

[186] E. Hahn. *Nuclear induction due to free Larmor precession*. Phys. Rev. **77**, 297 (1950).

[187] R. G. Brewer and R. Shoemaker. *Optical free induction decay*. Phys. Rev. A **6**, 2001 (1972).

[188] F. A. Hopf, R. F. Shea, and M. O. Scully. *Theory of optical free-induction decay and two-photon superradiance*. Phys. Rev. A **7**, 2105 (1973).

[189] C. Ott, A. Kaldun, L. Argenti, P. Raith, K. Meyer, *et al. Reconstruction and control of a time-dependent two-electron wave packet*. Nature **516**, 374 (2014).

[190] B. Bernhardt, A. R. Beck, X. Li, E. R. Warrick, M. J. Bell, *et al. High-spectral-resolution attosecond absorption spectroscopy of autoionization in xenon*. Phys. Rev. A **89**, 023408 (2014).

[191] D. J. Brady. *Optical imaging and spectroscopy*. John Wiley & Sons (2009).

[192] Y. Mairesse and F. Quéré. *Frequency-resolved optical gating for complete reconstruction of attosecond bursts*. Phys. Rev. A **71**, 011401 (2005).

# Vita

Seth Camp was born in Rome, Georgia. He grew up in Cedartown, Georgia living with his father. He attended Berry College and received a Bachelor of Science degree in Mathematics and Physics in May 2011. That fall, he was began a doctoral program in physics at Louisiana State University under the supervision of Mette Gaarde and Kenneth Schafer. He will receive the degree of Doctor of Philosophy in Physics at the August 2017 commencement.